

## Gravitational wave sources in our Galactic backyard: Predictions for BHBH, BHNS and NSNS binaries detectable with LISA

2 T. WAGG ,<sup>1,2,3</sup> F.S. BROEKGAARDEN ,<sup>2</sup> S.E. DE MINK ,<sup>3,4,2</sup> N. FRANKEL ,<sup>5,6,7</sup> L.A.C. VAN SON ,<sup>2,4,3</sup> AND  
3 S. JUSTHAM 

4 <sup>1</sup>*Department of Astronomy, University of Washington, Seattle, WA, 98195*

5 <sup>2</sup>*Center for Astrophysics — Harvard & Smithsonian, 60 Garden Street, Cambridge, MA 02138, USA*

6 <sup>3</sup>*Max-Planck-Institut für Astrophysik, Karl-Schwarzschild-Straße 1, 85741 Garching, Germany*

7 <sup>4</sup>*Anton Pannekoek Institute for Astronomy & Grappa, University of Amsterdam, Postbus 94249, 1090 GE Amsterdam, The Netherlands*

8 <sup>5</sup>*Canadian Institute for Theoretical Astrophysics, University of Toronto, 60 St. George Street, Toronto, ON M5S 3H8, Canada*

9 <sup>6</sup>*Max Planck Institute for Astronomy, Königstuhl 17, D-69117 Heidelberg, Germany*

10 <sup>7</sup>*David A. Dunlap Department for Astronomy and Astrophysics, University of Toronto, 50 St. George Street, Toronto, ON M5S 3H4, Canada*

11 <sup>8</sup>*School of Astronomy & Space Science, University of the Chinese Academy of Sciences, Beijing 100012, China*

13 (Received July 6, 2022)

### ABSTRACT

15 Future searches for gravitational waves from space will be sensitive to double compact objects (DCOs)  
16 in our Milky Way. We present new simulations of the populations of double black holes (BHBs), black  
17 hole neutron stars (BHNSs) and double neutron stars (NSNSs) that will be detectable by the planned  
18 space-based gravitational wave detector LISA. For our estimates, we use an empirically-informed model  
19 of the metallicity dependent star formation history of the Milky Way. We populate it using an extensive  
20 suite of binary population-synthesis predictions for varying assumptions relating to mass transfer,  
21 common-envelope, supernova kicks, remnant masses and wind mass loss physics. **Each model in the**  
22 **grid has been recently shown to be consistent with current constraints on the inferred**  
23 **overall GW rates from ground-based detectors.**

24 For a 4(10)-year LISA mission, we predict between 30-370(50-550) detections over these variations,  
25 out of which 6-154(9-238) are BHBs, 2-198(3-289) are BHNSs and 3-35(4-57) are NSNSs. **We expect**  
26 **that about 50%(60%) can be distinguished from WDWD sources, based on their mass**  
27 **or eccentricity and localisation. Specifically, for about 10%(15%) we expect to be able**  
28 **to determine chirp masses better than 10%. For 13%(13%) we expect sky-localisations**  
29 **better than 1 degree.** We discuss how the variations in the physics assumptions alter the distribution  
30 of properties of the detectable systems, even when the detection rates are unchanged. We further  
31 discuss the possibility of multi-messenger observations of pulsar populations with the Square Kilometre  
32 Array (SKA) and assess the benefits of extending the LISA mission.

33 **Keywords:** gravitational waves, gravitational wave detectors, compact objects, stellar mass black holes,  
34 neutron stars, binary stars, stellar evolution, pulsars

### 1. INTRODUCTION

35 Since the first direct observation of gravitational waves  
36 ([Abbott et al. 2016](#)), the number of black hole (BH) and  
37 neutron star (NS) binaries observed by ground-based

39 gravitational-wave detectors has rapidly grown ([Abbott](#)  
40 [et al. 2019, 2020b; The LIGO Scientific Collaboration](#)  
41 [et al. 2021c](#)), offering exciting insights into the forma-  
42 tion, lives and deaths of massive (binary) stars (e.g. [Ab-](#)  
43 [bott et al. 2021](#)).

44 The Laser Interferometer Space Antenna (LISA,  
45 [Amaro-Seoane et al. 2017; Colpi et al. 2019](#)) will pro-  
46 vide observations in an entirely new regime of grav-  
47 itational waves. LISA will observe at lower frequen-

48 cies ( $10^{-5} \lesssim f/\text{Hz} \lesssim 10^{-1}$ ) than ground-based detec-  
 49 tors and so will enable the study of sources that are  
 50 imperceptible by ground-based detectors, such as the  
 51 mergers of supermassive black holes and extreme mass-  
 52 ratio inspirals (e.g. Begelman et al. 1980; Klein et al.  
 53 2016). Moreover, this frequency regime is also of inter-  
 54 est for the detection of *local* stellar-mass double compact  
 55 objects (DCOs) millions of years before their merger.  
 56 This presents an opportunity for both multi-messenger  
 57 detections to search for electromagnetic counterparts,  
 58 as well as multiband gravitational-wave detections that  
 59 can help to constrain binary characteristics (e.g. Sesana  
 60 2016; Gerosa et al. 2019). In addition, LISA will be  
 61 able to measure the eccentricities of DCOs, which may  
 62 yield further constraints on binary evolution, differentiat-  
 63 ate between formation channels and distinguish between  
 64 DCO types (e.g. Nelemans et al. 2001; Breivik et al.  
 65 2016; Antonini et al. 2017; Rodriguez et al. 2018). Un-  
 66 like ground-based detectors, **the majority of stellar-**  
**67 mass sources detected in LISA will reside in local**  
**68 galaxies, with most situated in the Milky Way.**  
 69 These sources could be used as a probe for the structure  
 70 of our galaxy (e.g. Korol et al. 2019).

71 Traditionally, predictions about the detection of  
 72 stellar-mass sources with LISA focus on double white  
 73 dwarf (WDWD) binaries, as they are abundantly  
 74 present in our galaxy and are expected to be the domi-  
 75 nant source of stellar-mass binaries that are detectable  
 76 by LISA (Nelemans et al. 2001; Ruiter et al. 2010; Yu  
 77 & Jeffery 2010; Nissanke et al. 2012; Korol et al. 2017;  
 78 Lamberts et al. 2018). More recently, interest has grown  
 79 in the detection of NS and BH binaries. Although they  
 80 are more rare, LISA detections of these sources are po-  
 81 tentially valuable for learning more about the evolution  
 82 and endpoints of massive stars. In this paper we focus  
 83 on making LISA predictions for double black hole bina-  
 84 ries (BHBHs), black hole neutron star binaries (BHNSs)  
 85 and double neutron star binaries (NSNSs).

86 The detection of NSNSs in LISA could improve our  
 87 understanding of many phenomena. Galactic NSNSs  
 88 have been observed with electromagnetic signals for sev-  
 89 eral decades (e.g. Hulse & Taylor 1975; Antoniadis et al.  
 90 2016, see also refs. in Tauris et al. 2017) and more re-  
 91 cently the mergers of NSNSs have been detected with  
 92 ground-based gravitational-wave detectors (e.g. Abbott  
 93 et al. 2017a). A LISA detectable NSNS with a pulsar  
 94 component close to merger would be ideal for connecting  
 95 these populations, as the binary could be observed from  
 96 inspiral to merger. NSNSs (and possibly BHNSs) are  
 97 useful sources for understanding the origin of r-process  
 98 elements (e.g. Eichler et al. 1989) as well as the elec-  
 99 tromagnetic counterparts to gravitational-wave signals,

100 such as kilonovae (e.g. Li & Paczyński 1998; Metzger  
 101 2017), short gamma-ray bursts (e.g. Berger 2014), ra-  
 102 dio emission (e.g. Hotokezaka et al. 2016) and neutrinos  
 103 (e.g. Kyutoku et al. 2018).

104 BHBHs in the Milky Way present a greater observa-  
 105 tional challenge. To date, no BH has been observed in a  
 106 BHBH binary in the Milky Way, and so LISA could pro-  
 107 vide the first detection of a Galactic BHBH. The only  
 108 confirmed BHs in our galaxy have been discovered as  
 109 components of X-ray binaries with companion stars (e.g.  
 110 Bolton 1972; Webster & Murdin 1972). These detec-  
 111 tions have observed BHs with masses mainly constrained  
 112 between 5 and  $10 M_{\odot}$  (Corral-Santana et al. 2016), a  
 113 stark contrast to the more massive BHs observed with  
 114 LIGO/Virgo that tend to contain at least one BH with a  
 115 mass greater than  $10 M_{\odot}$  (Abbott et al. 2020b). These  
 116 observations of X-ray binaries suggest the presence of  
 117 a lower mass gap (from  $2-5 M_{\odot}$ ) in which there are no  
 118 strong candidates for either black holes or neutron stars  
 119 (Özel et al. 2010; Farr et al. 2011) but the gap's exis-  
 120 tence remains an open question (e.g. Kreidberg et al.  
 121 2012; Mandel & Müller 2020; Jayasinghe et al.  
 122 2021). Recently there has also been increased discuss-  
 123 ion over the maximum BH mass in our galaxy, with the  
 124 claims of a  $70 M_{\odot}$  BH (Liu et al. 2019) which has sub-  
 125 sequently been challenged (El-Badry & Quataert 2020;  
 126 Abdul-Masih et al. 2020; Shenar et al. 2020; Eldridge  
 127 et al. 2020, see also Liu et al. 2020) and revised mea-  
 128 surements of the mass of Cygnus X-1 (Miller-Jones et al.  
 129 2021). A sample of BHBHs detected with LISA could  
 130 possibly help to constrain the BH mass distribution.

131 One particularly interesting class of potential LISA  
 132 sources is BHNSs. With the recent detection of two  
 133 BHNSs by the LIGO scientific collaboration, the exis-  
 134 tence of these DCOs has been confirmed (The LIGO Sci-  
 135 entific Collaboration et al. 2021b). However, with only  
 136 two detections (not including the low-confidence candi-  
 137 date GW190426, Abbott et al. 2020b, or GW190425,  
 138 GW190814 and GW190917 which have not been ruled  
 139 out as BHNSs, Abbott et al. 2020a,c; The LIGO Sci-  
 140 entific Collaboration et al. 2021a) and no electromag-  
 141 netic counterparts, the formation rate and properties of  
 142 BHNSs are still uncertain. A distinctly exciting possibil-  
 143 ity for BHNSs is the detection of a pulsar–BH system or  
 144 millisecond pulsar–BH system (Narayan et al. 1991; Pol  
 145 et al. 2021). These systems could be observed not only  
 146 by LISA, but also radio telescopes such as MeerKAT  
 147 and the Square Kilometre Array (SKA, Dewdney et al.  
 148 2009), which would help to improve the measurement of  
 149 individual system parameters and to constrain uncertain  
 150 binary evolution processes (e.g. Pfahl et al. 2005; Chat-  
 151 topadhyay et al. 2020). **Moreover, the pulsar acts**

as an ultraprecise clock around a BH and thus a pulsar–BH system provides stringent tests of theories of gravity (Keane et al. 2015).

For the purposes of this investigation, we consider the ‘classical’ isolated binary evolution channel (e.g. Tutukov & Yungelson 1973, 1993; Smarr & Blandford 1976; Srinivasan 1989; Kalogera et al. 2007; Belczynski et al. 2016) in which double compact objects are formed following common-envelope ejection or a phase of highly non-conservative mass transfer (van den Heuvel 2011; van den Heuvel et al. 2017). We do not, however, account for several alternative proposed formation channels, which could affect the rate and distribution of detectable NS and BH binaries in LISA. These channels include: dynamical formation in dense star clusters (e.g. Sigurdsson & Hernquist 1993; Portegies Zwart & McMillan 2000; Miller & Lauburg 2009; Rodriguez et al. 2015), young/open star clusters (e.g. Ziosi et al. 2014; Di Carlo et al. 2020; Banerjee 2020; Rastello et al. 2020, 2021) and (active) galactic nuclei discs (e.g. Morris 1993; Antonini & Rasio 2016; McKernan et al. 2020), isolated (hierarchical) triple evolution involving Kozai-Lidov oscillations (e.g. Stephan et al. 2016; Silsbee & Tremaine 2017; Antonini et al. 2017; Toonen et al. 2020), and chemically homogenous evolution through efficient rotational mixing (e.g. de Mink et al. 2009; Mandel & de Mink 2016; Marchant et al. 2016, 2017; du Buisson et al. 2020).

In this paper, we present models for the detection rate and distribution of binary properties (masses, frequency, eccentricity, distance, merger time) of BHBHs, BHNSs and NSNSs formed through isolated binary evolution in the Milky Way. We explore the effect of varying physical assumptions in our population synthesis model on our results as well as discuss the effect of extending the LISA mission length and the prospects for distinguishing DCO detections from the WDWD background.

Earlier work on BHBHs, BHNSs and NSNSs in LISA has used a variety of population synthesis codes, Milky Way models and LISA specifications, resulting in a wide range of predictions (Nelemans et al. 2001; Belczynski et al. 2010; Liu & Zhang 2014; Lamberts et al. 2019; Lau et al. 2020; Breivik et al. 2020; Sesana et al. 2020; Shao & Li 2021). We build upon previous efforts but with several important improvements. We explore the effects of varying binary physics assumptions by repeating our analysis for 20 different models, which have each been shown to be consistent with constraints on the inferred overall GW rates from ground-based detectors, and comparing the effects on the detection rate and distributions of source parameters (Broekgaarden et al. 2021a,b). We use a model for the Milky Way that accounts for the chemical enrichment history

and is calibrated on the APOGEE survey (Majewski et al. 2017; Frankel et al. 2018), whereas most others did not consider the effect of metallicity in detail (see however Lamberts et al. 2019; Sesana et al. 2020). We provide a detailed treatment of the eccentricity of detectable sources, both for the inspiral evolution as well as gravitational wave signal during the LISA mission. Moreover, the grid of binary population synthesis simulations that we use is the most extensive of its kind to date and makes use of the adaptive sampling algorithm STROOPWAFEL (Broekgaarden et al. 2019, 2021a). Overall over 2 billion massive binaries were simulated to produce the DCO populations used in this work. We find that this large number of simulations is important to reduce the sampling noise even when using adaptive importance sampling.

All data related to the predictions made in this study are publicly available on Zenodo at Wagg et al. (2021), as are the populations used in our simulations at Broekgaarden (2021a, BHBH) Broekgaarden (2021b, BHNS) and Broekgaarden (2021c, NSNS). We make all code used to produce our results available in a Github repository [Q<sup>1</sup>](#). In addition, the repository contains step-by-step Jupyter notebooks that explain how to reproduce and change each figure in the paper. In a companion paper, Wagg et al. (2021), we present [LEGWORK<sup>2</sup>](#), the LISA Evolution and Gravitational Wave Orbit Kit, a python package designed for making predictions for the detection of sources with LISA, which we use in this work.

Our paper is structured as follows. In Section 2, we describe the methods for synthesising a population of binaries, the variations of physical assumptions that we consider, how we simulate the Milky Way distribution of DCOs and our methods for calculating a detection rate for LISA. We present the main results for our fiducial model in Section 3, before exploring the variations in the detectable population when changing our physical assumptions in Section 4. In Section 5 we discuss these how and whether these sources can be distinguished from the WDWD population and whether the subpopulations of NSNS, BHNS and BHBH can be distinguished from one other. We further discuss prospects for identifying EM counterparts, the role of different formation channels and overall caveats in the modelling approach. In Section 6, we compare and contrast our methods and findings to previous work and finish with our conclusions in Section 7.

<sup>1</sup><https://github.com/TomWagg/detecting-DCOs-in-LISA>

<sup>2</sup><https://legwork.readthedocs.io>

## 2. METHOD

To produce predictions for the DCOs that are detectable with LISA, we use a synthesised population of DCOs, simulated using the methods described in Section 2.1. In Section 2.2 we describe our model for the Milky Way and how we place DCOs in randomly sampled Milky Way instances. We evolve the orbit of each DCO in a Milky Way instance up to the LISA mission and calculate the detection rate for that instance using the methods presented in Section 2.3.

### 2.1. Binary population synthesis

We use the grid of 20 binary population synthesis simulations recently presented in Broekgaarden et al. (2021a,b). This grid of simulations is synthesised using the rapid population synthesis code COMPAS (Stevenson et al. 2017; Vigna-Gómez et al. 2018; Stevenson et al. 2019; Broekgaarden et al. 2019). COMPAS follows the approach of the population synthesis code BSE (Hurley et al. 2000, 2002) and uses fitting formula and rapid algorithms to efficiently predict the final fate of binary systems. The code is open source and documented in the papers listed above, the online documentation<sup>3</sup> and in the methods paper (Team COMPAS: J. Riley et al. 2021). The model we refer to as our fiducial model allows for BHs with masses in the heavily debated mass gap, but we also consider 20 physics variations. Broekgaarden et al. (2021b) showed that all of these physics variations are still consistent with current constraints on the overall inferred GW rates, at least when considering large variations of the assumed metallicity specific cosmic star formation rate (The LIGO Scientific Collaboration et al. 2021c). We summarise the main assumptions and settings relevant for this work in Appendix A.

The result of the simulations is a sample of binaries, which, for each metallicity  $Z$ , have  $N_{\text{binaries}}$  binaries with parameters

$$\mathbf{b}_{Z,i} = \{m_1, m_2, a_{\text{DCO}}, e_{\text{DCO}}, t_{\text{evolve}}, t_{\text{inspiral}}, w\}, \quad (1)$$

for  $i = 1, 2, \dots, N_{\text{binaries}}$ , where  $m_1$  and  $m_2$  are the primary and secondary masses,  $a_{\text{DCO}}$  and  $e_{\text{DCO}}$  are the semi-major axis and eccentricity at the moment of double compact object (DCO) formation,  $t_{\text{evolve}}$  is the time between the binary's zero-age main sequence and DCO formation,  $t_{\text{inspiral}}$  is the time between DCO formation (that is, immediately after the second supernova in the system) and gravitational-wave merger and  $w$  is

<sup>3</sup><https://compas.science>

the adaptive importance sampling weight assigned by STROOPWAFEL (Broekgaarden et al. 2019, Eq. 7). We sample from these sets of parameters when creating synthetic galaxies.

### 2.2. Galaxy synthesis

In order to estimate a detection rate of DCOs with statistical uncertainties, we create a series of random instances of the Milky Way, each populated with a sub-sample drawn (with replacement) from the synthesised binaries described in Section 2.1.

Most previous studies that predict a detection rate for LISA place binaries in the Milky Way independently of their age or evolution. We improve upon this as the first study to use an empirically-informed analytical model of the Milky Way that takes into account the galaxy's enrichment history by applying the metallicity-radius-time relation from Frankel et al. (2018). Those authors developed this relation in order to measure the global efficiency of radial migration in the Milky Way and calibrated it using a sample of red clump stars measured with APOGEE (Majewski et al. 2017). We assess the impact of using this improved Milky Way model in Appendix D and the effect of Galactic models on LISA predictions has been investigated more generally in Storck & Church (2022).

In Section 2.2.1, we outline our model for the Milky Way and in Section 2.2.2 we explain how we combine our population of synthesised DCOs with this Milky Way model.

#### 2.2.1. Milky Way model

Fig. 1 shows the distributions and relations outlined in this section and also displays an example random galaxy drawn using this model.

Our model for the Milky Way accounts for the low-[ $\alpha/\text{Fe}$ ]<sup>4</sup> disc, high-[ $\alpha/\text{Fe}$ ] disc and a central component approximating a bulge/bar. The low- and high-[ $\alpha/\text{Fe}$ ] discs are often also referred to as the thin and thick discs because the stellar vertical distribution is better fit by a double exponential rather than a single one. However, this doesn't allow one to assign a star to either the thin or thick disk purely based on its height above the Galactic plane. Therefore, we instead use the chemical definition of the two disks (applying the [ $\alpha/\text{Fe}$ ] nomenclature) as there is a clear bimodal distribution in the chemical plane, allowing stars to be assigned to each of the disc components based on their chemical abundances. For each of the three components,

<sup>4</sup>Nomenclature used to describe the enhancement of  $\alpha$  elements compared to iron in stellar atmospheres

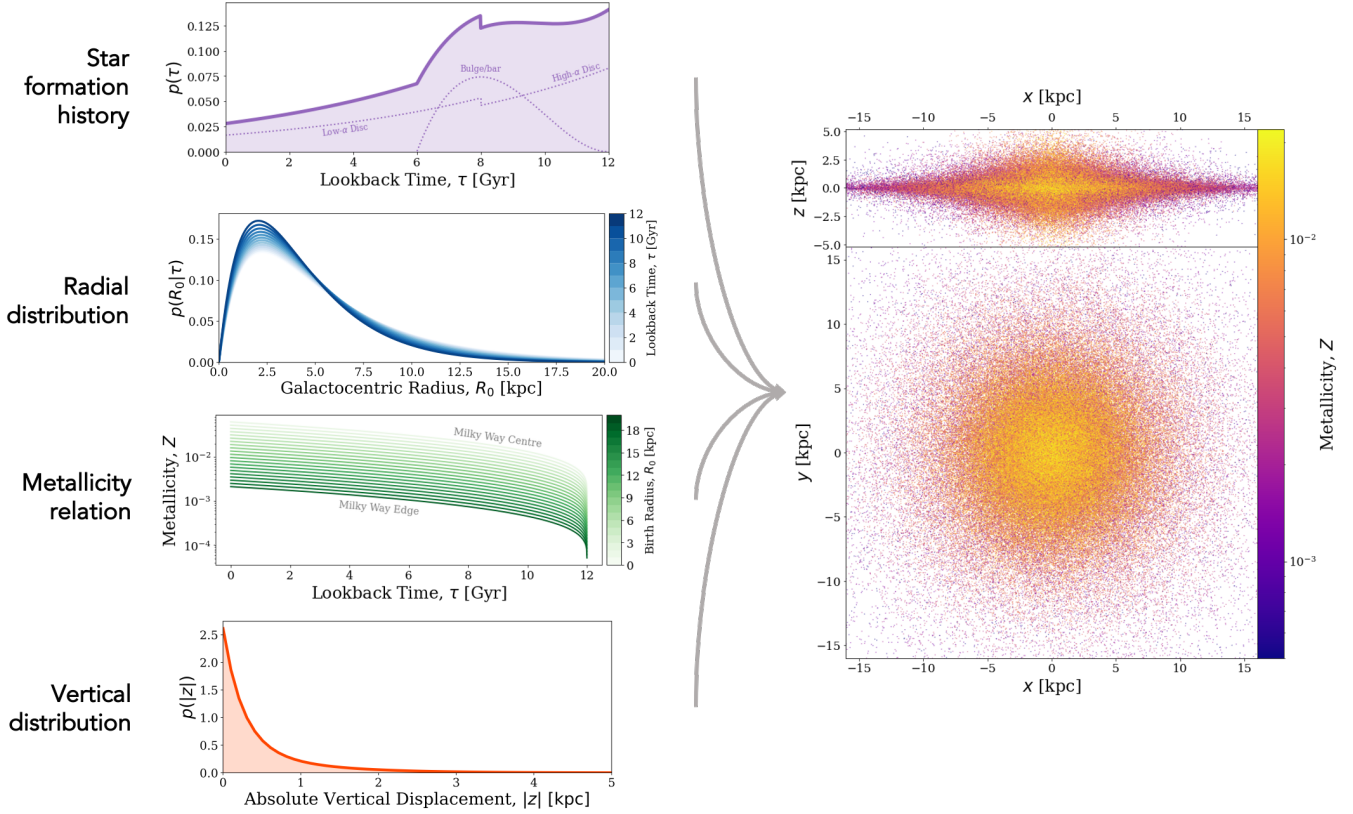


**Figure 1.** A schematic illustrating how we model the Milky Way. The left panel illustrates the different model aspects: star formation history of three galactic components (individually shown in the dotted lines), radial distribution, metallicity-radius-time relation, and height distribution. The right panel shows an example instance of the Milky Way with 250000 binaries shown as points coloured by metallicity. The top panel shows a side-on view and the bottom panel a face-on view.

we use a separate star formation history and spatial distribution, which we combine into a single model, weighting each component by its present-day stellar mass. [Licquia & Newman \(2015\)](#) gives that the stellar mass of the bulge is  $0.9 \times 10^{10} M_{\odot}$  and the stellar mass of the disc is  $5.2 \times 10^{10} M_{\odot}$ , which we split equally between the low- and high-[ $\alpha$ /Fe] discs (e.g., [Snaith et al. 2014](#)).

*Star formation history:* We use an exponentially declining star formation history ([Frankel et al. 2018](#)) (inspired by the average cosmic star formation history) for the combined low- and high-[ $\alpha$ /Fe] discs,

$$p(\tau) \propto \exp\left(-\frac{(\tau_m - \tau)}{\tau_{\text{SFR}}}\right), \quad (2)$$

where  $\tau$  is the lookback time (the amount of time elapsed between the binary's zero-age main sequence and today),  $\tau_m = 12$  Gyr is the assumed age of the Milky Way and  $\tau_{\text{SFR}} = 6.8$  Gyr is the star formation timescale ([Frankel et al. 2018](#)). The two discs form stars in mutually exclusive time periods, such that the high-[ $\alpha$ /Fe] disc forms stars in the early history of the galaxy (8–12 Gyr ago) and the low-[ $\alpha$ /Fe] disc forms stars more recently (0–8 Gyr ago). Both distributions are nor-

malised so that an equal amount of mass is formed in each of the two components over their respective star forming periods.

The star formation history of the bulge/bar of the Milky Way has many uncertainties due to the (1) sizeable age measurement uncertainties at large ages in observational studies, (2) complex selection processes affecting the observed age distributions, and (3) formation mechanisms that are still under debate. However, the central bar (which we assume to dominate here) was shown to contain stars with an extended age range, with most observed stars between 6 and 12 Gyr with a younger tail of ages that could come from the subsequent secular growth of the Galactic bar (e.g., [Bovy et al. 2019](#)). To model the bulge/bar's age distribution more realistically than in previous studies (which assume an old bulge coming from a single starburst), we choose to adopt a more extended star formation history using a  $\beta(2, 3)$  distribution, shifted and scaled such that stars are only formed in the range [6, 12] Gyr. We show these distributions in the top left panel of Fig. 1.

*Radial distribution:* For each of the three components we employ the same single exponential distribution (but

with different scale lengths)

$$p(R) = \exp\left(-\frac{R}{R_d}\right) \frac{R}{R_d^2}, \quad (3)$$

where  $R$  is the Galactocentric radius and  $R_d$  is the scale length of the component. For the low-[ $\alpha$ /Fe] disc, we set  $R_d = R_{\text{exp}}(\tau)$ , where  $R_{\text{exp}}(\tau)$  is the scale length presented in Frankel et al. (2018, Eq. 6)

$$R_{\text{exp}}(\tau) = 4 \text{ kpc} \left(1 - \alpha_{R_{\text{exp}}} \left(\frac{\tau}{8 \text{ Gyr}}\right)\right), \quad (4)$$

where  $\alpha_{R_{\text{exp}}} = 0.3$  is the inside-out growth parameter<sup>5</sup>. This scale length accounts for the inside-out growth of the low-[ $\alpha$ /Fe] disc and hence is age dependent. We assume  $R_d = (1/0.43)$  kpc for the high-[ $\alpha$ /Fe] disc (Bovy et al. 2016, Table 1) and  $R_d = 1.5$  kpc for the bulge/bar component (Bovy et al. 2019). **Note that in this way we have approximated the bulge/bar component as being axi-symmetric, which is sufficient for our purposes.** We show the combination of these distributions in the second panel on the left in Fig. 1.

*Vertical distribution:* Similar to the radial distribution, we use the same single exponential distribution (but with different scale heights) for each component, given by

$$p(|z|) = \frac{1}{z_d} \exp\left(-\frac{|z|}{z_d}\right), \quad (5)$$

where  $z$  is the vertical displacement above the Galactic plane and  $z_d$  is the scale height. We set  $z_d = 0.3$  kpc for the low-[ $\alpha$ /Fe] disc (McMillan 2011) and  $z_d = 0.95$  kpc for the high-[ $\alpha$ /Fe] disc (Bovy et al. 2016). For the bulge/bar, we set  $z_d = 0.2$  kpc (Wegg et al. 2015). We show the combination of these distributions in the bottom left panel of Fig. 1.

*Metallicity-radius-time relation:* To account for the chemical enrichment of star forming gas as the Milky Way evolves, we adopt the relation given by (Frankel et al. 2018, Eq. 7)

$$\begin{aligned} [\text{Fe}/\text{H}](R, \tau) &= F_m + \nabla[\text{Fe}/\text{H}]R \\ &- \left(F_m + \nabla[\text{Fe}/\text{H}]R_{[\text{Fe}/\text{H}]=0}^{\text{now}}\right)f(\tau), \end{aligned} \quad (6)$$

where

$$f(\tau) = \left(1 - \frac{\tau}{\tau_m}\right)^{\gamma_{[\text{Fe}/\text{H}]}} , \quad (7)$$

$F_m = -1$  dex is the metallicity of the gas at the center of the disc at  $\tau = \tau_m$ ,  $\nabla[\text{Fe}/\text{H}] = -0.075 \text{ kpc}^{-1}$  is the

<sup>5</sup>We find that  $R_{\text{exp}}(\tau) = 4$  kpc fits the data well and adopt this value rather than the 3 kpc quoted in Frankel et al. (2018), which was a fixed parameter (not a fit).

metallicity gradient,  $R_{[\text{Fe}/\text{H}]=0}^{\text{now}} = 8.7$  kpc is the radius at which the present day metallicity is solar and  $\gamma_{[\text{Fe}/\text{H}]} = 0.3$  sets the time dependence of the chemical enrichment. We convert this to the representation of metallicity that we use in this paper by applying (e.g. Bertelli et al. 1994)

$$\log_{10}(Z) = 0.977[\text{Fe}/\text{H}] + \log_{10}(Z_\odot). \quad (8)$$

Although Frankel et al. (2018) only fit this model for the low-[ $\alpha$ /Fe] disc, we also use this metallicity-radius-time relation for the high- $\alpha$  disc and the bar, but focusing on the chemical tracks more representative to the inner disc and large ages. Sharma et al. (2020) showed that using a simple continuous model for both the low- and high-[ $\alpha$ /Fe] discs, the Milky Way abundance distributions could be well reproduced. Empirically, the abundance tracks in the [ $\alpha$ /Fe]-[Fe/H] plane (and other elements) of the stars in the bulge/bar follow the same track as those of the old stars in the Solar neighbourhood (Griffith et al. 2021; Bovy et al. 2019, Fig. 7.), which motivates our modelling choice to use the same metallicity-radius-time relation.

#### 2.2.2. Combining population and galaxy synthesis

For each Milky Way instance, we randomly sample the following set of parameters

$$\mathbf{g}_j = \{\tau, R, Z, z, \theta\} \quad (9)$$

for  $j = 1, 2, \dots, N_{\text{MW}}$ , where we set  $N_{\text{MW}} = 2 \times 10^5$ ,  $\tau, R, Z$  and  $z$  are defined and sampled using the distribution functions specified in Section 2.2.1,  $\theta$  is the azimuthal angle sampled uniformly on  $[0, 2\pi]$  and  $Z$  is the metallicity. Fig. 1 shows an example of a random Milky Way instance created with these distributions. This shows how these distributions translate to positions and illustrates the gradient in metallicity over radius.

We match each set of galaxy parameters  $\mathbf{g}_j$ , to a random set of binary parameters  $\mathbf{b}_{Z,i}$ , by drawing a binary from the closest metallicity bin to the metallicity in  $\mathbf{g}_j$ . If the metallicity in  $\mathbf{g}_j$  is below the minimum COMPAS metallicity bin ( $Z = 10^{-4}$ ), we use this minimum bin. If the metallicity in  $\mathbf{g}_j$  is above the maximum COMPAS metallicity bin ( $Z = 0.03$ ), we use a randomly selected bin from the five highest metallicity bins<sup>6</sup>.

Each binary is likely to move from its birth orbit. Although all stars in the Galactic disc experience radial migration (Sellwood & Binney 2002; Frankel et al.

We spread the binaries over the five highest bins, rather than just the highest bin, as we found that using a single bin led to unphysical artifacts in our results. These artifacts arose because the small population of binaries in the highest bin were oversampled.

430 DCOs generally experience stronger dynamical  
 431 evolution as a result of the effects of both Blaauw kicks  
 432 (Blaauw 1961) and natal kicks (e.g. Hobbs et al. 2005).  
 433 The magnitude of the systemic kicks are typically  
 434 small compared to the initial circular velocity of a bi-  
 435 nary at each Galactocentric radius. Therefore, we ex-  
 436 pect that kicks will not significantly alter the overall  
 437 distribution of their positions (see however, e.g., Brandt  
 438 & Podsiadlowski 1995; Abbott et al. 2017b). Given this,  
 439 and for the sake of computational efficiency, we do not  
 440 account for the displacement due to systemic kicks in  
 441 our analysis.

### 442 2.3. Gravitational wave detection

443 We use the Python package **LEGWORK** (Wagg et al.  
 444 2021) to evolve binaries and calculate their LISA de-  
 445 tectability. For a full derivation of the equations given  
 446 below see (Wagg et al. 2021, Section 3), or the LEG-  
 447 WORK documentation [\[2\]](#).

#### 448 2.3.1. Inspiral evolution

449 Each binary loses orbital energy to gravitational waves  
 450 throughout its lifetime. This causes the binary to shrink  
 451 and circularise over time. In order to assess the de-  
 452 tectability of a binary, we need to know its eccentricity  
 453 and frequency at the time of the LISA mission. For each  
 454 binary in our simulated Milky Way, we know that the  
 455 time from DCO formation to today is  $\tau - t_{\text{evolve}}$  and that  
 456 the initial eccentricity and semi-major axis are  $e_{\text{DCO}}$  and  
 457  $a_{\text{DCO}}$ . We find the eccentricity of the binary at the start  
 458 of the LISA mission,  $e_{\text{LISA}}$ , by numerically integrating  
 459 its time derivative (Peters 1964, Eq. 5.13) given the ini-  
 460 tial conditions. This can be converted to the semi-major  
 461 axis at the start of LISA,  $a_{\text{LISA}}$  (Peters 1964, Eq. 5.11),  
 462 which in turn gives the orbital frequency,  $f_{\text{orb,LISA}}$ , by  
 463 Kepler's third law since we know the component masses.

#### 464 2.3.2. Binary detectability

We define a binary as detectable if its gravitational wave signal has a signal-to-noise ratio (SNR) of greater than 7 by the end of the LISA mission (e.g. Breivik et al. 2020; Korol et al. 2020). The sky-, polarisation- and orientation-averaged signal-to-noise ratio,  $\rho$ , of an inspiraling binary can be calculated with the following (e.g. Finn & Thorne 2000)

$$\rho^2 = \sum_{n=1}^{\infty} \int_{f_{n,i}}^{f_{n,f}} \frac{h_{c,n}^2}{f_n^2 S_n(f_n)} df_n, \quad (10)$$

where  $n$  is a harmonic of the gravitational wave signal,  $f_n = n \cdot f_{\text{orb}}$  is the frequency of the  $n^{\text{th}}$  harmonic of the gravitational wave signal,  $f_{\text{orb}}$  is the orbital frequency,  $S_n(f_n)$  is the LISA sensitivity curve at frequency  $f_n$  (e.g.

Robson et al. 2019) and  $h_{c,n}$  is the characteristic strain of the  $n^{\text{th}}$  harmonic, given by (e.g. Barack & Cutler 2004)

$$h_{c,n}^2 = \frac{2^{5/3}}{3\pi^{4/3}} \frac{(G\mathcal{M}_c)^{5/3}}{c^3 D_L^2} \frac{1}{f_{\text{orb}}^{1/3}} \frac{g(n,e)}{nF(e)}, \quad (11)$$

where  $D_L$  is the luminosity distance to the source,  $f_{\text{orb}}$  is the orbital frequency,  $g(n,e)$  and  $F(e)$  are given in Peters & Mathews (1963) and  $\mathcal{M}_c$  is the chirp mass, defined as

$$\mathcal{M}_c = \frac{(m_1 m_2)^{3/5}}{(m_1 + m_2)^{1/5}}. \quad (12)$$

Note that increasing the length of the LISA mission allows more time for a DCO to evolve over the mission. Therefore the frequency limits in Eq. 10 are dictated by the LISA mission length. The SNR generally scales as  $\sqrt{T_{\text{obs}}}$  (with exceptions for sources very close to merging) and thus the SNR of a typical source in a 10-year LISA mission is approximately 1.58 ( $=\sqrt{10/4}$ ) times stronger than in a 4-year mission.

We use **LEGWORK** (Wagg et al. 2021) to calculate the signal-to-noise ratio for each binary and the package ensures that enough harmonics are computed for each binary such that the error on the gravitational-wave luminosity remains below 1%.

#### 478 2.3.3. Detection rate calculation

For each physics variation model and DCO type, we first convert the COMPAS simulation results into a total number of DCOs in the Milky Way,  $N_{\text{DCO}}$ . We do this by integrating the full mass and period distributions and stars and normalising to the total Milky Way mass. For more details see Appendix B.

We then determine the fraction of binaries that are detectable in each Milky Way instance by summing the adaptive importance sampling weights of the binaries that have an SNR greater than 7, and dividing by the total weights in the simulation. We multiply this fraction by  $N_{\text{DCO}}$  to find a detection rate (which we write as a total number of detections per LISA mission)

$$N_{\text{detect}} = \frac{\sum_{i=0}^{N_{\text{MW}}} w_i \phi(i)}{\sum_{i=0}^{N_{\text{MW}}} w_i} N_{\text{DCO}}, \quad (13)$$

where  $\phi(i) = 1$  if a binary is detectable and 0 otherwise. We calculate the detection rate by Monte Carlo sampling 2500 Milky Way instances (each containing 200,000 DCOs) for each DCO type and every physics variation in order to obtain values for the uncertainty on the expected detection rate.

### 491    3. RESULTS I - PREDICTIONS FOR LISA 492    SOURCES

493    In this section we present our predictions for the popu-  
494    lation of detectable LISA sources for our fiducial model.  
495    In total we expect, on average, 124 detections in a 4-  
496    year LISA mission, of which 74, 42 and 8 are BHBHs,  
497    BHNSs and NSNSs respectively, based on our fiducial  
498    simulations. In the remainder of this section, we discuss  
499    where the sources are expected relative to LISA’s sensi-  
500    tivity curve (Sec. 3.1), their properties (Sec. 3.2), their  
501    locations in the Milky Way (Sec. 3.3), their formation  
502    channels (Sec. 3.4) and finally we discuss the expected  
503    SNR and how accurately we expect that the parameters  
504    can be measured (Sec. 3.5). Note that all results shown  
505    in this section are based on our fiducial simulations. A  
506    discussion of the impact of variations in the physics as-  
507    sumptions is provided in Sec. 4.

#### 508    3.1. *The LISA sensitivity curve and the population of 509    detectable sources*

510    We show the expected LISA sensitivity curve (Rob-  
511    son et al. 2019) in Fig. 2, which includes the confu-  
512    sion noise arising from the Galactic WDWD popula-  
513    tion, and overplot our predictions for the distribution  
514    of detectable sources. Eccentric systems emit gravita-  
515    tional waves in multiple harmonic frequencies ( $n f_{\text{orb}}$ ,  
516    with  $n = 2, 3, \dots$ ). We choose to plot them at the  $x$ -  
517    coordinate that corresponds to the frequency of the har-  
518    monic that individually accumulates the largest SNR.  
519    For circular systems, the  $x$ -coordinate simply corre-  
520    sponds to  $2f_{\text{orb}}$ . The  $y$ -coordinate indicates the strength  
521    of the signal (or to be more precise, the amplitude spec-  
522    tral density, ASD), including the contribution from *all*  
523    harmonics.

524    For reference, we show dotted lines to indicate where  
525    a hypothetical binary system would reside assuming a  
526    given distance from earth (diagonal lines) and a fixed  
527    remaining inspiral time (vertical lines). For each line we  
528    assume the binary is circular and has a chirp mass equal  
529    to the average of the sample ( $\langle \mathcal{M}_c \rangle$ , annotated in each  
530    panel). We also overplot the LISA verification binaries  
531    (star symbols, Kupfer et al. 2018).

532    We observe several features in Fig. 2 that are worth  
533    discussing and explaining. We note that some of these  
534    have also been described in earlier studies (see Sec. 6).  
535    Firstly, we note the empty band that separates the LISA  
536    sensitivity curve and the detectable population. This is  
537    the result of the criteria for detection where we require  
538     $\text{SNR} > 7$ .

539    We further note that the detectable population is con-  
540    centrated on the left side of LISA’s sensitivity window.

541    The peak is located at a frequency of about 0.4 mHz,  
542    which is much lower than the frequency where LISA will  
543    be most sensitive (about 10 mHz). This can be under-  
544    stood from the acceleration of inspiraling DCOs as they  
545    evolve towards higher frequencies. DCOs typically form  
546    with wide orbits (low frequencies) that would not be  
547    detectable yet. Their orbits shrink as they lose angular  
548    momentum in the form of gravitational waves leading to  
549    an increase of their orbital frequency until they become  
550    detectable. These systems are increasingly rare because  
551    they evolve faster and faster towards higher frequency as  
552    the inspiral accelerates, even though the signal emitted  
553    by a more compact binary is stronger (Peters 1964). The  
554    vertical grid lines show these rapidly decreasing inspiral  
555    times at increasing frequencies. Most of the population  
556    is thus expected to reside at low frequencies.

557    In the lower three panels, we show the contributions  
558    of the different types of sources. Comparing them, one  
559    can observe the shift in the frequency at which the peak  
560    is located, at 0.3 mHz, 0.7 mHz and 1 mHz for BHBH,  
561    BHNS and NSNS systems respectively. This is a result  
562    of the difference in chirp mass. A higher mass system  
563    can emit at lower frequency and still produce the min-  
564    imum SNR needed for detection. We note that this ef-  
565    fect can be used to distinguish the heavier DCOs that  
566    we discuss in this work from WDWD systems, at least  
567    probabilistically (see Sec. 5.1.1). In the same way, this  
568    also explains the offset in frequency between the pop-  
569    ulation of sources we predict and the LISA verification  
570    binaries.

571    Inspecting the dotted reference lines, we note that the  
572    peak of the density distribution of observable sources co-  
573    incides with the location expected for circular systems  
574    at 8 kpc, which is the distance to the centre of the Milky  
575    Way. As can be seen best in the lower panels, the ref-  
576    erence lines for 0.1 and 30 kpc enclose the majority of  
577    systems, as expected given the dimensions of the Milky  
578    Way.

579    There is a distinct subpopulation of binaries, most  
580    clearly visible in the lower panels as an offshoot that  
581    extends downwards to ASDs of  $10^{-19} \text{ Hz}^{-1/2}$ , especially  
582    around 2 mHz. This offshoot is almost uniquely com-  
583    posed of eccentric binaries, as can be seen in Fig. F2,  
584    which shows a similar figure but colouring individual  
585    systems by their eccentricity. This can also be seen,  
586    albeit indirectly, from the contour lines shown in the  
587    bottom panels of Fig. 2, which encompass 90% of the  
588    *circular* sources in each population. This contour does  
589    not include the offshoot. We conclude that eccentric  
590    sources occupy a very different region in this diagram.

#### 591    3.2. *Properties of the detectable systems*

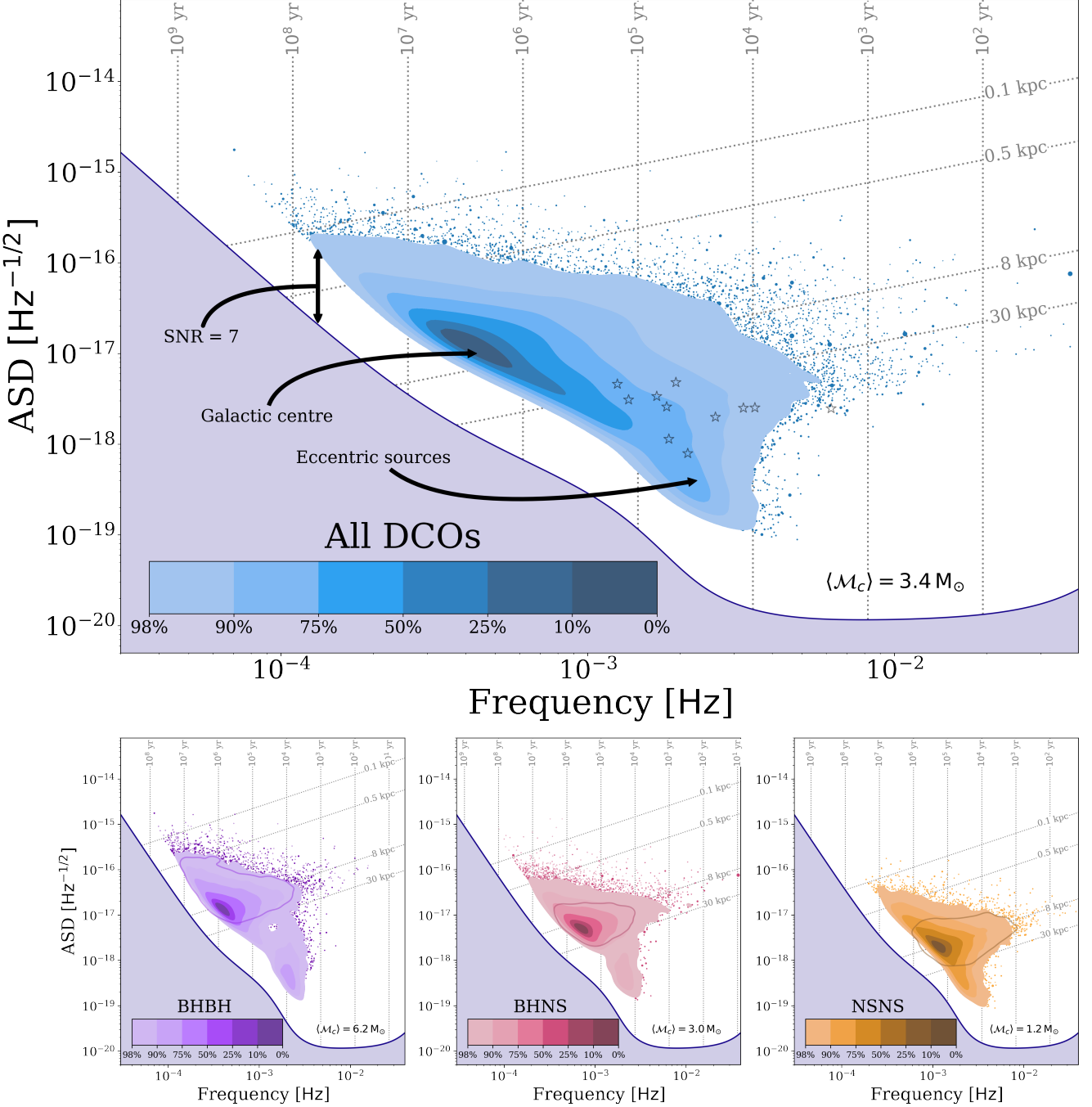


**Figure 2.** The LISA sensitivity curve is shown together with the density distribution of the characteristic strain and the dominant frequency for all detectable sources in our simulations (top) and separated by type (bottom). Contours show the percentage of the population enclosed. The remaining 2% of the population is shown as dots with a size that scales with the sampling weight. To guide the interpretation, we show reference lines marking where a circular binary would reside for a given distance (diagonal line) and remaining inspiral time (vertical lines), assuming an average chirp mass  $\langle M_c \rangle$ , orientation and sky location. The coloured lines in the bottom panels show a contour that encloses 90% of the population that is circular. LISA verification binaries are overplotted in the top panel (star symbols). See also Fig. F2 and Sec. 3.1 for a discussion.

In Fig. 3, we show the 1D distribution of several individual parameters of the population of detectable binaries together with the 1- and 2- $\sigma$  uncertainties obtained via bootstrapping. These uncertainties represent the fluctuations in our results over different random instances of the Milky Way. The distributions shown here are approximated by kernel density estimators, corrected for edge effects by mirroring the sample (Schuster 1985).

*Orbital Frequency*—The orbital frequency distributions for BHBHs, BHNSs and NSNSs (Fig. 3a) peak at progressively increasing frequencies. As mentioned in Sec. 3.1, this is because a higher mass DCO at the same distance and eccentricity requires a lower frequency to produce the same signal-to-noise ratio and thus be detected. The distributions appear nearly symmetric, **but the left tail of the distribution is more populated, especially for the BHBHs.** This is due to the contribution of highly eccentric binaries, which are most abundant in the BHBH population. These systems are still detectable by LISA, despite their low orbital frequency, as the high eccentricity means that the majority of the GW signal is emitted at higher harmonics, where LISA is more sensitive.

*Black Hole Mass*—In Fig. 3b, we show the distribution of **primary** black hole masses for BHNS and BHBH systems. **The BHNS distribution shows a bimodality. This is due to the bimodal mass ratio distribution (see Fig. 3c) since most NS components have approximately the same mass.**

For both the BHBHs and BHNSs, we see that the black hole mass distribution favours low masses. About 90% of BHs have masses below  $12 M_{\odot}$ , in our fiducial simulations shown here. This is in contrast with observations from ground-based GW detectors, where heavy BHs with masses of about  $30 M_{\odot}$  and higher have been common. There are two main reasons for this discrepancy. First, the population of BHs in the Milky Way (and, in particular, those detectable by LISA due to their recent formation times, see Fig. 3e) primarily come from progenitors that formed from high metallicity gas according to our simulations. Stellar winds are stronger at high metallicity leading to increased mass loss. This affects the mass of the most massive black holes that can be formed (Belczynski et al. 2010). Secondly, ground-based detectors are strongly biased towards high mass systems, since they can be detected out to larger distances and thus a greater volume is probed. In contrast, LISA has no such bias and is, in principle, sensitive to inspiraling DCOs throughout the entire Milky Way regardless of their mass, as long as we catch them when

they are emitting in the LISA band. For this reason, LISA is more likely to detect the more common lower mass DCOs.

We also note that our BH mass distribution extends down below  $5 M_{\odot}$  to  $2.5 M_{\odot}$  which is our fiducial maximum neutron star mass. The BHs in this simulation fill the so-called “lower mass gap” marked as a grey band (Özel et al. 2010; Farr et al. 2011), see also Shao & Li (2021) who recently also pointed this out. This prediction is sensitive to adopted model for fallback during the SN explosion as we discuss this further in Section 4.2.1.

*Mass Ratio*—The mass ratio distributions for each DCO type are very distinct from one another, as can be seen in Fig. 3c. The majority of NSNSs have a mass ratio close to unity, with 90% of systems having  $q > 0.8$ , where  $q \equiv m_2/m_1$ . The reason for the concentration around equal masses is that most NSs are formed either through electron-capture supernovae (ECSN) or from low mass stars in our simulations. We assume a remnant mass for any NS formed through ECSN of  $1.26 M_{\odot}$  (see Sec. A.2). The remnant mass prescription that we use assumes a fixed fallback mass for any star with a CO core mass less than  $2.5 M_{\odot}$ , such that many NSs end up with an identical mass of  $1.278 M_{\odot}$  (see Fryer et al. 2012, Eq. 19). This means that many NSs are formed with equal masses and hence we see a mass ratio distribution peaked around unity.

In contrast, only 8% of detectable BHBHs are formed with  $q > 0.8$  and the distribution peaks around  $q = 0.4$ . We find that the strong stellar winds in our (typically high-metallicity) progenitors are the reason behind this, **though we still would not expect a significant number of detections at higher mass ratios since the intrinsic merging BHBH population tends to have less equal mass ratios (e.g. van Son et al. 2021, Fig. 8).**

BHBHs with unequal masses typically come from progenitors that also had more extreme mass ratios at birth ( $90$  and  $30 M_{\odot}$  are typical for the progenitors of detectable BHBH systems in our simulations). The primary in such systems experiences strong mass loss by winds before filling its Roche lobe. This mostly happens during its early hydrogen-shell burning phase. The wind mainly reduces the mass of the envelope, but does not have a very strong effect on the core. By the time the primary fills its Roche lobe, it has become less massive and the mass ratio is closer to one. This favours stable mass transfer **and most detectable BHBHs form through stable mass transfer (see Section. 3.4).** The massive core of the primary star typically becomes the more massive BH. Accretion on the secondary star

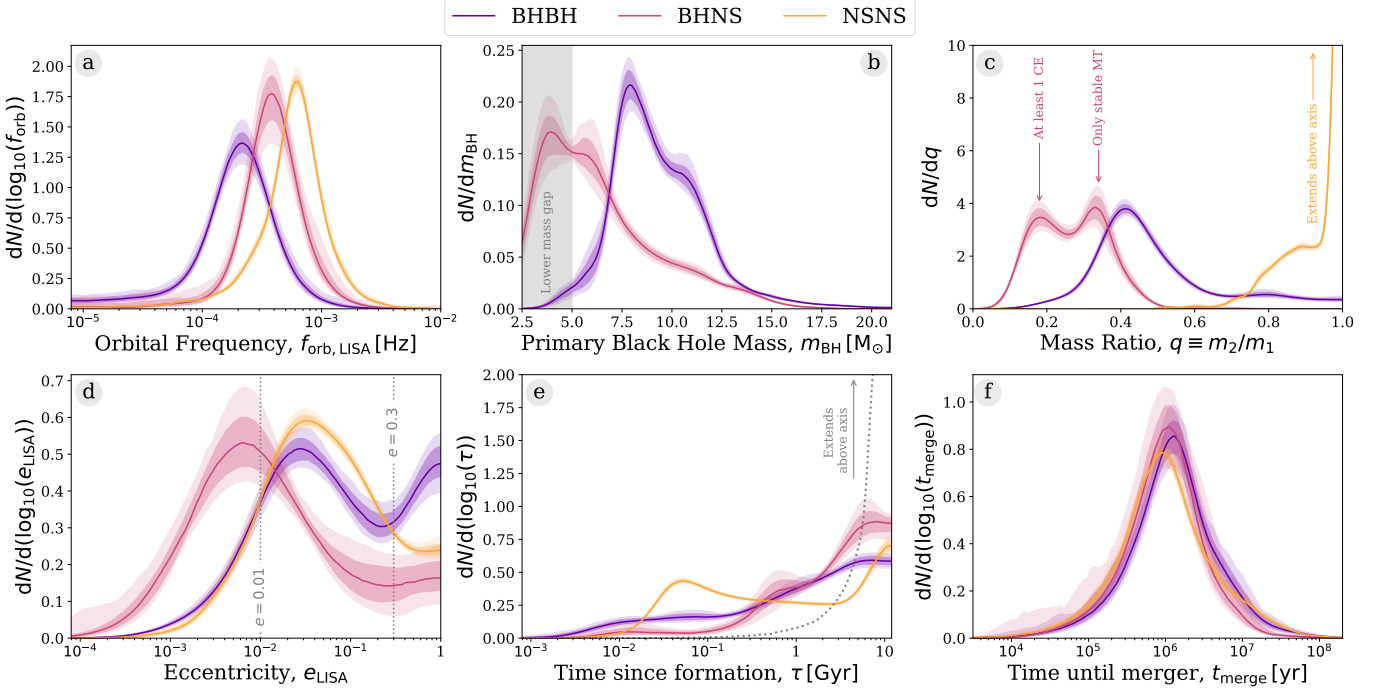


**Figure 3.** Properties of detectable systems for a 4-year LISA mission in our fiducial model. Each panel shows a kernel density estimator for a single property, coloured by DCO type. Each curve has been individually normalised. The shaded areas show the 1- and 2- $\sigma$  sampling uncertainties (obtained via bootstrapping). The dotted line in panel e shows the star formation history we have assumed in our Milky Way model. See Sec. 3.2 for a discussion.

is limited and the secondary eventually provides the less massive black hole.

At the same time, stellar wind mass loss disfavours the formation of black holes with comparable masses. Such systems would have originated from progenitors that also started with comparable masses. The rather massive secondaries in these systems (especially after they accreted from the primary) experience very strong stellar wind mass loss due to LBV-like eruptions. This limits the amount by which they can expand (e.g. van Son et al. 2021). At the same time, wind mass loss (and also stable and more conservative mass transfer in these systems) lead to widening of the orbit. Both effects, the reduced expansion and increased widening of the orbit, tend to prevent the secondaries from being able to fill their Roche lobe. This thus limits the number of systems that experience the reverse mass transfer or common-envelope phase needed to shrink the orbits and make them tight enough to be detected as gravitational-wave sources.

We find that detectable BHNSs have even more unequal mass ratios. Moreover, the mass ratio distribution is bimodal, where the two peaks arise from two distinct formation scenarios. Around two thirds of detectable BHNSs experience at least one common-envelope event, whilst the last third are formed through only stable mass

transfer. The first peak at  $q = 0.18$  is from systems that experience at least one common-envelope phase and occurs at the expected mass ratio, which approximately follows the mean BH mass ( $\sim 6.5 M_\odot$ ) and NS mass ( $\sim 1.2 M_\odot$ ). Yet we also see a second peak at higher mass ratios around  $q = 0.34$ , which arises from the fraction of the population that underwent only stable mass transfer phases. The stability of mass transfer depends on the mass ratio, preferentially forming systems with more equal masses, i.e. at higher  $q$ .

*Eccentricity*—In Fig. 3d we show the eccentricity distributions. We find that most systems (73%) will have eccentricities larger than 0.01 during the LISA mission, which should in principle be detectable according to Nishizawa et al. (2016). This means that we will potentially be able to use eccentricity to distinguish these sources from WDWDs, which are expected to have little to no eccentricity (see Sec. 5.1.1). We note that several previous studies assumed all systems to be circular when calculating the detection rates (e.g. Liu & Zhang 2014; Lamberts et al. 2018; Sesana et al. 2020). We discuss the impact of this assumption in Section 6.

For systems with eccentricities higher than  $e \gtrsim 0.3$ , most gravitational wave energy is emitted in higher harmonics. Such systems are more rare, but we find them to be significant among the BHBH population, where

they account for 21% of systems. Detectable BHBHs in our simulation (and, in particular, those that are eccentric) are primarily systems formed through the stable mass transfer channel (see Fig. F1). These systems are still relatively wide (compared to those formed through the CE channel) immediately prior to formation of the second BH, which makes them more easily affected by kicks. If the kick is oriented roughly in opposite direction to the orbital motion and has a velocity that is of similar magnitude as the orbital velocity, it will lead to the formation of a highly eccentric system.

It is rare to get such a “lucky kick”, but there are a few effects that favour this for BHBHs. The kicks of BHs are reduced by fallback and they are thus less likely to disrupt the system. Moreover, because of their higher masses, BHBHs can be observed already at lower orbital frequencies. This means that they have not had as much time to circularise and so still have significant eccentricity by the time of the LISA mission. Finally, LISA favours the detection of eccentric systems, if all other properties are held fixed. This is because the gravitational-wave emission is stronger (Eq. C2) and the energy is emitted at higher frequencies (Peters & Mathews 1963, Eq. 20) where LISA is more sensitive.

The lower abundance of highly eccentric systems among the NSNS and BHNS systems may seem counterintuitive since neutron stars are lower mass and would be more strongly affected by natal kicks, which one may expect to lead to more eccentric systems. However, the majority of NSs in our simulations are formed through ECSN and USSN and for these types of supernovae we draw from a Maxwellian with  $\sigma_{\text{rms}}^{1D} = 30 \text{ km s}^{-1}$ . Thus the kicks received by NSs in our simulations are often much smaller than for BHs.

*Time since formation*—In Fig. 3e we show how long ago the LISA detectable DCOs formed. Star formation was highest at early times 6 – 12 Gyr ago, after which it declined. In contrast, the LISA detectable DCOs primarily formed in the relatively *recent* history of our Milky Way, about 2 Gyr ago. This reflects the fact that binaries in our simulation typically take about a Gyr to merge.

When comparing the distribution of formation times for the three different DCO types we see that NSNSs are most strongly concentrated at recent times, followed by BHBHs and then BHNSs. To understand this it is helpful to consider how the inspiral time scales with various parameters (Peters 1964)

$$t_{\text{inspiral}} \propto \frac{a^4}{(m_1 + m_2)^3} \cdot \frac{q}{(1+q)^2} \cdot (1 - e^2)^{-7/2}. \quad (14)$$

The inspiral time depends most strongly on the separation at DCO formation,  $a$ , and this is where the three

types also differ most strongly (see Fig. F3). The detectable NSNS systems have the tightest orbits at DCO formation. The median of the distribution of separations at DCO formation,  $\langle a_{\text{DCO}} \rangle_{\text{med}}$ , relate as 8:3:1 for detectable BHBH:BHNS:NSNS in our simulations. This results in increase of the inspiral time by a factor of about 4000:80:1.

**The distribution of separations at DCO formation** is also the reason that the time since formation for NSNSs shows a bimodality. For NSNSs, the separation at DCO formation peaks around  $2 \times 10^{-2} \text{ AU}$  but the distribution has a second population that extends to much lower separations relative to the the BHNS and BHBH distributions. It is this population of shorter separations that corresponds to the NSNSs that were formed more recently (within the last 100 Myr).

The total masses affect the inspiral time to the third power and this where the heavier BHBH systems are favoured. The median total masses differ by ratios of 6:4:1 for detectable BHBH:BHNS:NSNS in our simulations, impacting the inspiral times such that they are a factor of 200:60:1 shorter, partially counteracting the effect of the separations. The term depending on the mass ratio  $q$  only varies by about 30% for the mass ratio ranges considered here and so is not of interest. The eccentricity term is not of importance for mildly eccentric systems,  $f(e_{\text{DCO}} \leq 0.3) \leq 1.4$  but of large importance for the very eccentric  $f(e_{\text{DCO}} \geq 0.9) \geq 300$ . The fraction of highly eccentric systems with  $e_{\text{DCO}} > 0.9$  is 33%, 16%, and 8% of for BHBH, BHNS and NSNS respectively, see also Fig. F3.

We conclude that the shorter median separations at DCO formation are the main reason why NSNS are most strongly peaked at short delay times. They are followed by BHBHs rather than BHNSs due to the high masses and substantial eccentricities of BHBHs.

*Time until merger*—Fig. 3f shows the remaining time until merger for each of the DCO types at the start of LISA mission. The distributions are strikingly similar and peak with merger times of around a Myr.

The merger time is a function of the mass, frequency and eccentricity of the sources, such that more massive, higher frequency and more eccentric sources merge faster (Peters 1964, Eq. 5.14). So, despite the fact that each DCO type often has higher values in any one of these properties, the convolution of all three tends to negate the differences. For example, NSNSs have the highest orbital frequencies and are mildly eccentric whilst BHNSs have moderate orbital frequencies and are more circular. However, BHNSs are more massive in

Component	Formation	Detectable			
		All	BHBH	BHNS	NSNS
Low- $\alpha$ disc	42.5%	86%	89%	82%	85%
High- $\alpha$ disc	42.5%	6%	5%	8%	12%
Bulge/bar	15.0%	8%	6%	10%	3%

**Table 1.** Percentage of systems in each Galactic component.

general and so the overall merger times are distributed very similarly for both DCO types.

### 3.3. Distribution in the Milky Way

For our Milky way model we consider three different components, a low-[ $\alpha$ /Fe] (“thin”) disc, an older high-[ $\alpha$ /Fe] (“thick”) disc and a bulge/bar (see Sec. 2.2). In Table 1 we summarise the number of detections originating from each of these components. Despite the fact that only 42.5% of systems are formed in the low-[ $\alpha$ /Fe] disc, we find that 86% of the detections originate from this component. This is because most detectable systems were formed relatively recently (see Fig. 3e) and so the high-[ $\alpha$ /Fe] disc and bulge are effectively too old to contribute many detectable systems. Nevertheless, we do find a significant fraction of detectable systems originate in the high-[ $\alpha$ /Fe] disc and bulge, indicating that it is still important to include these components, as was ignored in some earlier works (see Sec. 6).

In the top panel of Fig. 4, we show the density distribution for detectable DCOs in the galaxy. We see that most detectable sources are concentrated towards the Galactic centre, with a strong bias towards sources that are on our side of the Milky Way in the vicinity of the solar system (indicated with the  $\odot$  symbol). In principle, systems are detectable out to large distances of about 20 kpc and more, although they become increasingly rare, as can be seen from the 95% contour.

The differences between different DCO types can be seen more clearly in the bottom panel of Fig. 4 where we show the distribution of the distances,  $D$ , from earth to the detectable systems. Each distribution peaks around 8 kpc, which is the distance to the centre of the Milky Way. The distribution for BHBH and BHNS systems follow a very similar shape, favouring the detection of systems with distance  $< 8$  kpc, but with a tail extending out to about 20 kpc.

The distribution for NSNS stands out by being flatter, making them more common nearby and, surprisingly, also at larger distances compared to the stellar density. This may seem counter intuitive as one might naively expect the less massive NSNS systems would not be observable out to larger distances than the more massive BHNS and NSNS systems. To understand the differ-

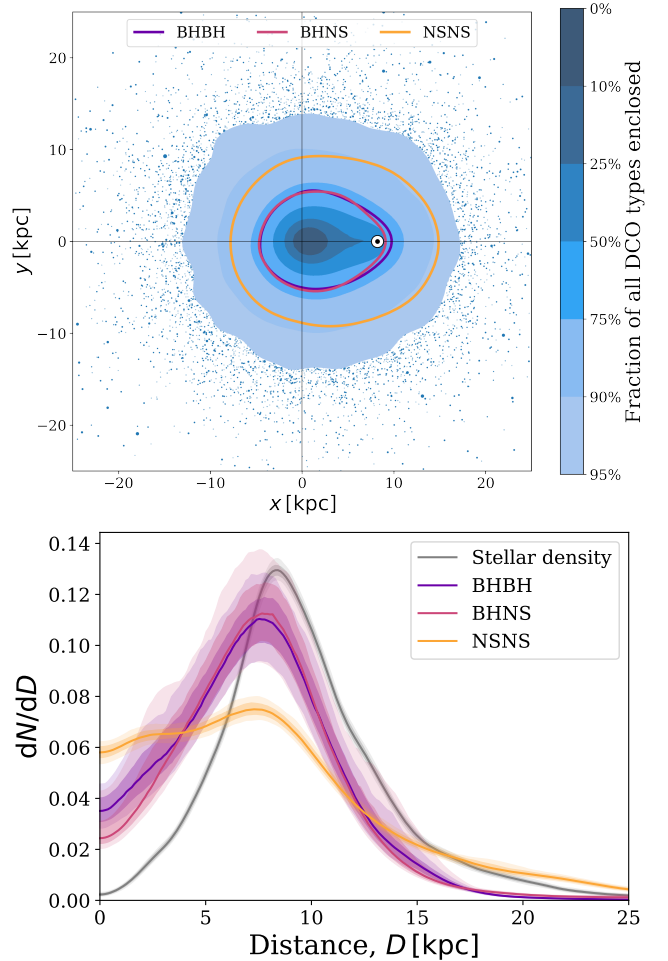


**Figure 4. Top:** A face-on view of the Galactic density distribution for detectable DCOs. We show the density distribution for the top 95% of the sources, the rest are indicated by scatter points whose sizes correspond to their sampling weights. The coloured lines show the 75% contour for each of the individual DCO types. The large cross passes through  $(0, 0)$  and helps to highlight the bias towards the position of the sun, which is indicated by the  $\odot$ . **Bottom:** As Fig. 3, but for the luminosity distance.

ences we need to consider not only the mass distribution of binaries, but also their eccentricity and frequency distributions. Since, each parameter contributes to the calculation of the SNR (and thus affects the maximum distance at which systems can be detected).

The reason that the NSNSs are favoured at higher distances is that the NSNS population has the highest fraction of “mildly” eccentric systems ( $0.01 < e < 0.03$ ). In contrast, the BHNS population has a much higher fraction of effectively circular systems ( $e < 0.01$ ), which emit weaker gravitational waves compared to equivalent eccentric systems. Therefore, despite their typically higher masses, the distance at which a BHNS source is

detectable is generally lower than for the mildly eccentric NSNS.

Conversely, the BHBH population has the highest fraction of highly eccentric systems ( $e > 0.3$ ). Although one may naively expect that this would result in stronger signals (and so further distances), for a system to have these high eccentricities in LISA, it must still be early in its evolution (otherwise it would have circularised) and thus have a low orbital frequency. The result of this is that highest eccentricity systems tend to have lower SNRs and so cannot be detected at large distances.

Overall we see that the eccentricity distribution of NSNSs occupies a “sweet spot” where the gravitational wave power is increased compared to circular systems, but it isn’t too high that the frequency is significantly impacted. This means that NSNSs can be seen out to the largest distances of the three DCO types.

#### 3.4. Formation channels

In our fiducial model, approximately two thirds of detectable BHBHs are formed through the ‘only stable mass transfer’ channel, whilst the remaining third are primarily formed through the ‘classic’ CE channel, in which the first phase of mass transfer is stable whilst the second is unstable and results in a common-envelope event. Detectable BHNSs follow an inverse pattern, such that around two thirds are formed through the classic channel and the rest are mainly formed through only stable mass transfer.

In contrast, detectable NSNSs are very rarely formed through only stable mass transfer. Approximately half of systems are formed through the ‘classic’ channel and the rest are formed through a double-core common-envelope event (Brown 1995) where both progenitors evolve on a similar timescale and initiate a double-core common-envelope event whilst they are on the giant branch. All detectable DCOs show a small fraction of systems are formed through a channel that does not fit into the other categories and hence are labelled ‘other’. These systems tend to be formed through ‘lucky’ supernova kicks that happen to shrink the binary significantly by chance.

The fraction of detectable DCOs that are formed through different formation channels in the other model variations are shown Fig. F1, where the first column in the plot corresponds to the fiducial model that we described above.

#### 3.5. How accurately will we be able to infer the parameters of detected systems?

So far we have discussed the properties of the all detectable sources. However, only for a subset of systems

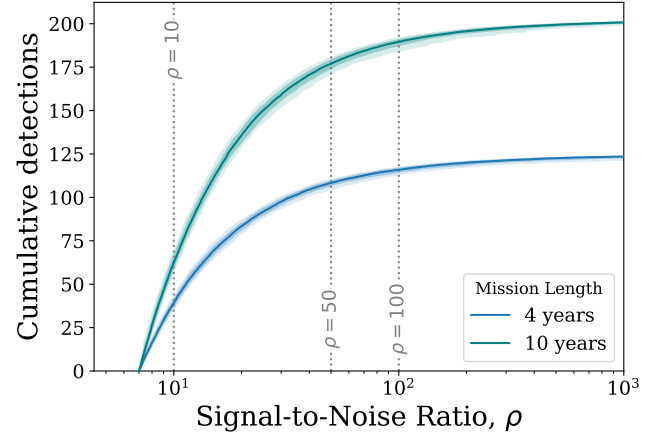


**Figure 5.** Cumulative number of LISA detections with a given signal-to-noise ratio. Colours indicate LISA mission length and shading shows 1- and 2- $\sigma$  uncertainties (obtained via bootstrapping).

we expect to get high enough SNR to obtain accurate and useful measurements of these parameters. Below we discuss the expected SNR distribution and the typical uncertainties expected for the most relevant parameters, namely, the chirp mass and sky localisation.

*Signal-to-noise ratio*—In Fig. 5 we show the cumulative number of detections with a given SNR. Although many a large fraction of sources have SNRs around our assumed detection threshold of 7, many systems are detected with very high SNRs. We find that on average for a 4(10)-year LISA mission, of the 124(202) detections, 85(138), 16(27) and 9(14) systems have SNRs greater than 10, 50 and 100, respectively. These high SNR systems are typically, but not only, the more massive BHBH systems.

*Chirp mass*—The chirp mass is important for identifying the type of the source of a detected GW signal. The uncertainty of the chirp mass depends on the uncertainty in the measured orbital frequency, the time derivative of the orbital frequency and the eccentricity as detailed in Appendix C.

We find that for a 4(10)-year LISA mission, approximately 41(105) detections have measurable chirp masses ( $\Delta\mathcal{M}_c/\mathcal{M}_c < 1$ , indicated by the dark shaded region in Fig. 6) whilst 13(31) have chirp mass uncertainties below 10% ( $\Delta\mathcal{M}_c/\mathcal{M}_c < 0.1$ , indicated by the light shaded region in Fig. 6). This uncertainty is generally dominated by the uncertainty on the time derivative of the frequency, since most of the binaries are too early in their inspiral for LISA to measure a strong chirp. Note from Fig. 6 that increasing the mission length significantly increases the number of detections for which the chirp

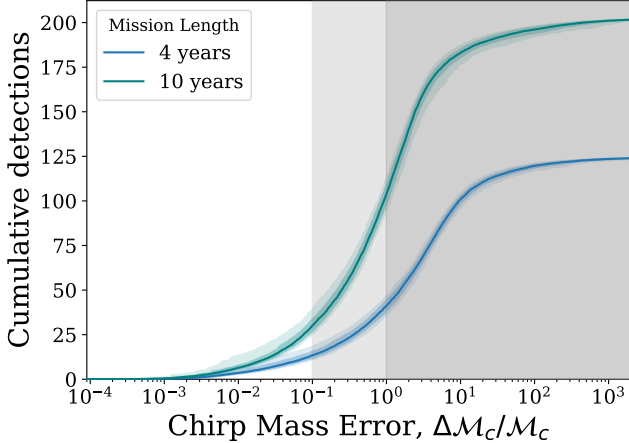


**Figure 6.** As Fig. 5, but for the chirp mass uncertainty. The shaded areas indicate regions with more than 10% and 100% uncertainty. .

mass uncertainty is below 100%. The total number of detections only scales as  $\sqrt{T_{\text{obs}}}$ , yet we find that the total number of detections with a chirp mass uncertainty is below 100% and 10% both scale approximately as  $T_{\text{obs}}$ .

*Sky localisation*—An accurate sky localisation will be essential to possibly identify electromagnetic counterparts or distinguish sources that come from different components of our Milky Way.

We quantify the sky localisation of a source by estimating the angular resolution for the detectable sources. Since all potential sources are effectively stationary on the timescale of the LISA mission, we can follow Mandel et al. (2018) and use the timing accuracy of LISA and the effective detector baseline to calculate the angular resolution,  $\sigma_\theta$ , as

$$\sigma_\theta = 16.6^\circ \left( \frac{7}{\rho} \right) \left( \frac{5 \times 10^{-4} \text{ Hz}}{f_{\text{dom}}} \right) \left( \frac{2 \text{ AU}}{L} \right), \quad (15)$$

where  $L$  is the effective detector baseline, which for LISA is 2 AU in the frame of the solar system, since it will orbit the Sun.

We plot the distribution of expected angular resolutions in Fig. 7. We see that, for a 4(10)-year LISA mission, approximately 82(123) sources can be resolved to an angular resolution better than 10 degrees and only 16(23) better than 1 degree.

For comparison, the size of a pencil beam for a 15 m diameter SKA dish observing at 1.4 GHz is roughly 0.67 square degrees (Smits et al. 2009), corresponding to an angular resolution of  $\sigma_\theta = \sqrt{(0.67/\pi)} = 0.46^\circ$  (similar to the angular size of the moon). We will further discuss the prospects of matching LISA detections to radio pulsars with SKA in Sec. 5.2.

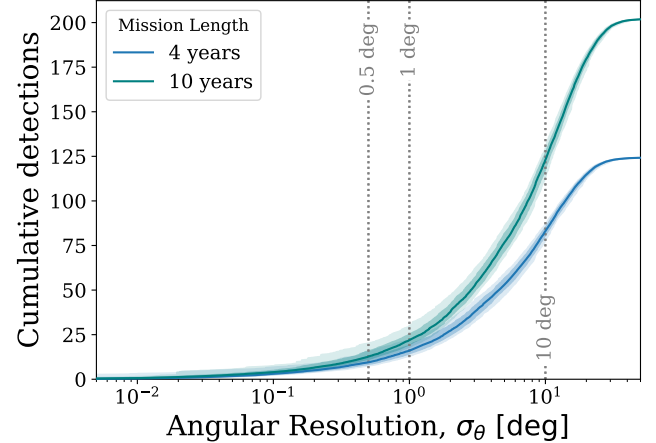


**Figure 7.** As Fig. 5, but for the angular resolution. .

#### 4. RESULTS II - IMPACT OF PHYSICS ASSUMPTIONS

In this section we explore the effect of varying the uncertain assumptions governing the evolution of binary system and the formation of compact objects. For this we use the population synthesis simulations and model variations presented in Broekgaarden et al. (2021a,b).

We first discuss the robustness of our predictions for the number of detectable systems (Section 4.1). We then discuss examples of how the observable properties of the detectable systems, such as the distribution of masses and eccentricities, are affected and can potentially be used to probe the physics of double compact object formation (Section 4.2).

##### 4.1. Detection rates

We predict approximately 30-370 detections in a 4-year LISA mission, across all our simulations for varying physics assumptions. This increases to about 50-550 for a 10-year LISA mission. Although the number of detections per type can vary by about 2 orders of magnitude, we find that the total detection rate is fairly robust, among the variations we have considered (see Table F1).

In Fig. 8, we show the expected number of LISA detections based on our simulations considering variations in the physical assumptions. We show the expected number of detections for BHBN, BHNS and NSNS systems in the top, middle and bottom panel respectively. All the rates and their uncertainties plotted in this figure are also provided in Table F1. In the sections that follow, we briefly explain the variations considered and discuss the most prominent trends.

###### 4.1.1. Efficiency of mass transfer

The efficiency of mass transfer, i.e. the fraction of mass lost by the donor through Roche-lobe overflow that is accreted by the companion, is poorly constrained and is considered as one of the main uncertainties in binary evolution (e.g. de Mink et al. 2007). In our fiducial model A, we use a prescription in which the accretion rate onto stellar companions is regulated by their thermal timescale, i.e. the timescale on which a star can react to changes and restore thermal equilibrium (see e.g. Schneider et al. 2015).

In models B-D, we instead adopt a fixed value for the mass transfer efficiency,  $\beta$ , from  $\beta = 0.25$  up to 0.75, in cases of stable mass transfer onto a stellar companion. For accretion onto NS and BH we still assume that their accretion is limited to the Eddington rate.

Since nearly all systems that can be detected form channels where the very first interaction is stable mass transfer, changing  $\beta$  can affect the majority of systems. Generally, higher mass transfer efficiencies lead to higher masses for the accreting stars, but also lead to wider orbits (Soberman et al. 1997; van Son et al. 2020). Changing  $\beta$  thus already affects the masses and orbital separation after the first interaction phase, which in turn changes the starting conditions and outcome of all subsequent interactions phases. This makes it complicated to fully understand the impact of varying  $\beta$  in simple terms, but we can distinguish two main patterns for higher and lower mass systems respectively.

For the most massive progenitors, increasing  $\beta$  leads to secondary stars that are so massive and luminous that they experience strong wind mass loss. This leads to further widening of the orbit. In addition the more massive secondaries may not be able to fully expand as mass loss may prematurely remove their hydrogen envelope. Both of these effects tend to prevent the most massive secondaries from filling their Roche lobe. This means that they cannot initiate the reverse interaction needed to shrink the binary system and eventually produce a detectable double compact object. We indeed see that increasing  $\beta$  leads to a decrease of the expected number of detections for BHBs and BHNSs, which originate from the most massive progenitors.

For lower mass progenitors, which primarily produce NSNS systems, we find the opposite: increasing  $\beta$  leads to an *increase* in the number of detectable NSNS systems. This is in part because the changes in secondary mass and the orbital widening, affect the number of systems for which the reverse interaction successfully ejects the envelope and shrinks the orbit. Furthermore, the increased mass of the secondary stars allows stars that would have otherwise ended their life as a WD to instead become massive enough to form a NS (e.g. Za-

partas et al. 2017). The same effect also allows some NS progenitors to become massive enough to become BH progenitors, which partially cancels the extra progenitors that would have originally been destined to become WDs.

#### 4.1.2. Common-envelope evolution

The common-envelope phase constitutes a highly uncertain phase in the evolution of interacting binary systems (e.g. Ivanova et al. 2013). The uncertainties concern the conditions required for the onset of a common-envelope phase and, if a common-envelope phase occurs, what the outcome is. Rapid population synthesis simulations such as ours approximate both questions in a crude way. We therefore consider several model variations.

*The efficiency parameter  $\alpha_{\text{CE}}$* —To estimate the outcome of a CE phase, we use a simple consideration of the binding energy and orbital energy (Webbink 1984; de Kool 1990). Our fiducial model assumes a common-envelope efficiency parameter  $\alpha_{\text{CE}} = 1$  which can be interpreted as the case where all the energy liberated by shrinking the orbit is used in an optimal way to unbind the envelope. There have been many attempts to constrain this parameter using observations and more recently also using 3D simulations (e.g. De Marco et al. 2011; Law-Smith et al. 2020; Lau et al. 2021), but no consistent picture has emerged. Therefore we consider large variations in this parameter.

In models G-J we alter the common-envelope efficiency parameter  $\alpha_{\text{CE}}$  to 0.1, 0.5, 2.0 and 10.0 respectively. Values smaller than 1 may represent cases where not all energy is used efficiently to unbind the envelope, for example when part of the energy escapes in the form of radiation or if part is used to impart additional kinetic energy in the ejecta (e.g. Ivanova et al. 2013; Nandez & Ivanova 2016). Values larger than 1 may represent cases where additional energy sources can be tapped into, such as for example jets powered by accretion (e.g. Schreier et al. 2021). The variations can also be seen as a way to cover uncertainties in estimates for the binding energy itself.

Increasing  $\alpha_{\text{CE}}$  makes common-envelope ejection more efficient or, in other words, less orbital shrinkage is needed to successfully eject the envelope. This has two consequences. (1) A larger fraction of systems avoids merging during the CE phase. This increases the overall number of DCOs. (2) The systems that survive the CE phase are wider, possibly too wide to become detectable as gravitational wave sources (e.g. Klencki et al. 2021). So, while the first consequence favours the formation of

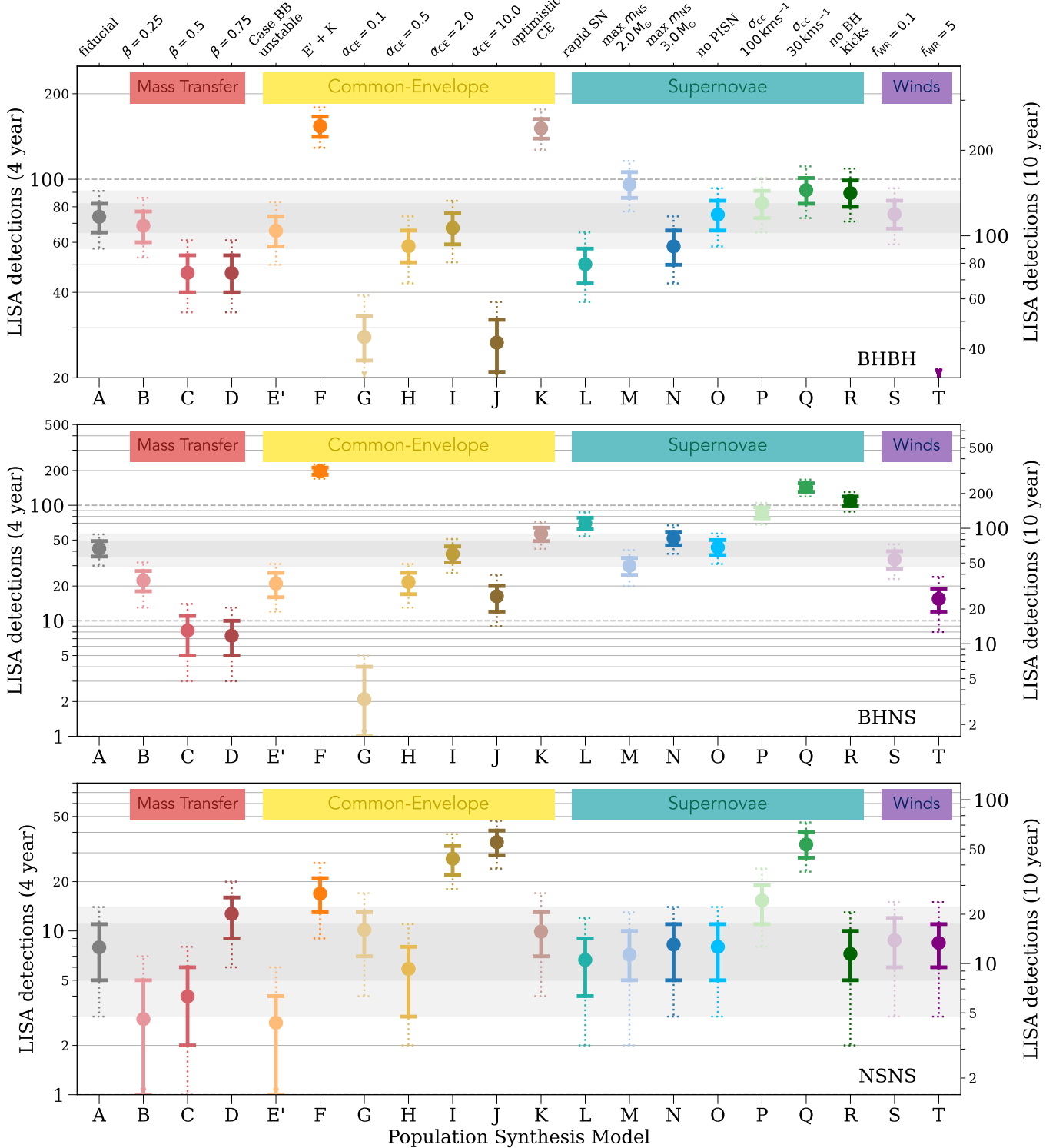


**Figure 8.** The number of expected detections in the LISA mission for different DCO types and model variations. Error bars show the 1- (solid) and 2- $\sigma$  (dotted) Poisson uncertainties. An arrow indicates that the error bar extends to zero. The left axis and grid lines show the number of detections in a 4-year LISA mission and the right axis shows an approximation of the number of detections in a 10-year mission (we scale the axis by  $\sqrt{T_{\text{obs}}}$ , see Table F1 for exact rates). **The grey shaded regions indicate the 1- and 2- $\sigma$  region for the fiducial model.** Each model is described in further detail in Table A1 and details of the fiducial assumptions are in Section A.2. See Sec. 4.1 for a discussion.

1137 DCOs, the second consequence disfavours the formation  
 1138 of DCOs that are tight enough to be detected.

1139 These two opposing effect result in a fine tuning sit-  
 1140 uation. Only a very small subset of progenitor systems  
 1141 have the right orbital parameters prior to the CE phase  
 1142 to successfully produce detectable systems. Changing  
 1143  $\alpha_{CE}$  moves and changes this window in the parameter  
 1144 space that successfully leads to the formation of de-  
 1145 tectable systems. How the number of the detectable  
 1146 systems changes depends on whether the relevant pa-  
 1147 rameter space grows or shrinks and on how well the rel-  
 1148 evant part of the parameters space is populated. Fully  
 1149 unravelling these effects and how they interplay with  
 1150 the assumed star formation history is beyond our scope  
 1151 (and possibly not even of large relevance given the severe  
 1152 simplifications). We will limit the further discussions to  
 1153 simply stating the trends we observe.

1154 We find that the BHBH rate peaks for  $\alpha_{CE} = 1$  (model  
 1155 A) and reduces whether we increase *or* decrease  $\alpha_{CE}$ .  
 1156 The BHNS rate follows the same pattern as BHBHs al-  
 1157 though the value of  $\alpha_{CE}$  which maximises BHNSs seems  
 1158 to be between 1 and 2. In contrast, for NSNSs we find  
 1159 that increasing  $\alpha_{CE}$  (models I and J) results in signifi-  
 1160 cantly higher rates.

1161 *The “optimistic” CE treatment*—We further explore a  
 1162 model variation introduced by Belczynski et al. (2007)  
 1163 often referred to as the “optimistic” CE scenario.  
 1164 This variation (model K) relaxes our restriction that  
 1165 donor stars that are on the Hertzsprung cannot survive  
 1166 common-envelope events.

1167 In agreement with other studies, we find that this  
 1168 treatment leads to a significant increase in the formation  
 1169 rate of BHBHs, by a factor of two. This is because the  
 1170 progenitors expand significantly during the Hertzsprung  
 1171 gap phase in our simulations. In our fiducial simulation,  
 1172 all progenitors that initiate unstable interaction during  
 1173 this phase would end as stellar mergers, while in this  
 1174 variation they will survive. The progenitors of BHNSs  
 1175 and NSNSs are less strongly affected with an increase  
 1176 about 30% increase.

1177 *Case BB mass transfer*—In models E' and F we consider  
 1178 uncertainties in case BB mass transfer. This is a phase  
 1179 of mass transfer where the donor star has already lost  
 1180 its hydrogen envelope in a prior interaction, but fills  
 1181 its Roche lobe again as it expands during helium shell  
 1182 burning phase (e.g. Dewi et al. 2002; Tauris et al. 2015,  
 1183 2017). This is of particular interest for the formation  
 1184 of NSs, as their lower mass progenitors are swelling the  
 1185 most during this phase (e.g. Laplace et al. 2020, and  
 1186 references therein). Population synthesis studies find

1187 that nearly all NSNS systems form through a phase of  
 1188 case BB mass transfer (Vigna-Gómez et al. 2018).

1189 In model E' we enforce that case BB mass transfer is  
 1190 always unstable, such that it always leads to a CE. Note  
 1191 that this is slightly different from model E described in  
 1192 Broekgaarden et al. (2021a,b). In their work the pes-  
 1193 simistic approach to CE evolution is implemented such  
 1194 that all HG stars are excluded including helium stars in  
 1195 the helium shell burning phase. This, in combination  
 1196 with the assumption that case BB mass transfer is al-  
 1197 ways unstable, effectively leads to the exclusion of all  
 1198 systems that originate through this channel. We are in-  
 1199 terested in NSNS systems, which are frequently formed  
 1200 through this channel in our simulations. Therefore, we  
 1201 adapted this model to only exclude H-rich HG donors,  
 1202 but allow systems with donors that are helium stars in  
 1203 the helium shell burning phase to survive a CE phase.

1204 As expected, in model E', we find that case BB sys-  
 1205 tems form through a common-envelope phase rather  
 1206 than only stable mass transfer (see Fig. F1). This model  
 1207 gives the lowest NSNS rate of all of our variations, which  
 1208 is a factor of 3 lower than our fiducial rate. We also  
 1209 find a reduction of the BHNS systems by a factor 2.  
 1210 The BHBH systems are not significantly affected, as ex-  
 1211 pected, since case BB mass transfer does not play a role  
 1212 for high mass progenitors.

1213 Finally, in model F, we again enforce that case BB  
 1214 mass transfer is always unstable, but in combination  
 1215 with the optimistic treatment for CE (essentially com-  
 1216 bining models E' and K). This allows the systems that  
 1217 have HG donors for common-envelopes (as well as those  
 1218 formed through case BB mass transfer) to survive the  
 1219 CE phase. We find that this model leads to the highest  
 1220 predictions for the detections among all variations that  
 1221 we have considered.

#### 1222 4.1.3. Supernovae and compact remnants

1223 The formation of compact remnants and their associ-  
 1224 ated natal kicks also constitute important uncertainties.

1225 In model L we consider the so-called “rapid” remnant  
 1226 mass function by Fryer et al. (2015) as an alternative  
 1227 to the “delayed” description used in our fiducial simula-  
 1228 tions. This affects the mass distribution (see Sec. 4.2.1),  
 1229 but the effects on the number of detectable systems is  
 1230 modest for BHBH and BHNS, and negligible for NSNS.

1231 The same is true for the impact of changing the as-  
 1232 sumed maximum neutron star mass,  $m_{NS,max}$  ( $M$  and  
 1233  $N$ ). Lowering  $m_{NS,max}$  increases the number of detec-  
 1234 tions involving BHs (since more stars form BHs instead  
 1235 of NSs) and vice versa, but has no significant effect on  
 1236 the number of NSNS detections since the vast majority  
 1237 are formed from low mass NSs.

We find that not implementing pair-instability supernovae (PISN) or pulsational pair-instability supernovae (PPISN) in model O has no effect on the number of detections with LISA. This is because the average metallicity of the Milky Way is high enough such that no progenitor retains enough mass to initiate a PISN or PPISN.

Decreasing the natal kicks for all core-collapse supernovae (models P-Q) increases the detection rates for each DCO type, since lower kicks result in fewer disrupted binaries and hence a more numerous detectable population. The BHNS and NSNS systems are strongly affected whilst the impact on BHBH systems is insignificant. The reason that BHBHs are relatively unaffected is that, in our models, the natal kicks for BHs are scaled down with the amount of mass that falls back. In the case of BHBHs, the black holes have very massive cores and thus low kicks.

In model R we assume BHs form without any kick, while using our fiducial assumption for the natal kicks of neutron stars. This increases the predictions for BHNS by a factor 3 but the impact on BHBH systems is much smaller for the same reason as for models P-Q. As expected, the NSNS population is not affected.

#### 4.1.4. Stellar winds

Mass loss in the form of stellar winds or eruptions is also a main uncertainty. It affects by how much stars can grow in size and it affects the final core masses. We consider variations in the mass loss by naked helium (Wolf-Rayet like) stars and choose to vary the efficiency of these winds between 0.1 and 5, to account for uncertainties in the derived rates (e.g. Vink 2017; Shenar et al. 2019; Hamann et al. 2019; Sander & Vink 2020).

We find that a reduction of the wind mass loss has very little effect on our predictions. This is the consequence of several effects that cancel each other. Firstly, the decreased Wolf-Rayet like winds mean that the DCOs (particularly those containing BHs) are generally more massive and so more detectable in LISA. Secondly, one may expect that LISA sources in model S would be higher frequency than in our fiducial model as decreased winds generally result in tighter binaries. However, though this is the case at DCO formation, we find that by the time the sources have evolved until they are observable by the LISA mission, they have lower orbital frequencies than in our fiducial model. This is because the reduced winds allow DCOs to be formed at higher metallicity and, therefore, at more recent times. This means that most DCOs do not evolve for as long before the LISA mission and so remain at lower frequencies (wider separations) thus making them less detectable.

In addition, we find that NSNSs are more eccentric and BHBHs are less eccentric than our fiducial model (with BHNSs relatively unchanged). The increase in eccentricity for NSNSs comes from the same reason as the lower frequency, more recent birth times mean that binaries have less time to circularise. The same is not true for BHBHs as the more massive systems are less affected by supernova kicks and so fewer high eccentricity systems are formed. Overall, despite the large differences in the system properties, these three effects in combination leave the detection rates relatively unchanged.

In model T we instead *increase* the efficiency of Wolf-Rayet winds by a factor of 5. In this model the detection rate of BHBHs decreases by over a factor of 10 and BHNSs by over a factor of 2 whilst the NSNS rate is relatively unchanged. Increasing the efficiency of WR winds widens the orbit and decreases the final masses of DCOs. This means that some progenitors that would have formed LISA sources under our fiducial assumptions would not have enough mass to produce a DCO, or produce a NS instead of a BH. The effect is strongest for the progenitors of black holes, since these are most strongly affected by Wolf-Rayet winds. This effect is less pronounced in NSs since the rate of mass loss for the progenitors of these systems is low enough that changing by a factor of 5 still does not impact the final fate. Moreover, DCOs that are formed tend to be less massive and therefore less detectable.

### 4.2. Properties of detectable systems

In this section, we consider how varying underlying physics assumptions changes the properties of detectable systems. We focus on several key differences across physics variations rather than showing the differences in every model and thus this section is by no means exhaustive.

#### 4.2.1. Effect of remnant mass prescription on lower mass gap

In Fig. 9, we show the component mass distribution for all LISA detectable DCOs (BHBHs, BHNSs and NSNSs) for two different remnant mass prescriptions. The grey distribution uses the Fryer *delayed* remnant mass prescription (Fryer et al. 2012), which is our fiducial assumption (model A). This prescription produces compact objects in the lower mass gap ( $2.5 M_{\odot} \leq m \leq 5 M_{\odot}$ ) and indeed we find that, of the LISA detectable DCOs, approximately 69% of BHBHs, 39% of BHNSs and 0% of NSNSs have at least one component in the lower mass gap. Overall, weighting by the relative detection rates, this gives that, in our fiducial model, 55% of our predicted LISA DCO detections would have at least one component in the lower mass

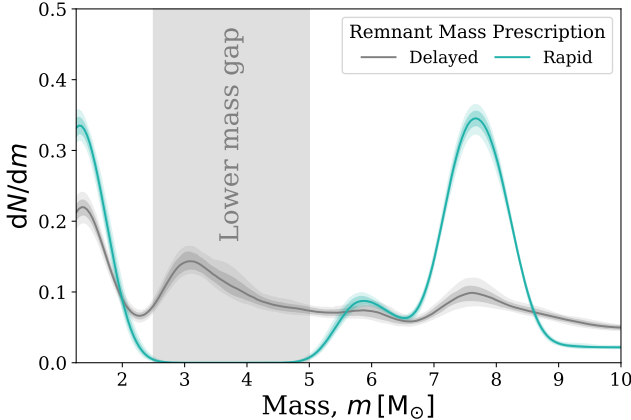


**Figure 9.** Comparison of the component mass distribution of LISA detectable DCOs when using the Fryer delayed (model A) and rapid (model L) remnant mass prescriptions. Distributions are plotted in the same way as Fig. 3, except all DCOs types are shown in one curve and each type is weighted by its detection rate in the respective model.

gap when using this remnant mass prescription. This equates to approximately 69 systems being detected in the lower mass gap. Alternatively, the blue curve in Fig. 9 shows the same distribution but for the *rapid* remnant mass prescription (Fryer et al. 2012), which we use in model L. In this case, no compact objects are formed (and therefore, detected) in the lower mass gap.

From the stark difference between these models, it is clear that it is difficult at this point to say with any certainty what fraction of systems LISA will detect in the lower mass gap given the highly uncertain formation rate of systems in this mass range.

We find that the percentage of detectable systems with at least one component in the lower mass gap varies between approximately 30-70% (or, in terms of detections, from 15 to 156) for the different model variations that we consider, except for model L, for which it is 0%. **We note however that the masses of detectable systems are not always well constrained (see Section 3.5). It may therefore be difficult to assess whether a detected system truly has components in the mass gap.**

Lastly, we highlight that recent investigations of the GW detections so far suggest a significant reduction of BHs in the lower mass gap (e.g. Farah et al. 2021; Ye & Fishbach 2022, van Son et al. in prep.). All our models except model L allow for systems in the mass gap, which may be at tension with the observational constraints so far.

#### 4.2.2. Effect of natal kicks on eccentricity distribution

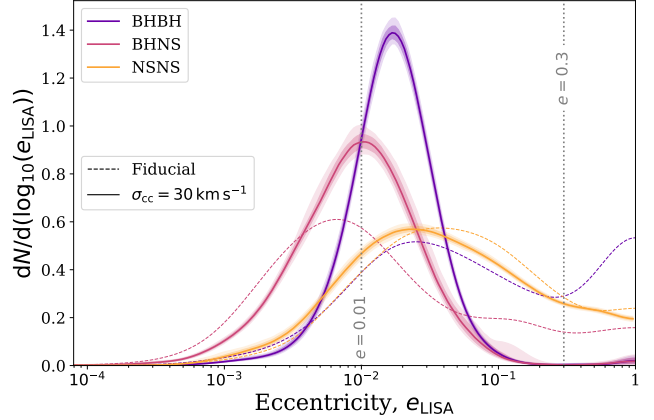


**Figure 10.** As Fig. 3d, but for model Q. For comparison, we show the mean distribution for the fiducial model (model A) as dashed lines.

In Fig. 10, we investigate how decreasing the magnitude of natal kicks from core-collapse supernovae affects the eccentricity distribution of LISA detectable DCOs. For reference, we show the mean fiducial distributions (model A) as dashed lines (see Fig. 3d for full comparison). In the main curves, we reduce the velocity dispersion for core-collapse supernovae from  $265 \text{ km s}^{-1}$  to  $30 \text{ km s}^{-1}$  (model Q).

We find that the LISA detectable BHBHs are significantly less eccentric with weaker kicks, such that the population above  $e = 0.2$  is nearly completely eliminated. This is because BHBHs are often massive enough to withstand strong natal kicks without disrupting and these kicks tend to impart significant eccentricity. In model Q, very few systems are ever given such strong kicks and thus very few BHBHs are detected with significant eccentricity.

Since BHNSs are less massive than BHBHs and have more unequal mass ratios, they are more vulnerable to disruption during supernova kicks. BHNSs can only withstand strong kicks when they are aimed in the correct direction and so only a small ‘lucky’ fraction of the fiducial population is highly eccentric. Therefore in model Q, although we see that the population of highly eccentric BHNS systems is eliminated (similar to BHBHs), the peak of the distribution actually shifts to *higher* eccentricity. This is because a larger fraction of systems are given weaker kicks that BHNSs can withstand and these impart much more moderate eccentricities.

Finally, we find that the NSNS distribution is relatively unchanged between model A and Q. This is not surprising however since the majority of NSNSs are formed through electron-capture supernovae and ultra-stripped supernovae and for these types of supernovae

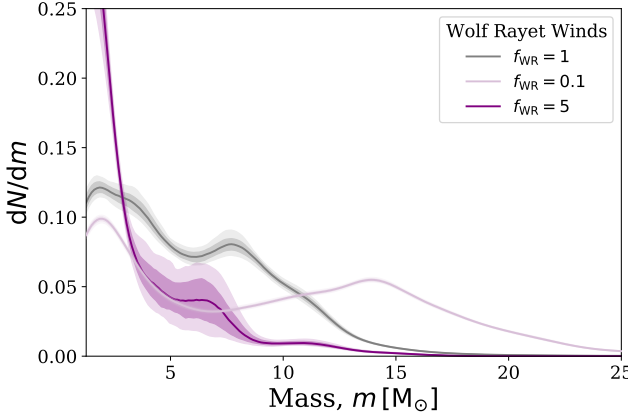


**Figure 11.** As Fig. 9, but instead varying Wolf-Rayet wind efficiency (models S and T). The curve for  $f_{WR} = 5$  has much higher uncertainties as there are many fewer DCO systems formed in this model (the inverse reasoning also explains the lower uncertainties for  $f_{WR} = 0.1$ ).

we use  $\sigma_{\text{rms}}^{1D} = 30 \text{ km s}^{-1}$  already (see App. A.2) and thus there is little difference between the models.

Overall, compared to our fiducial model, we find that decreasing supernova natal kicks, though it strongly increases the number of detections (see Fig. 8), strongly decreases the fraction of highly eccentric systems that are detected.

#### 4.2.3. Effect of Wolf-Rayet winds on mass distribution

In Fig. 11 we show the effect that changing the efficiency of Wolf-Rayet winds has on the individual component mass distribution. Decreasing the Wolf-Rayet wind efficiency allows the formation of more massive DCOs in the Milky Way and, indeed, we see that the distribution extends to  $25 M_\odot$  and relatively fewer detectable systems are formed at low masses. By contrast, increasing the Wolf-Rayet efficiency by a factor of 5 strongly disfavours the formation of systems at high masses and approximately 85% of detectable systems have masses below  $5 M_\odot$ . These three distributions are very distinct and so it is possible that the mass distribution of LISA could help to constrain the efficiency of Wolf-Rayet winds.

## 5. DISCUSSION

In this section we discuss the prospects of (and methods for) identifying LISA sources (Sec. 5.1), the possibility of matching LISA signals to SKA detections (Sec. 5.2), the main caveats for this study (Sec. 5.3) and the possible contribution from other formation channels (Sec. 5.4). All predictions quoted in each subsection are derived for the fiducial model (model A).

### 5.1. Identification of GW sources

It is important to note that, though we present predictions for the detection rates of specific DCO types, the nature of the source may not be immediately (**or ever**) apparent from the gravitational wave signal. LISA can detect a variety of sources, from exoplanets (e.g. Tamanini & Danielski 2019) to common-envelopes (e.g. Ginat et al. 2020; Renzo et al. 2021) that may cause confusion. However, by far the most prominent will be the population of Galactic WDWDs detectable with LISA, which will be several orders of magnitude larger than the population of the more massive DCOs that we focus on in this paper (e.g. Korol et al. 2017). It is therefore imperative that we consider how to distinguish NS and BH binaries from this much more numerous population of sources. In addition to distinguishing them from WDWDs, we must consider how to discriminate between BHBHs, BHNSs and NSNSs themselves.

#### 5.1.1. Distinguishing from WDWD population

The simplest way to check whether a source is a WDWD is to evaluate its chirp mass. The mass of a non-rotating white dwarf cannot be larger than the Chandrasekhar limit of  $1.4 M_\odot$  (Chandrasekhar 1931; Hamada & Salpeter 1961), so we can take the maximum chirp mass of a WDWD to be  $\sim 1.2 M_\odot$ . Therefore, any DCO with a chirp mass that satisfies  $\mathcal{M}_c > 1.2 M_\odot + \Delta \mathcal{M}_c$  must not be a WDWD (where  $\Delta \mathcal{M}_c$  is the error on the chirp mass, estimated using Eq. C3). We find that for the detectable population of a 4(10)-year LISA mission, 24(38)% of BHBHs, 28(41)% of BHNSs and 4(5)% of NSNSs satisfy this condition. This method is not particularly effective for NSNSs since their average chirp mass,  $1.17 M_\odot$ , is below the Chandrasekhar limit.

Another discriminator between WDWDs and other DCOs is eccentricity. WDWDs formed in the disc are thought to be formed mainly through isolated binary formation and have little to no eccentricity (e.g. Nelemans et al. 2001, see however Dosopoulou & Kalogera 2016a,b; Gosnell et al. 2019). This is because WD-WDs formed through isolated binary evolution all experience a phase of mass transfer or a common envelope, which typically circularises the binary (e.g. Marsh et al. 2004). However, in contrast to the more massive DCOs that we study, WDWDs do not experience strong natal kicks which we find to be the main source of eccentricity. Therefore, if any system is detected with anything other than one detectable harmonic, this suggests that the system is unlikely to be a WDWD. We find that for a 4(10)-year LISA mission, 55(61)% of BHBHs, 27(29)% of BHNSs and 66(68)% of NSNSs are detected with multiple harmonics (see also Sec. 3.2). Both the

absolute percentage and the relative improvement with an extended LISA mission is lower for the BHNSs with respect to other DCOs as we find that these BHNSs are less eccentric on average (see Fig. 3d and discussion in Sec. 3.2).

However, we should also consider that eccentric WD-WDs could be formed through dynamical formation in Milky Way globular clusters (e.g. Willems et al. 2007; Kremer et al. 2018), or with third companions (e.g. Antonini et al. 2017). This means that we cannot assume that eccentric binaries are not WDWDs unless they are detected in the Galactic plane (though even then there is a chance they were formed dynamically). We can use the sky localisation, scale height of the disc and distance to the source to estimate what fraction of eccentric sources can be localised to the Galactic plane. This condition can be written as  $\sigma_\theta < \arcsin(z_{\text{plane}}/D_L)$  or  $D_L < z_{\text{plane}}$ , where we set the height of the Galactic plane,  $z_{\text{plane}} = 0.95$  kpc, to the scale height of the high- $\alpha$  disc. We apply this condition to find that the fraction of sources that are eccentric and localised within the disc for a 4(10)-year LISA mission are 40(40)% for BHBHs, 23(23)% for BHNSs and 59(59)% for NSNSs. Note that although the fractions are the same for the 10-year mission, the absolute number of detections is still greater.

Overall, combining these methods (chirp mass, eccentricity and sky localisation) we find that for a 4(10)-year mission, LISA will detect at least 37(70) BHBHs, 18(38) BHNSs and 5(8) NSNSs that are distinguishable from the WDWD population. Thus we will be able to confidently distinguish approximately half of all detected sources from WDWDs. This increases to roughly 60% for a 10-year mission. We highlight that, though the overall number of LISA detections in an extended mission only increases by a factor of  $\sqrt{T_{\text{obs}}}$ , the number of distinguishable detections increases by a greater factor since each of the more numerous sources are better measured. This further underlines the benefits of extending the LISA mission to 10 years.

### 5.1.2. Discriminating between BHBHs, BHNSs and NSNSs

The problem of discriminating between the BHBH, BHNS and NSNS populations can be more difficult than distinguishing them from WDWDs. For NSNSs, we can follow a similar method to the WDWDs (see Sec. 5.1.1) by applying our knowledge of the maximum mass of a neutron star. Following our fiducial assumption, we can take the maximum mass of a neutron star as  $2.5 M_\odot$  and thus the maximum chirp mass that a system can attain without one of the components being a black hole is  $\mathcal{M}_c = 2.2 M_\odot$ . For a 4(10)-year LISA mission, the fraction of systems that are above or below this limit

(and thus *must* respectively contain or not contain a BH component) by more than  $\Delta\mathcal{M}_c$  is 21(33)% for BHBHs, 18(24)% for BHNSs and 47(62)% of NSNSs, which in terms of absolute detections is 16(39) for BHBHs, 7(17) for BHNSs and 4(8) for NSNSs.

For separating the BHBH and BHNS population one could do so probabilistically given the properties that are measured, particularly the orbital frequency and eccentricity, since these distributions are fairly different for the two DCO types (see Fig. 3). This method would pose a challenge, however, as it would likely only indicate which type was more likely rather than discriminate between them with strong evidence.

Another possible solution would be the existence of electromagnetic counterparts to the gravitational wave signal. In Section 5.2 we consider the possibility of detecting a pulsar within a BHNS or NSNS system. This could be used to identify the type of the source.

### 5.2. Matching LISA detections to pulsars with the SKA

Since the vast majority of the LISA detectable population of DCOs will not merge for many years, the main type of electromagnetic counterpart for this population is pulsars. Therefore, for this section we focus only on BHNSs and NSNSs since no BHBH system will contain a pulsar. The joint detection of a binary pulsar with LISA and the Square Kilometre Array (SKA, Dewdney et al. 2009) would not only help to constrain the parameters of the binary, but also enable investigation of other compact object physics. A pulsar(PSR)+BH can provide stringent tests of theories of gravity, in particular the “No-hair theorem” (Keane et al. 2015). Alternatively, an ultrarelativistic PSR+NS system could be used to measure the neutron star equation of state up to an order of magnitude more accurately than other proposed observational constraints (Kyutoku et al. 2019; Thrane et al. 2020).

We estimate that on average, given the number of detectable pulsars and the SKA sky area, each pulsar in the SKA occupies a region with an angular resolution of  $\sigma_\theta < 1.3^\circ$  or  $0.7^\circ$  for SKA-1 and SKA-2 respectively (see Appendix E). Therefore, any DCOs containing NSs localised by LISA with an angular resolution lower than these values can be unambiguously matched to the radio signal in the SKA. By considering Fig. 7, approximately 11 and 6 (for SKA-1 and SKA-2) DCOs will satisfy this constraint.

If there is more than one pulsar in the region given by the LISA sky localisation, one can compare the measured parameters of the system in LISA and the SKA. Both the SKA and LISA will measure the orbital frequency to high precision, as well as the time derivative

of the frequency and chirp mass to a lesser precision, of each of these systems. Therefore, one could perform a targeted search with the SKA that checks the sky location given by LISA, only looking for binary pulsars with orbital frequencies within the uncertainties. If there was still more than one possible pulsar one could also check against the chirp mass. In this way, we expect it will be possible to get a joint detection between the SKA and LISA even when the sky area implied by the LISA detection contains more than one pulsar.

In order to assess the efficacy of this method, we would need to know the probability that two random binary pulsars would have orbital frequencies and chirp masses close enough that one could not tell which pulsar matches the LISA detection. This would require simulating the SKA population of pulsars with a code such as PSRPOPpy (Bates et al. 2014) to find the frequency and chirp mass distribution, which is beyond the scope of this paper. However, the uncertainty in the orbital frequency of a binary on the detection threshold ( $\text{SNR} = 7$ ) for a 4-year LISA mission is  $2.5 \times 10^{-9}$  Hz and  $1.0 \times 10^{-9}$  Hz for a 10-year mission (calculated using Eq. C4). Therefore, we expect that the SKA could likely isolate the correct binary pulsar to match to a LISA detection even when several are present in the sky localisation region.

### 5.3. Caveats

Our predictions are subject to various uncertainties which can be broadly divided into two different categories: those arising from the progenitor models for the population of DCOs and those arising from the choices we have made when placing these DCOs in our model for the Milky-Way. Although we are unable, at present, to evaluate the impact of all these uncertainties, the reader should nevertheless keep in mind that they are likely very substantial. Most of these concerns are not unique to these study, but apply to most of the predictions available in present literature. We highlight a few main concerns.

*Progenitor models*—Our binary-star progenitors models have been computed with a rapid population synthesis code (see Sec. 2.1). This code relies on approximate parametric prescriptions for the stellar evolutionary tracks of single tracks and simple algorithms to mimic the effects of evolutionary and binary interaction processes. Even though we explicitly consider the impact of some of the main physics uncertainties (see Sect. A.3) the list of variations that we considered is far from exhaustive. Moreover, it is by no means guaranteed that the parametric prescriptions used in this code lead to realistic results, even when varying the values of the

parameters to their extremes. We stress in particular the uncertainties affecting our most massive progenitor models. Observational constraints are scarce for high mass stars and practically non-existent for the rapid evolutionary phases (e.g. Langer 2012; Mapelli 2021). This is even more true for the evolution of massive stars at low metallicity. In addition to our limited understanding of massive stars, we note that the rapid population synthesis code, such as the one employed to compute the models used in this study, rely on extrapolations of the original fitting formulae to approximate the evolutionary tracks for these higher mass progenitors (Hurley et al. 2000, 2002). A further caveat is whether the population synthesis predictions used in our study realistically describe the population of compact objects. Broekgaarden et al. (2021b) shows that none of the physics variations that we use can be excluded at present based on the overall constraints on the GW rates, but this does not mean that they are accurate. For example, at present it is unclear whether these models reproduce the features in the inferred mass distribution (van Son et al. in prep. Farah et al. 2021; The LIGO Scientific Collaboration et al. 2021b; Li et al. 2021; Veske et al. 2021; Tiwari 2022; Edelman et al. 2022).

*Populating the Milky Way*—Our Milky Way model is semi-empirical and has been calibrated based on observations. Unfortunately, the early evolution of the (metallicity dependence of the) star formation history is poorly constrained. We do not expect this to be a major concern, as most of the double compact objects have relatively short delay times of less than 2 Gyr (see Fig. 3e), but this is a caveat that should be kept in mind. Furthermore, to estimate the rate of detectable systems, we rely on normalisation choices (e.g. how many detectable double compacts are formed per unit of star formation). This depends heavily on the initial mass function, as low mass stars account for most of the mass while high mass stars are the progenitors of double compact objects. Further choices, such as the binary fraction and the initial distributions of binary parameters also play a lesser but probably still significant role de Mink & Belczynski (e.g. 2015); Chruslinska et al. (e.g. 2017); Klencki et al. (e.g. 2018).

We also note that, for reasons of computational efficiency, we have not accounted for the spatial velocities resulting from the Blaauw-Boersma kick (Blaauw 1961; Boersma 1961). In test simulations we find that accounting for this spreads out the population (increasing the typical height above the Galactic plane and Galactocentric radius), but we find that the impact on the rate is

1693 limited. In light of the other much larger uncertainties,  
 1694 we felt that this was justified (see however, e.g., Brandt  
 1695 & Podsiadlowski 1995; Abbott et al. 2017b). **We have**  
 1696 **further ignored a possible contribution coming**  
 1697 **from the Galactic halo, as Sesana et al. (2020)**  
 1698 **estimates this is not significant compared to the**  
 1699 **contributions from the Galactic bulge and discs.**

1700 However, this may not be true for other formation chan-  
 1701 nels other than those we have considered here.

#### 1702 5.4. Other formation channels

1703 In this paper we considered the formation of NS  
 1704 and BH binaries formed via isolated binary evolution,  
 1705 through the classical CE channel, the stable mass trans-  
 1706 fer channel and variations on these (see Fig. F1). We did  
 1707 not consider further possible contributions from other  
 1708 formation channels, which may play a role.

1709 We highlight the possible role of dynamical formation  
 1710 in globular clusters. Kremer et al. (2018) predict, for a  
 1711 nominal 4-year LISA mission, that 21 sources will have  
 1712 SNR  $> 7$ , of which 7 are BHBHs, 0 are BHNSs and 1  
 1713 is a NSNS (see Table 1 Kremer et al. 2018). This is  
 1714 significantly lower than the rates we predict for nearly  
 1715 every model variation. If true, this would mean that for-  
 1716 mation through isolated binary formation will dominate  
 1717 the LISA detections.

1718 Banerjee (2020) investigates formation of LISA de-  
 1719 tectable BHBHs in young massive and open stellar clus-  
 1720 ters and estimates approximately 128 BHBHs with SNR  
 1721  $> 5$  in a 5-year LISA mission (see Table 1, Column 9  
 1722 Banerjee 2020). Although this is similar to the number  
 1723 we predict for our fiducial model, we note these authors  
 1724 adopt a threshold SNR required for a detection that is  
 1725 lower and a mission length is slightly longer than what  
 1726 is typically assumed (i.e. SNR  $> 7$  and 4 years, as we  
 1727 have also adopted in our work). We expect that, after  
 1728 correcting for this and making a fair comparison, our  
 1729 fiducial model predicts about twice as many detections.

1730 The contribution of triples systems (e.g. Antonini  
 1731 et al. 2017), or even higher order multiple systems (e.g.  
 1732 Vynatheya & Hamers 2021) will likely also be of inter-  
 1733 est, in particular for the formation of eccentric sources.  
 1734 We are, however, not aware of specific predictions for  
 1735 the detection rates that we can compare to directly.

## 1736 6. COMPARISON WITH PREVIOUS STUDIES

1737 In Fig. 12, we compare our results to similar previous  
 1738 studies that investigate the population of stellar-mass  
 1739 BHBHs, BHNSs and NSNSs that are detectable with  
 1740 LISA. Fig. 12 details the expected detection rates pre-  
 1741 dicted by each paper as well as their assumptions regard-  
 1742 ing their Milky Way galaxy model, binary population

1743 synthesis simulation and LISA mission specifications.  
 1744 We only include papers that are similar to our work,  
 1745 such that they use population synthesis and simulate  
 1746 sources in the Galactic plane. Moreover, Fig. 12 does  
 1747 not include the numerous papers on the LISA WDWD  
 1748 population as we do not make predictions for WDWDs.

1749 *Nelemans et al. (2001)*—were the first to investigate the  
 1750 population of LISA detectable stellar-mass double com-  
 1751 pact objects. We find a significantly higher detection  
 1752 rate for BHBHs and BHNSs, as well as a slightly lower  
 1753 rate for NSNSs. We can understand this difference from  
 1754 changes both to the specifications of LISA (such as the  
 1755 mission length and SNR threshold for detection) and our  
 1756 understanding of massive star evolution since the pub-  
 1757 lication of their paper, which both strongly affect the  
 1758 expected detections rates.

1759 *Belczynski et al. (2010)*—built upon the work of Nele-  
 1760 mans et al. (2001), by using a different population syn-  
 1761 thesis code with two model variations and a multi-  
 1762 component model for the Milky Way. They find a much  
 1763 lower detection rate for BHNSs and NSNSs (and agreed  
 1764 on zero BHBHs) when compared to Nelemans  
 1765 et al. (2001). They state that this discrepancy from Nelemans  
 1766 et al. (2001) comes from differences in their population  
 1767 synthesis and an overall lower formation rate rather than  
 1768 any changes to LISA detectability. The low total de-  
 1769 tection rate for all DCOs in this paper compared to  
 1770 our work is unsurprising given the relatively high SNR  
 1771 threshold of 10 and short mission length of 1 year. The  
 1772 reduced mission length means that the source signal has  
 1773 much less time to accumulate, whilst also fewer WD-  
 1774 WDs can be resolved in this time, leading to a weaker  
 1775 signal and an increased Galactic confusion noise relative  
 1776 to our work.

1777 *Liu & Zhang (2014)*—performed a similar investigation  
 1778 using a different population synthesis code and find  
 1779 higher rates than earlier works. Their lower detection  
 1780 threshold and longer mission length compared to Bel-  
 1781 czynski et al. (2010) likely explains the relatively in-  
 1782 creased rates. Yet their rates are still significantly below  
 1783 what we find. This could be for several reasons; they as-  
 1784 sume all binaries are circular both in their evolution and  
 1785 for detection. This means that systems may not have  
 1786 inspiralled as far before the LISA mission or may appear  
 1787 to have weaker gravitational waves when eccentricity is  
 1788 not accounted for. They also use a simplified model  
 1789 for the Milky Way with a single disc of one metallicity  
 1790 and constant star formation, whilst also using a mission  
 1791 length half what we assume. Each of these factors likely  
 1792 contributes to the lower overall detection rates.

First Author	Year	Predicted DCO Detection Rates						Population Synthesis				
		BHBH		BHNS		NSNS		Code	Open Source Code	Metallicity	Binary Physics Variations	
<i>Wagg</i>	2021	6-154	9-238	2-198	3-289	3-35	4-57	COMPAS	✓	53 bins between [1e-4, 3e-2]	20	
<i>Shao</i>	2021	12	2	X		BSE	✓		0.02	Fryer rapid, Mandel & Mueller remnant mass		
<i>Breivik</i>	2020	72	19	10		COSMIC	✓		0.02, 0.003	None		
<i>Lau</i>	2020	X	X	35		COMPAS	✓		0.0142	Case BB always unstable, Single SN, alpha=0.1		
<i>Sesana</i>	2020	4.2	6.5	X	X	BSE	✓		13 bins between [1e-4, 3e-2]	None		
<i>Lamberts</i>	2018	25	X	X		BSE	✓		13 bins between [1e-4, 3e-2]	None		
<i>Liu</i>	2014	6	3	16		BSE	✓		0.02	None		
<i>Belczynski</i>	2010	2.3	0	0.2	0	4	1.7	Startrack	X	0.02 (disc, bulge), 0.001 (halo)	Optimistic CE, Pessimistic CE	
<i>Nelemans</i>	2001	0	3	39		SeBa	✓		0.02	None		

First Author	Year	Galaxy and Positioning						Detection			
		Star formation history			Spatial distribution		Galactic Components	Metallicity Dependent Distributions	SNR Limit	LISA Mission Time (yr)	Eccentricity Treatment
<i>Wagg</i>	2021	Exponential 8-0 Gyr ago (thin disc), Exponential 12-8 Gyr ago (thick disc), Skewed gaussian 0-6 Gyr (bulge)		Exponential radial and vertical, different scale length/height for each component, thin disc has inside-out growth		Thin disc, thick disc, bulge	✓	7	4, 10	Full	
<i>Shao</i>	2021	Constant over 10 Gyr		Uniform flat disc of 15 kpc		Single disc	X	5	4	Full	
<i>Breivik</i>	2020	Constant over 10 Gyr (thin disc), 1 Gyr burst 10 Gyr ago (bulge), 1 Gyr burst 11 Gyr (thick disc)		McMillan 2011		Thin disc, thick disc, bulge	X	7	4	Full	
<i>Lau</i>	2020	Constant		Miyamoto & Nagai potential (disc), Wilkinson & Evans potential (halo)		Single disc or halo	X	8	4	Full	
<i>Sesana</i>	2020	FIRE simulation		FIRE simulation		Everything within 300kpc	✓	7	4, 10	Ignored during detection	
<i>Lamberts</i>	2018	FIRE simulation		FIRE simulation		Everything within 300kpc	✓	5	4	Ignored during detection	
<i>Liu</i>	2014	Constant over 13.7 Gyr		Exponential radial, sech^2 vertical (Benacquista+2007)		Single disc	X	7	2	Assumed circular	
<i>Belczynski</i>	2010	Constant over 10 Gyr (disc), 1 Gyr burst 10 Gyr ago (bulge), burst at 13 Gyr (halo)		Exponential sphere (bulge), exponential radial and vertical (disc), spherical shell (halo)		Disc, bulge, halo	X	10	1	Full	
<i>Nelemans</i>	2001	Exponential over 10 Gyr		Exponential radial, sech^2 vertical		Single disc	X	1, 5	1	Full	

**Figure 12.** A table comparing previous studies of a similar nature to this work. In the detection rate section darker shades of blue indicate higher detection rates. In other sections, darker shades of green indicate more detailed models or more accurate choices. Entries in detection rates with two values listed correspond to the different mission lengths (penultimate column). The works listed in the table are Nelemans et al. (2001), Belczynski et al. (2010), Liu & Zhang (2014), Lamberts et al. (2018), Sesana et al. (2020), Lau et al. (2020), Breivik et al. (2020) and Shao & Li (2021).   

*Lamberts et al. (2018)*—presented a new approach to the problem by using the FIRE simulation (*Hopkins et al. 2014*) to distribute their sources rather than an analytical model of the Milky Way and were the first paper in this area to incorporate metallicity dependence into their Milky Way model. *Sesana et al. (2020)* followed up on this paper using the same simulated BHBH population and presented updated results for the number of expected BHBH detections. They find significantly fewer BHBHs than our fiducial model despite using the same SNR threshold and LISA mission length. The discrepancy between the results of *Sesana et al. (2020)* and those presented in this work could be caused by different treatments of eccentricity. Unlike our work, *Sesana et al. (2020)* assume that all binaries are circular for the purpose of detection in LISA, which could result in a lower number of detections by missing eccentric binaries that appear as weaker signals when assumed to be circular. This is especially relevant as we find that around 87% of LISA detectable BHBHs are not circular and around 21% have significant eccentricity (see Fig. 3d). We also improve upon this work by using a larger number of metallicity bins compared to *Sesana et al. (2020)*, since a low number of metallicity bins can produce artificial features in the mass distribution of DCOs and possibly affect the detection rate (see *Dominik et al. 2015; Neijssel et al. 2019; Kummer 2020*, and also appendix D for further discussion). Finally, it could be that different implicit assumptions in their population synthesis code lead to differences in our results (*Toonen et al. 2014*).

*Lau et al. (2020)*—focussed on the number of Galactic NSNS binaries that could be detected by LISA. Their study uses the same population synthesis code, COMPAS, as this work, though an earlier version. Despite this, their study finds a much larger number of detections. They make several different physical assumptions in their population synthesis, using the *Fryer et al. (2012)* rapid remnant mass prescription, assuming the optimistic CE scenario, limiting the maximum neutron star mass to  $2 M_{\odot}$  and not implementing PISN. However, we note that none of these assumptions strongly affect the NSNS LISA detection rate (see bottom panel of Fig. 8, models K, L, M and O) and so this is unlikely to entirely account for the differences. It is also important to highlight that COMPAS has received several improvements and bug fixes since *Vigna-Gómez et al. (2018)* (which contains the simulations used by *Lau et al. 2020*) and these could possibly have affected the formation rate of NSNSs.

Yet it is most likely that the remaining difference between our results is due to way in which we simulate the Milky Way. *Lau et al. (2020)* use a model for the Milky

Way similar to that of *Breivik et al. (2020)*, which we use to estimate the impact of the choice of MW model in Appendix D. The Milky Way model by *Breivik et al. (2020)* applies only two metallicity bins, while we consider a range of metallicities between  $10^{-4}$  and 0.03. When applying the simpler model for the Milky Way, we find that the NSNS detection rate is increased by at least a factor of two. *Lau et al. (2020)* only uses a single metallicity, and so assuming that all star formation happens at a single high metallicity (which has a high efficiency of producing NSNS), could lead to an even greater overestimate of the detection rate. Hence, we expect the low number of metallicity bins in their Milky Way model to be the main driver behind the discrepancy between our results.

*Breivik et al. (2020)*—introduced the population synthesis code COSMIC and presented detections for many different DCO types in LISA using this code. They find that LISA will detect **72 BHBHs, 19 BHNSs and 10 NSNSs** in the Milky Way over a 4 year mission. *Breivik et al. (2020)* make many physical assumptions that differ from our fiducial model, the most notable being that they assume the optimistic CE scenario and that case BB mass transfer is always unstable, whilst also using a simpler model for the Milky Way (see Appendix D). Thus for better comparison we ran our simulation using model F and the Milky Way model from *Breivik et al. (2020)*. This results in 97, 101 and 43 detections for BHBHs, BHNSs and NSNSs respectively. **Therefore, though our BHBH rates agree reasonably well, we predict much higher rates for BHNSs and NSNSs.** These differences are likely due to using a different population synthesis code (COSMIC), which has different underlying physics assumptions from COMPAS. Given our strong agreement for BHBHs, it is possible that COSMIC and COMPAS handle NSs differently and so lead to different detection rates for DCOs containing NSs. However checking this would require a more in-depth study of the intrinsic formation rate of DCOs containing NSs in the two codes.

*Shao & Li (2021)*—most recently investigated the detectability binaries containing BHs in LISA using BSE and a relatively simple model for the Milky Way (assuming a uniform flat disc, constant star formation and a single metallicity). They assume that kicks for NSs formed through ECSN are slightly higher than our work ( $50 \text{ km s}^{-1}$  instead of  $30 \text{ km s}^{-1}$ ). This may account for their particularly low BHNS rate (as the binaries would be more likely to disrupt), which is a factor of 20 lower than ours, but we expect their assumption of the optimistic CE scenario, reduced Wolf-Rayet winds

and lower SNR detection threshold could partially offset this. As we show in Appendix D, their use of a simpler Milky Way model, especially with only a single metallicity, would lead to an underestimate of the BHBH and BHNS rates, which may explain the discrepancy in our results.

Overall, since the work of Nelemans et al. (2001), in addition to the LISA mission specifications, the methods that we use to simulate binaries and the Milky Way have all changed significantly. We now predict that LISA detections of these massive DCOs are dominated by BHBHs, rather than NSNSs, whilst the absolute detection rates for BHBHs and BHNSs are much higher. Further studies in this area could improve on this work by including the effects of systemic kicks on the position of systems in the Milky Way and accounting for contributions from other formation channels.

## 7. CONCLUSION & SUMMARY

We provide predictions for the detection rate and population properties of LISA detectable BHBH, BHNS and NSNS. We use a novel empirically-informed analytical model for the metallicity dependent star formation history of the Milky Way, calibrated against the APOGEE stellar spectroscopic survey. We use this to model Monte-Carlo realisations of the present-day BHBH, BHNS and NSNS populations in our Milky Way. For the binary population, we use the results of a large grid of simulations performed with the rapid population synthesis code COMPAS, which can reproduce the current constraints on the overall GW rates (Broekgaarden et al. 2021a,b; The LIGO Scientific Collaboration et al. 2021c). Our suite of simulations consider 20 physics variations, which represent the most common uncertainties in binary physics. We investigate the detectability of sources in the planned space-based GW detector LISA using the LEGWORK package (Wagg et al. 2021), that we specifically developed for this purpose and is publicly available. We investigate the results expected for a 4- and 10-year LISA mission. Our main conclusions can be summarised as:

- 1. Total detections:** We predict 30-370 detections in a 4-year LISA mission, across all our simulations for varying physics assumptions. This increases to about 50-550 for a 10-year LISA mission. Although the number of detections per type can vary by about 2 orders of magnitude, we find that the total detection rate is fairly robust, among the variations we have considered (see Table F1).

- 2. Detections by type:** For our fiducial model, we predict a total of  $124 \pm 11$  detections and out of

these we find about  $74 \pm 9$  BHBHs,  $42 \pm 6$  BHNSs and  $8 \pm 3$  NSNSs. The errors quoted here are the  $1-\sigma$  Poisson uncertainties resulting from the random initialisation of the Milky Way (see Table F1).

**3. Physics variations:** Among the model variations we consider, we find that our predictions for the rates for the different DCO types are robust within a factor of 2 of the fiducial rate, with the following exceptions. For BHBHs, the rate is most sensitive to the treatment of common envelope phases or an increase of the WR wind mass loss. For BHNSs and NSNSs, the assumptions regarding the assumed common envelope ejection efficiency, treatment of case BB mass transfer and the kicks are most important. In addition, the assumed mass transfer efficiency impacts the BHNS (see Fig. 8).

**4. Probing the black hole mass distribution and the lower mass gap:** We expect LISA to predominantly detect lower mass BHs (with 90% of BHBH and BHNSs having BH masses lower than  $11 M_\odot$  in our fiducial simulations). This is in stark contrast to current ground-based detectors which are heavily biased towards high mass systems, since they can be detected out to larger distances. We predict that between 15-156 systems with a component with a mass between  $2.5-5 M_\odot$  would be detected by a 4-year LISA, for our different physics variations. An exception is model using the Fryer Rapid remnant mass prescription, which produces none. However, it will likely be hard for LISA data to make a significant impact on this debate on the existence of the lower mass gap given the uncertainty of the individual masses (see Fig. 9).

**5. Eccentricity distribution:** We find that for all DCO types a large fraction of detectable systems still have nonzero eccentricities ( $e > 0.01$ ) when entering the LISA band, which can be used to distinguish them from the more numerous WDWD binaries, which are largely expected to be circular. In particular, for our fiducial model, we find that this is the case for around three quarters of detectable binaries. Furthermore, around 16% of detectable binaries have eccentricities that are so high ( $e > 0.3$ ) that the emission at frequencies corresponding to higher order harmonics start to dominate (see Fig. 3).

**6. Distinguishing from WDWD sources:** For about half of all detections we expect that we will

be able to confidently determine the type of compact objects involved and this increases to 60% for a 10-year LISA mission (see Sec. 5.1.1).

**7. Chirp mass determinations:** For about 10% of systems we expect to be able to determine the chirp mass better than 10% and this increases to 15% for a 10-year LISA mission (see Fig. 6).

**8. Prospects for finding EM counterparts:** We expect about 13% of detections with a sky localisation better than 1 degree for our fiducial model (though the fraction remains roughly constant among model variations). This fraction remains the same for a 10-year LISA mission, meaning that the number increases proportionally. This will be of interest for electromagnetic searches for counterparts, in particular for radio pulsar searches with SKA (see Fig. 5.2).

**9. Benefits of extending the LISA mission:** The number of detections scale approximately as  $\sqrt{T_{\text{obs}}}$ , where  $T_{\text{obs}}$  is the mission length. Therefore, extending the LISA mission from 4- to 10-years increases the number of detections by about 60% for each model variation. A further important benefit is the improvement of the characterisation of the sources, since the relative error on the frequency derivative (which dominates the relative error in the chirp mass) scales as  $T_{\text{obs}}^{-2.5}$  for stationary sources (Eq. C5). We find that the number of systems with chirp masses that can be measured better than 10% increases by a factor of 2.4 for each model variation. In addition, the number of systems with a sky localisation better than one degree increases by a factor of 1.5. Overall, the number of sources that can be unambiguously distinguished from WDWDs increases by almost a factor of 2 (see Section 5.1.1).

## ACKNOWLEDGMENTS

We thank Katie Brevik, Will Farr, Rob Farmer, Valeriya Korol, Floris Kummer, Eva Laplace, Mike Lau, Tyson Littenberg, Ilya Mandel, Mathieu Renzo, Alberto Sesana, Katie Sharpe, Simon Stevenson, the CCA GW group and COMPAS collaboration for insightful discussions. TW also thanks Terence Lovatt for his advice and help on improving an earlier draft of this project. Portions of this study were inspired by the LISA Sprint at the Center for Computational Astrophysics of the Flatiron Institute, supported by the Simons Foundation. This project was funded in part by the National Science Foundation under Grant No. (NSF grant number 2009131), the European Union’s Horizon 2020 research and innovation program from the European Research Council (ERC, Grant agreement No. 715063), and by the Netherlands Organization for Scientific Research (NWO) as part of the Vidi research program Bin-Waves with project number 639.042.728. We further acknowledge the Black Hole Initiative funded by a generous contribution of the John Templeton Foundation and the Gordon and Betty Moore Foundation.

**Software:** We used LEGWORK to evolve sources over time and calculate signal-to-noise ratios (Wagg et al. 2021). It is freely available at <https://legwork.readthedocs.io/en/latest/>. Simulations in this paper made use of the COMPAS rapid binary population synthesis code (Team COMPAS: J. Riley et al. 2021). The simulations performed in this work were simulated with a COMPAS version that predates the publicly available code. Our version is most similar to v02.13.01 of the publicly available COMPAS code. Requests for the original code can be made to Floor Broekgaarden. The authors used STROOPWAFEL from (Broekgaarden et al. 2019), publicly available at <https://github.com/FloorBroekgaarden/STROOPWAFEL><sup>7</sup>. The authors also made use of Python (v3.8), available at <http://www.python.org>. In addition the following Python packages were used: matplotlib (Hunter 2007), NumPy (Harris et al. 2020), Astropy (Astropy Collaboration et al. 2013, 2018), Seaborn (Waskom 2021), SciPy (Virtanen et al. 2020), h5py (Collette et al. 2021) and Jupyter Lab (Kluyver et al. 2016). This research has made use of NASA’s Astrophysics Data System Bibliographic Services. We also made use of the computational facilities from the Harvard FAS Research Computing cluster.

<sup>7</sup>For the latest pip installable version of STROOPWAFEL please contact Floor Broekgaarden.

## REFERENCES

- 2056 Abbott, B. P., Abbott, R., Abbott, T. D., et al. 2016,  
 2057 Physical Review X, 6, 041015,  
 2058 doi: [10.1103/PhysRevX.6.041015](https://doi.org/10.1103/PhysRevX.6.041015)
- 2059 —. 2019, Physical Review X, 9, 031040,  
 2060 doi: [10.1103/PhysRevX.9.031040](https://doi.org/10.1103/PhysRevX.9.031040)
- 2061 —. 2020a, ApJL, 892, L3, doi: [10.3847/2041-8213/ab75f5](https://doi.org/10.3847/2041-8213/ab75f5)
- 2062 —. 2017a, PhRvL, 119, 161101,  
 2063 doi: [10.1103/PhysRevLett.119.161101](https://doi.org/10.1103/PhysRevLett.119.161101)
- 2064 —. 2017b, ApJL, 850, L40, doi: [10.3847/2041-8213/aa93fc](https://doi.org/10.3847/2041-8213/aa93fc)
- 2065 Abbott, R., Abbott, T. D., Abraham, S., et al. 2020b,  
 2066 arXiv e-prints, arXiv:2010.14527.  
<https://arxiv.org/abs/2010.14527>
- 2067 —. 2020c, ApJL, 896, L44, doi: [10.3847/2041-8213/ab960f](https://doi.org/10.3847/2041-8213/ab960f)
- 2068 —. 2021, ApJL, 913, L7, doi: [10.3847/2041-8213/abe949](https://doi.org/10.3847/2041-8213/abe949)
- 2069 Abdul-Masih, M., Banyard, G., Bodensteiner, J., et al.  
 2070 2020, Nature, 580, E11, doi: [10.1038/s41586-020-2216-x](https://doi.org/10.1038/s41586-020-2216-x)
- 2071 Abt, H. A. 1983, ARA&A, 21, 343,  
 2072 doi: [10.1146/annurev.aa.21.090183.002015](https://doi.org/10.1146/annurev.aa.21.090183.002015)
- 2073 Amaro-Seoane, P., Audley, H., Babak, S., et al. 2017, arXiv  
 2074 e-prints, arXiv:1702.00786.  
<https://arxiv.org/abs/1702.00786>
- 2075 Antoniadis, J., Tauris, T. M., Ozel, F., et al. 2016, arXiv  
 2076 e-prints, arXiv:1605.01665.  
<https://arxiv.org/abs/1605.01665>
- 2077 Antonini, F., & Rasio, F. A. 2016, ApJ, 831, 187,  
 2078 doi: [10.3847/0004-637X/831/2/187](https://doi.org/10.3847/0004-637X/831/2/187)
- 2079 Antonini, F., Toonen, S., & Hamers, A. S. 2017, ApJ, 841,  
 2080 77, doi: [10.3847/1538-4357/aa6f5e](https://doi.org/10.3847/1538-4357/aa6f5e)
- 2081 Astropy Collaboration, Price-Whelan, A. M., Sipőcz, B. M.,  
 2082 et al. 2018, AJ, 156, 123, doi: [10.3847/1538-3881/aabc4f](https://doi.org/10.3847/1538-3881/aabc4f)
- 2083 Astropy Collaboration, Robitaille, T. P., Tollerud, E. J.,  
 2084 et al. 2013, A&A, 558, A33,  
 2085 doi: [10.1051/0004-6361/201322068](https://doi.org/10.1051/0004-6361/201322068)
- 2086 Banerjee, S. 2020, PhRvD, 102, 103002,  
 2087 doi: [10.1103/PhysRevD.102.103002](https://doi.org/10.1103/PhysRevD.102.103002)
- 2088 Barack, L., & Cutler, C. 2004, PhRvD, 69, 082005,  
 2089 doi: [10.1103/PhysRevD.69.082005](https://doi.org/10.1103/PhysRevD.69.082005)
- 2090 Bates, S. D., Lorimer, D. R., Rane, A., & Swiggum, J.  
 2091 2014, MNRAS, 439, 2893, doi: [10.1093/mnras/stu157](https://doi.org/10.1093/mnras/stu157)
- 2092 Begelman, M. C., Blandford, R. D., & Rees, M. J. 1980,  
 2093 Nature, 287, 307, doi: [10.1038/287307a0](https://doi.org/10.1038/287307a0)
- 2094 Belczynski, K., Benacquista, M., & Bulik, T. 2010, ApJ,  
 2095 725, 816, doi: [10.1088/0004-637X/725/1/816](https://doi.org/10.1088/0004-637X/725/1/816)
- 2096 Belczynski, K., Holz, D. E., Bulik, T., & O’Shaughnessy, R.  
 2097 2016, Nature, 534, 512, doi: [10.1038/nature18322](https://doi.org/10.1038/nature18322)
- 2098 Belczynski, K., Kalogera, V., Rasio, F. A., et al. 2008,  
 2099 ApJS, 174, 223, doi: [10.1086/521026](https://doi.org/10.1086/521026)
- 2100 Belczynski, K., Taam, R. E., Kalogera, V., Rasio, F. A., &  
 2101 Bulik, T. 2007, ApJ, 662, 504, doi: [10.1086/513562](https://doi.org/10.1086/513562)
- 2102 Berger, E. 2014, ARA&A, 52, 43,  
 2103 doi: [10.1146/annurev-astro-081913-035926](https://doi.org/10.1146/annurev-astro-081913-035926)
- 2104 Bertelli, G., Bressan, A., Chiosi, C., Fagotto, F., & Nasi, E.  
 2105 1994, A&AS, 106, 275
- 2106 Blaauw, A. 1961, BAN, 15, 265
- 2107 Boersma, J. 1961, BAN, 15, 291
- 2108 Bolton, C. T. 1972, Nature, 235, 271, doi: [10.1038/235271b0](https://doi.org/10.1038/235271b0)
- 2109 Bovy, J., Leung, H. W., Hunt, J. A. S., et al. 2019,  
 2110 MNRAS, 490, 4740, doi: [10.1093/mnras/stz2891](https://doi.org/10.1093/mnras/stz2891)
- 2111 Bovy, J., Rix, H.-W., Schlaufly, E. F., et al. 2016, ApJ, 823,  
 2112 30, doi: [10.3847/0004-637X/823/1/30](https://doi.org/10.3847/0004-637X/823/1/30)
- 2113 Brandt, N., & Podsiadlowski, P. 1995, MNRAS, 274, 461,  
 2114 doi: [10.1093/mnras/274.2.461](https://doi.org/10.1093/mnras/274.2.461)
- 2115 Breivik, K., Coughlin, S., Zevin, M., et al. 2020, ApJ, 898,  
 2116 71, doi: [10.3847/1538-4357/ab9d85](https://doi.org/10.3847/1538-4357/ab9d85)
- 2117 Breivik, K., Rodriguez, C. L., Larson, S. L., Kalogera, V.,  
 2118 & Rasio, F. A. 2016, ApJL, 830, L18,  
 2119 doi: [10.3847/2041-8205/830/1/L18](https://doi.org/10.3847/2041-8205/830/1/L18)
- 2120 Broekgaarden, F. S. 2021a, BHBH simulations from:  
 2121 Impact of Massive Binary Star and Cosmic Evolution on  
 2122 Gravitational Wave Observations II: Double Compact  
 2123 Object Mergers, 1, Zenodo, doi: [10.5281/zenodo.5651073](https://doi.org/10.5281/zenodo.5651073)
- 2124 —. 2021b, BHNS simulations from: Impact of Massive  
 2125 Binary Star and Cosmic Evolution on Gravitational  
 2126 Wave Observations II: Double Compact Object Mergers,  
 2127 1, Zenodo, doi: [10.5281/zenodo.5178777](https://doi.org/10.5281/zenodo.5178777)
- 2128 —. 2021c, NSNS simulations from: Impact of Massive  
 2129 Binary Star and Cosmic Evolution on Gravitational  
 2130 Wave Observations II: Double Compact Object Mergers,  
 2131 1, Zenodo, doi: [10.5281/zenodo.5189849](https://doi.org/10.5281/zenodo.5189849)
- 2132 Broekgaarden, F. S., Berger, E., Neijssel, C. J., et al.  
 2133 2021a, arXiv e-prints, arXiv:2103.02608.  
<https://arxiv.org/abs/2103.02608>
- 2134 Broekgaarden, F. S., Justham, S., de Mink, S. E., et al.  
 2135 2019, MNRAS, 490, 5228, doi: [10.1093/mnras/stz2558](https://doi.org/10.1093/mnras/stz2558)
- 2136 Broekgaarden, F. S., Berger, E., Stevenson, S., et al. 2021b,  
 2137 arXiv e-prints, arXiv:2112.05763.  
<https://arxiv.org/abs/2112.05763>
- 2138 Brown, G. E. 1995, ApJ, 440, 270, doi: [10.1086/175268](https://doi.org/10.1086/175268)
- 2139 Chandrasekhar, S. 1931, ApJ, 74, 81, doi: [10.1086/143324](https://doi.org/10.1086/143324)
- 2140 Chattopadhyay, D., Stevenson, S., Hurley, J. R., Bailes,  
 2141 M., & Broekgaarden, F. 2020, arXiv e-prints,  
 2142 arXiv:2011.13503. <https://arxiv.org/abs/2011.13503>
- 2143 Chruslinska, M., Belczynski, K., Bulik, T., & Gladysz, W.  
 2144 2017, AcA, 67, 37
- 2145 Collette, A., Kluyver, T., Caswell, T. A., et al. 2021,  
 2146 h5py/h5py: 3.3.0, 3.3.0, Zenodo,  
 2147 doi: [10.5281/zenodo.594310](https://doi.org/10.5281/zenodo.594310)

- 2153 Colpi, M., Holley-Bockelmann, K., Bogdanovic, T., et al.  
 2154 2019, arXiv e-prints, arXiv:1903.06867.  
 2155 <https://arxiv.org/abs/1903.06867>
- 2156 Corral-Santana, J. M., Casares, J., Muñoz-Darias, T., et al.  
 2157 2016, A&A, 587, A61, doi: [10.1051/0004-6361/201527130](https://doi.org/10.1051/0004-6361/201527130)
- 2158 de Kool, M. 1990, ApJ, 358, 189, doi: [10.1086/168974](https://doi.org/10.1086/168974)
- 2159 De Marco, O., Passy, J.-C., Moe, M., et al. 2011, MNRAS,  
 2160 411, 2277, doi: [10.1111/j.1365-2966.2010.17891.x](https://doi.org/10.1111/j.1365-2966.2010.17891.x)
- 2161 de Mink, S. E., & Belczynski, K. 2015, ApJ, 814, 58,  
 2162 doi: [10.1088/0004-637X/814/1/58](https://doi.org/10.1088/0004-637X/814/1/58)
- 2163 de Mink, S. E., Cantiello, M., Langer, N., et al. 2009, A&A,  
 2164 497, 243, doi: [10.1051/0004-6361/200811439](https://doi.org/10.1051/0004-6361/200811439)
- 2165 de Mink, S. E., Pols, O. R., & Hilditch, R. W. 2007, A&A,  
 2166 467, 1181
- 2167 Dewdney, P. E., Hall, P. J., Schilizzi, R. T., & Lazio,  
 2168 T. J. L. W. 2009, IEEE Proceedings, 97, 1482,  
 2169 doi: [10.1109/JPROC.2009.2021005](https://doi.org/10.1109/JPROC.2009.2021005)
- 2170 Dewi, J. D. M., Pols, O. R., Savonije, G. J., & van den  
 2171 Heuvel, E. P. J. 2002, MNRAS, 331, 1027,  
 2172 doi: [10.1046/j.1365-8711.2002.05257.x](https://doi.org/10.1046/j.1365-8711.2002.05257.x)
- 2173 Di Carlo, U. N., Mapelli, M., Giacobbo, N., et al. 2020,  
 2174 MNRAS, 498, 495, doi: [10.1093/mnras/staa2286](https://doi.org/10.1093/mnras/staa2286)
- 2175 Dominik, M., Berti, E., O'Shaughnessy, R., et al. 2015,  
 2176 ApJ, 806, 263, doi: [10.1088/0004-637X/806/2/263](https://doi.org/10.1088/0004-637X/806/2/263)
- 2177 Dosopoulou, F., & Kalogera, V. 2016a, ApJ, 825, 70,  
 2178 doi: [10.3847/0004-637X/825/1/70](https://doi.org/10.3847/0004-637X/825/1/70)
- 2179 —. 2016b, ApJ, 825, 71, doi: [10.3847/0004-637X/825/1/71](https://doi.org/10.3847/0004-637X/825/1/71)
- 2180 du Buisson, L., Marchant, P., Podsiadlowski, P., et al. 2020,  
 2181 MNRAS, 499, 5941, doi: [10.1093/mnras/staa3225](https://doi.org/10.1093/mnras/staa3225)
- 2182 Edelman, B., Doctor, Z., Godfrey, J., & Farr, B. 2022, ApJ,  
 2183 924, 101, doi: [10.3847/1538-4357/ac3667](https://doi.org/10.3847/1538-4357/ac3667)
- 2184 Eichler, D., Livio, M., Piran, T., & Schramm, D. N. 1989,  
 2185 Nature, 340, 126, doi: [10.1038/340126a0](https://doi.org/10.1038/340126a0)
- 2186 El-Badry, K., & Quataert, E. 2020, MNRAS, 493, L22,  
 2187 doi: [10.1093/mnrasl/slaa004](https://doi.org/10.1093/mnrasl/slaa004)
- 2188 Eldridge, J. J., Stanway, E. R., Breivik, K., et al. 2020,  
 2189 MNRAS, 495, 2786, doi: [10.1093/mnras/staa1324](https://doi.org/10.1093/mnras/staa1324)
- 2190 Farah, A. M., Fishbach, M., Essick, R., Holz, D. E., &  
 2191 Galauadage, S. 2021, arXiv e-prints, arXiv:2111.03498.  
 2192 <https://arxiv.org/abs/2111.03498>
- 2193 Farmer, R., Renzo, M., de Mink, S. E., Marchant, P., &  
 2194 Justham, S. 2019, ApJ, 887, 53,  
 2195 doi: [10.3847/1538-4357/ab518b](https://doi.org/10.3847/1538-4357/ab518b)
- 2196 Farr, W. M., Sravan, N., Cantrell, A., et al. 2011, ApJ, 741,  
 2197 103, doi: [10.1088/0004-637X/741/2/103](https://doi.org/10.1088/0004-637X/741/2/103)
- 2198 Finn, L. S., & Thorne, K. S. 2000, PhRvD, 62, 124021,  
 2199 doi: [10.1103/PhysRevD.62.124021](https://doi.org/10.1103/PhysRevD.62.124021)
- 2200 Frankel, N., Rix, H.-W., Ting, Y.-S., Ness, M., & Hogg,  
 2201 D. W. 2018, ApJ, 865, 96,  
 2202 doi: [10.3847/1538-4357/aadba5](https://doi.org/10.3847/1538-4357/aadba5)
- 2203 Fryer, C. L., Belczynski, K., Ramirez-Ruiz, E., et al. 2015,  
 2204 ApJ, 812, 24, doi: [10.1088/0004-637X/812/1/24](https://doi.org/10.1088/0004-637X/812/1/24)
- 2205 Fryer, C. L., Belczynski, K., Wiktorowicz, G., et al. 2012,  
 2206 ApJ, 749, 91, doi: [10.1088/0004-637X/749/1/91](https://doi.org/10.1088/0004-637X/749/1/91)
- 2207 Gerosa, D., Ma, S., Wong, K. W. K., et al. 2019, PhRvD,  
 2208 99, 103004, doi: [10.1103/PhysRevD.99.103004](https://doi.org/10.1103/PhysRevD.99.103004)
- 2209 Ginat, Y. B., Glanz, H., Perets, H. B., Grishin, E., &  
 2210 Desjacques, V. 2020, MNRAS, 493, 4861,  
 2211 doi: [10.1093/mnras/staa465](https://doi.org/10.1093/mnras/staa465)
- 2212 Gosnell, N. M., Leiner, E. M., Mathieu, R. D., et al. 2019,  
 2213 ApJ, 885, 45, doi: [10.3847/1538-4357/ab4273](https://doi.org/10.3847/1538-4357/ab4273)
- 2214 Griffith, E., Weinberg, D. H., Johnson, J. A., et al. 2021,  
 2215 ApJ, 909, 77, doi: [10.3847/1538-4357/abd6be](https://doi.org/10.3847/1538-4357/abd6be)
- 2216 Hamada, T., & Salpeter, E. E. 1961, ApJ, 134, 683,  
 2217 doi: [10.1086/147195](https://doi.org/10.1086/147195)
- 2218 Hamann, W. R., Gräfener, G., Liermann, A., et al. 2019,  
 2219 A&A, 625, A57, doi: [10.1051/0004-6361/201834850](https://doi.org/10.1051/0004-6361/201834850)
- 2220 Hamann, W. R., & Koesterke, L. 1998, A&A, 335, 1003
- 2221 Harris, C. R., Millman, K. J., van der Walt, S. J., et al.  
 2222 2020, Nature, 585, 357–362,  
 2223 doi: [10.1038/s41586-020-2649-2](https://doi.org/10.1038/s41586-020-2649-2)
- 2224 Hjellming, M. S., & Webbink, R. F. 1987, ApJ, 318, 794,  
 2225 doi: [10.1086/165412](https://doi.org/10.1086/165412)
- 2226 Hobbs, G., Lorimer, D. R., Lyne, A. G., & Kramer, M.  
 2227 2005, MNRAS, 360, 974,  
 2228 doi: [10.1111/j.1365-2966.2005.09087.x](https://doi.org/10.1111/j.1365-2966.2005.09087.x)
- 2229 Hopkins, P. F., Kereš, D., Oñorbe, J., et al. 2014, MNRAS,  
 2230 445, 581, doi: [10.1093/mnras/stu1738](https://doi.org/10.1093/mnras/stu1738)
- 2231 Hotokezaka, K., Nissanke, S., Hallinan, G., et al. 2016,  
 2232 ApJ, 831, 190, doi: [10.3847/0004-637X/831/2/190](https://doi.org/10.3847/0004-637X/831/2/190)
- 2233 Hulse, R. A., & Taylor, J. H. 1975, ApJL, 195, L51,  
 2234 doi: [10.1086/181708](https://doi.org/10.1086/181708)
- 2235 Hunter, J. D. 2007, Computing in Science and Engineering,  
 2236 9, 90, doi: [10.1109/MCSE.2007.55](https://doi.org/10.1109/MCSE.2007.55)
- 2237 Hurley, J. R., Pols, O. R., & Tout, C. A. 2000, MNRAS,  
 2238 315, 543, doi: [10.1046/j.1365-8711.2000.03426.x](https://doi.org/10.1046/j.1365-8711.2000.03426.x)
- 2239 Hurley, J. R., Tout, C. A., & Pols, O. R. 2002, MNRAS,  
 2240 329, 897, doi: [10.1046/j.1365-8711.2002.05038.x](https://doi.org/10.1046/j.1365-8711.2002.05038.x)
- 2241 Ivanova, N., Heinke, C. O., Rasio, F. A., Belczynski, K., &  
 2242 Fregeau, J. M. 2008, MNRAS, 386, 553,  
 2243 doi: [10.1111/j.1365-2966.2008.13064.x](https://doi.org/10.1111/j.1365-2966.2008.13064.x)
- 2244 Ivanova, N., & Taam, R. E. 2004, ApJ, 601, 1058,  
 2245 doi: [10.1086/380561](https://doi.org/10.1086/380561)
- 2246 Ivanova, N., Justham, S., Chen, X., et al. 2013, A&A Rv,  
 2247 21, 59, doi: [10.1007/s00159-013-0059-2](https://doi.org/10.1007/s00159-013-0059-2)
- 2248 Jayasinghe, T., Stanek, K. Z., Thompson, T. A., et al.  
 2249 2021, MNRAS, 504, 2577
- 2250 Kalogera, V., & Baym, G. 1996, ApJL, 470, L61,  
 2251 doi: [10.1086/310296](https://doi.org/10.1086/310296)

- 2252 Kalogera, V., Belczynski, K., Kim, C., O'Shaughnessy, R.,  
 2253 & Willemse, B. 2007, PhR, 442, 75,  
 2254 doi: [10.1016/j.physrep.2007.02.008](https://doi.org/10.1016/j.physrep.2007.02.008)
- 2255 Keane, E., Bhattacharyya, B., Kramer, M., et al. 2015, in  
 2256 Advancing Astrophysics with the Square Kilometre Array  
 2257 (AASKA14), 40. <https://arxiv.org/abs/1501.00056>
- 2258 Klein, A., Barausse, E., Sesana, A., et al. 2016, PhRvD, 93,  
 2259 024003, doi: [10.1103/PhysRevD.93.024003](https://doi.org/10.1103/PhysRevD.93.024003)
- 2260 Klencki, J., Moe, M., Gladysz, W., et al. 2018, A&A, 619,  
 2261 A77
- 2262 Klencki, J., Nelemans, G., Istrate, A. G., & Chruslinska, M.  
 2263 2021, A&A, 645, A54, doi: [10.1051/0004-6361/202038707](https://doi.org/10.1051/0004-6361/202038707)
- 2264 Kluyver, T., Ragan-Kelley, B., Pérez, F., et al. 2016, in  
 2265 Positioning and Power in Academic Publishing: Players,  
 2266 Agents and Agendas, ed. F. Loizides & B. Schmidt, IOS  
 2267 Press, 87 – 90
- 2268 Korol, V., Rossi, E. M., & Barausse, E. 2019, MNRAS, 483,  
 2269 5518, doi: [10.1093/mnras/sty3440](https://doi.org/10.1093/mnras/sty3440)
- 2270 Korol, V., Rossi, E. M., Groot, P. J., et al. 2017, MNRAS,  
 2271 470, 1894, doi: [10.1093/mnras/stx1285](https://doi.org/10.1093/mnras/stx1285)
- 2272 Korol, V., & Safarzadeh, M. 2021, MNRAS, 502, 5576,  
 2273 doi: [10.1093/mnras/stab310](https://doi.org/10.1093/mnras/stab310)
- 2274 Korol, V., Toonen, S., Klein, A., et al. 2020, A&A, 638,  
 2275 A153, doi: [10.1051/0004-6361/202037764](https://doi.org/10.1051/0004-6361/202037764)
- 2276 Kreidberg, L., Bailyn, C. D., Farr, W. M., & Kalogera, V.  
 2277 2012, ApJ, 757, 36, doi: [10.1088/0004-637X/757/1/36](https://doi.org/10.1088/0004-637X/757/1/36)
- 2278 Kremer, K., Chatterjee, S., Breivik, K., et al. 2018, PhRvL,  
 2279 120, 191103, doi: [10.1103/PhysRevLett.120.191103](https://doi.org/10.1103/PhysRevLett.120.191103)
- 2280 Kroupa, P. 2001, MNRAS, 322, 231,  
 2281 doi: [10.1046/j.1365-8711.2001.04022.x](https://doi.org/10.1046/j.1365-8711.2001.04022.x)
- 2282 Kummer, F. 2020, UvA Scripties
- 2283 Kupfer, T., Korol, V., Shah, S., et al. 2018, MNRAS, 480,  
 2284 302, doi: [10.1093/mnras/sty1545](https://doi.org/10.1093/mnras/sty1545)
- 2285 Kyutoku, K., Kiuchi, K., Sekiguchi, Y., Shibata, M., &  
 2286 Taniguchi, K. 2018, PhRvD, 97, 023009,  
 2287 doi: [10.1103/PhysRevD.97.023009](https://doi.org/10.1103/PhysRevD.97.023009)
- 2288 Kyutoku, K., Nishino, Y., & Seto, N. 2019, MNRAS, 483,  
 2289 2615, doi: [10.1093/mnras/sty3322](https://doi.org/10.1093/mnras/sty3322)
- 2290 Lamberts, A., Blunt, S., Littenberg, T. B., et al. 2019,  
 2291 MNRAS, 490, 5888, doi: [10.1093/mnras/stz2834](https://doi.org/10.1093/mnras/stz2834)
- 2292 Lamberts, A., Garrison-Kimmel, S., Hopkins, P. F., et al.  
 2293 2018, MNRAS, 480, 2704, doi: [10.1093/mnras/sty2035](https://doi.org/10.1093/mnras/sty2035)
- 2294 Langer, N. 2012, ARA&A, 50, 107
- 2295 Laplace, E., Götzberg, Y., de Mink, S. E., Justham, S., &  
 2296 Farmer, R. 2020, A&A, 637, A6
- 2297 Lau, M. Y. M., Hirai, R., González-Bolívar, M., et al. 2021,  
 2298 arXiv e-prints, arXiv:2111.00923.  
 2299 <https://arxiv.org/abs/2111.00923>
- 2300 Lau, M. Y. M., Mandel, I., Vigna-Gómez, A., et al. 2020,  
 2301 MNRAS, 492, 3061, doi: [10.1093/mnras/staa002](https://doi.org/10.1093/mnras/staa002)
- 2302 Law-Smith, J. A. P., Everson, R. W., Ramirez-Ruiz, E.,  
 2303 et al. 2020, arXiv e-prints, arXiv:2011.06630.  
 2304 <https://arxiv.org/abs/2011.06630>
- 2305 Li, L.-X., & Paczyński, B. 1998, ApJL, 507, L59,  
 2306 doi: [10.1086/311680](https://doi.org/10.1086/311680)
- 2307 Li, Y.-J., Wang, Y.-Z., Han, M.-Z., et al. 2021, ApJ, 917,  
 2308 33, doi: [10.3847/1538-4357/ac0971](https://doi.org/10.3847/1538-4357/ac0971)
- 2309 Licquia, T. C., & Newman, J. A. 2015, ApJ, 806, 96,  
 2310 doi: [10.1088/0004-637X/806/1/96](https://doi.org/10.1088/0004-637X/806/1/96)
- 2311 Liu, J., Soria, R., Zheng, Z., et al. 2020, Nature, 580, E16,  
 2312 doi: [10.1038/s41586-020-2217-9](https://doi.org/10.1038/s41586-020-2217-9)
- 2313 Liu, J., Zhang, H., Howard, A. W., et al. 2019, Nature, 575,  
 2314 618, doi: [10.1038/s41586-019-1766-2](https://doi.org/10.1038/s41586-019-1766-2)
- 2315 Liu, J., & Zhang, Y. 2014, PASP, 126, 211,  
 2316 doi: [10.1086/675721](https://doi.org/10.1086/675721)
- 2317 Lyne, A. G., & Lorimer, D. R. 1994, Nature, 369, 127,  
 2318 doi: [10.1038/369127a0](https://doi.org/10.1038/369127a0)
- 2319 Majewski, S. R., Schiavon, R. P., Frinchaboy, P. M., et al.  
 2320 2017, AJ, 154, 94, doi: [10.3847/1538-3881/aa784d](https://doi.org/10.3847/1538-3881/aa784d)
- 2321 Manchester, R. N., Hobbs, G. B., Teoh, A., & Hobbs, M.  
 2322 2005, AJ, 129, 1993, doi: [10.1086/428488](https://doi.org/10.1086/428488)
- 2323 Mandel, I., & de Mink, S. E. 2016, MNRAS, 458, 2634,  
 2324 doi: [10.1093/mnras/stw379](https://doi.org/10.1093/mnras/stw379)
- 2325 Mandel, I., & Müller, B. 2020, MNRAS, 499, 3214,  
 2326 doi: [10.1093/mnras/staa3043](https://doi.org/10.1093/mnras/staa3043)
- 2327 Mandel, I., Sesana, A., & Vecchio, A. 2018, Classical and  
 2328 Quantum Gravity, 35, 054004,  
 2329 doi: [10.1088/1361-6382/aaa7e0](https://doi.org/10.1088/1361-6382/aaa7e0)
- 2330 Mapelli, M. 2021, Formation Channels of Single and Binary  
 2331 Stellar-Mass Black Holes (Springer), 4,  
 2332 doi: [10.1007/978-981-15-4702-7\\_16-1](https://doi.org/10.1007/978-981-15-4702-7_16-1)
- 2333 Marchant, P., Langer, N., Podsiadlowski, P., et al. 2017,  
 2334 A&A, 604, A55, doi: [10.1051/0004-6361/201630188](https://doi.org/10.1051/0004-6361/201630188)
- 2335 Marchant, P., Langer, N., Podsiadlowski, P., Tauris, T. M.,  
 2336 & Moriya, T. J. 2016, A&A, 588, A50,  
 2337 doi: [10.1051/0004-6361/201628133](https://doi.org/10.1051/0004-6361/201628133)
- 2338 Marchant, P., Renzo, M., Farmer, R., et al. 2019, ApJ, 882,  
 2339 36, doi: [10.3847/1538-4357/ab3426](https://doi.org/10.3847/1538-4357/ab3426)
- 2340 Margalit, B., & Metzger, B. D. 2017, ApJL, 850, L19,  
 2341 doi: [10.3847/2041-8213/aa991c](https://doi.org/10.3847/2041-8213/aa991c)
- 2342 Marsh, T. R., Nelemans, G., & Steeghs, D. 2004, MNRAS,  
 2343 350, 113, doi: [10.1111/j.1365-2966.2004.07564.x](https://doi.org/10.1111/j.1365-2966.2004.07564.x)
- 2344 Massevitch, A., & Yungelson, L. 1975,  
 2345 Mem. Soc. Astron. Italiana, 46, 217
- 2346 McKernan, B., Ford, K. E. S., & O'Shaughnessy, R. 2020,  
 2347 MNRAS, 498, 4088, doi: [10.1093/mnras/staa2681](https://doi.org/10.1093/mnras/staa2681)
- 2348 McMillan, P. J. 2011, MNRAS, 414, 2446,  
 2349 doi: [10.1111/j.1365-2966.2011.18564.x](https://doi.org/10.1111/j.1365-2966.2011.18564.x)
- 2350 Metzger, B. D. 2017, Living Reviews in Relativity, 20, 3,  
 2351 doi: [10.1007/s41114-017-0006-z](https://doi.org/10.1007/s41114-017-0006-z)

- 2352 Miller, M. C., & Lauburg, V. M. 2009, ApJ, 692, 917,  
 2353 doi: [10.1088/0004-637X/692/1/917](https://doi.org/10.1088/0004-637X/692/1/917)
- 2354 Miller-Jones, J. C. A., Bahramian, A., Orosz, J. A., et al.  
 2355 2021, Science, 371, 1046, doi: [10.1126/science.abb3363](https://doi.org/10.1126/science.abb3363)
- 2356 Morris, M. 1993, ApJ, 408, 496, doi: [10.1086/172607](https://doi.org/10.1086/172607)
- 2357 Nandez, J. L. A., & Ivanova, N. 2016, MNRAS, 460, 3992,  
 2358 doi: [10.1093/mnras/stw1266](https://doi.org/10.1093/mnras/stw1266)
- 2359 Narayan, R., Piran, T., & Shemi, A. 1991, ApJL, 379, L17,  
 2360 doi: [10.1086/186143](https://doi.org/10.1086/186143)
- 2361 Neijssel, C. J., Vigna-Gómez, A., Stevenson, S., et al. 2019,  
 2362 MNRAS, 490, 3740, doi: [10.1093/mnras/stz2840](https://doi.org/10.1093/mnras/stz2840)
- 2363 Nelemans, G., Yungelson, L. R., & Portegies Zwart, S. F.  
 2364 2001, A&A, 375, 890, doi: [10.1051/0004-6361:20010683](https://doi.org/10.1051/0004-6361:20010683)
- 2365 Nishizawa, A., Berti, E., Klein, A., & Sesana, A. 2016,  
 2366 PhRvD, 94, 064020, doi: [10.1103/PhysRevD.94.064020](https://doi.org/10.1103/PhysRevD.94.064020)
- 2367 Nissanke, S., Vallisneri, M., Nelemans, G., & Prince, T. A.  
 2368 2012, ApJ, 758, 131, doi: [10.1088/0004-637X/758/2/131](https://doi.org/10.1088/0004-637X/758/2/131)
- 2369 Nomoto, K. 1984, ApJ, 277, 791, doi: [10.1086/161749](https://doi.org/10.1086/161749)
- 2370 —. 1987, ApJ, 322, 206, doi: [10.1086/165716](https://doi.org/10.1086/165716)
- 2371 Öpik, E. 1924, Publications of the Tartu Astrofizika  
 2372 Observatory, 25, 1
- 2373 Özel, F., Psaltis, D., Narayan, R., & McClintock, J. E.  
 2374 2010, ApJ, 725, 1918,  
 2375 doi: [10.1088/0004-637X/725/2/1918](https://doi.org/10.1088/0004-637X/725/2/1918)
- 2376 Paczyński, B., & Sienkiewicz, R. 1972, AcA, 22, 73
- 2377 Peters, P. C. 1964, Physical Review, 136, 1224,  
 2378 doi: [10.1103/PhysRev.136.B1224](https://doi.org/10.1103/PhysRev.136.B1224)
- 2379 Peters, P. C., & Mathews, J. 1963, Physical Review, 131,  
 2380 435, doi: [10.1103/PhysRev.131.435](https://doi.org/10.1103/PhysRev.131.435)
- 2381 Pfahl, E., Podsiadlowski, P., & Rappaport, S. 2005, ApJ,  
 2382 628, 343, doi: [10.1086/430515](https://doi.org/10.1086/430515)
- 2383 Pfahl, E., Rappaport, S., Podsiadlowski, P., & Spruit, H.  
 2384 2002, ApJ, 574, 364, doi: [10.1086/340794](https://doi.org/10.1086/340794)
- 2385 Podsiadlowski, P., Langer, N., Poelarends, A. J. T., et al.  
 2386 2004, ApJ, 612, 1044, doi: [10.1086/421713](https://doi.org/10.1086/421713)
- 2387 Pol, N., McLaughlin, M., & Lorimer, D. 2021, arXiv  
 2388 e-prints, arXiv:2109.04512.  
<https://arxiv.org/abs/2109.04512>
- 2389 Pols, O. R., Schröder, K.-P., Hurley, J. R., Tout, C. A., &  
 2390 Eggleton, P. P. 1998, MNRAS, 298, 525,  
 2391 doi: [10.1046/j.1365-8711.1998.01658.x](https://doi.org/10.1046/j.1365-8711.1998.01658.x)
- 2392 Portegies Zwart, S. F., & McMillan, S. L. W. 2000, ApJL,  
 2393 528, L17, doi: [10.1086/312422](https://doi.org/10.1086/312422)
- 2394 Rastello, S., Mapelli, M., Di Carlo, U. N., et al. 2020,  
 2395 MNRAS, 497, 1563, doi: [10.1093/mnras/staa2018](https://doi.org/10.1093/mnras/staa2018)
- 2396 Rastello, S., Mapelli, M., di Carlo, U. N., et al. 2021, arXiv  
 2397 e-prints, arXiv:2105.01669.  
<https://arxiv.org/abs/2105.01669>
- 2398 Renzo, M., Callister, T., Chatzioannou, K., et al. 2021,  
 2399 ApJ, 919, 128, doi: [10.3847/1538-4357/ac1110](https://doi.org/10.3847/1538-4357/ac1110)
- 2400 Robson, T., Cornish, N. J., & Liu, C. 2019, Classical and  
 2401 Quantum Gravity, 36, 105011,  
 2402 doi: [10.1088/1361-6382/ab1101](https://doi.org/10.1088/1361-6382/ab1101)
- 2403 Rodriguez, C. L., Amaro-Seoane, P., Chatterjee, S., &  
 2404 Rasio, F. A. 2018, PhRvL, 120, 151101,  
 2405 doi: [10.1103/PhysRevLett.120.151101](https://doi.org/10.1103/PhysRevLett.120.151101)
- 2406 Rodriguez, C. L., Morscher, M., Pattabiraman, B., et al.  
 2407 2015, PhRvL, 115, 051101,  
 2408 doi: [10.1103/PhysRevLett.115.051101](https://doi.org/10.1103/PhysRevLett.115.051101)
- 2409 Ruiter, A. J., Belczynski, K., Benacquista, M., Larson,  
 2410 S. L., & Williams, G. 2010, ApJ, 717, 1006,  
 2411 doi: [10.1088/0004-637X/717/2/1006](https://doi.org/10.1088/0004-637X/717/2/1006)
- 2412 Sana, H., de Mink, S. E., de Koter, A., et al. 2012, Science,  
 2413 337, 444, doi: [10.1126/science.1223344](https://doi.org/10.1126/science.1223344)
- 2414 Sander, A. A. C., & Vink, J. S. 2020, MNRAS, 499, 873,  
 2415 doi: [10.1093/mnras/staa2712](https://doi.org/10.1093/mnras/staa2712)
- 2416 Schneider, F. R. N., Izzard, R. G., Langer, N., & de Mink,  
 2417 S. E. 2015, ApJ, 805, 20
- 2418 Schreier, R., Hillel, S., Shiber, S., & Soker, N. 2021,  
 2419 MNRAS, 508, 2386, doi: [10.1093/mnras/stab2687](https://doi.org/10.1093/mnras/stab2687)
- 2420 Schuster, E. F. 1985, Communications in Statistics-theory  
 2421 and Methods, 14, 1123
- 2422 Sellwood, J. A., & Binney, J. J. 2002, MNRAS, 336, 785,  
 2423 doi: [10.1046/j.1365-8711.2002.05806.x](https://doi.org/10.1046/j.1365-8711.2002.05806.x)
- 2424 Sesana, A. 2016, PhRvL, 116, 231102,  
 2425 doi: [10.1103/PhysRevLett.116.231102](https://doi.org/10.1103/PhysRevLett.116.231102)
- 2426 Sesana, A., Lamberts, A., & Petiteau, A. 2020, MNRAS,  
 2427 494, L75, doi: [10.1093/mnrasl/slaa039](https://doi.org/10.1093/mnrasl/slaa039)
- 2428 Shao, Y., & Li, X.-D. 2021, arXiv e-prints,  
 2429 arXiv:2107.03565. <https://arxiv.org/abs/2107.03565>
- 2430 Sharma, S., Hayden, M. R., & Bland-Hawthorn, J. 2020,  
 2431 arXiv e-prints, arXiv:2005.03646.  
<https://arxiv.org/abs/2005.03646>
- 2432 Shenar, T., Bodensteiner, J., Abdul-Masih, M., et al. 2020,  
 2433 A&A, 639, L6, doi: [10.1051/0004-6361/202038275](https://doi.org/10.1051/0004-6361/202038275)
- 2434 Shenar, T., Sablowski, D. P., Hainich, R., et al. 2019, A&A,  
 2435 627, A151, doi: [10.1051/0004-6361/201935684](https://doi.org/10.1051/0004-6361/201935684)
- 2436 Sigurdsson, S., & Hernquist, L. 1993, Nature, 364, 423,  
 2437 doi: [10.1038/364423a0](https://doi.org/10.1038/364423a0)
- 2438 Silsbee, K., & Tremaine, S. 2017, ApJ, 836, 39,  
 2439 doi: [10.3847/1538-4357/aa5729](https://doi.org/10.3847/1538-4357/aa5729)
- 2440 Smarr, L. L., & Blandford, R. 1976, ApJ, 207, 574,  
 2441 doi: [10.1086/154524](https://doi.org/10.1086/154524)
- 2442 Smits, R., Kramer, M., Stappers, B., et al. 2009, A&A, 493,  
 2443 1161, doi: [10.1051/0004-6361:200810383](https://doi.org/10.1051/0004-6361:200810383)
- 2444 Snaith, O. N., Haywood, M., Di Matteo, P., et al. 2014,  
 2445 ApJL, 781, L31, doi: [10.1088/2041-8205/781/2/L31](https://doi.org/10.1088/2041-8205/781/2/L31)
- 2446 Soberman, G. E., Phinney, E. S., & van den Heuvel,  
 2447 E. P. J. 1997, A&A, 327, 620.  
<https://arxiv.org/abs/astro-ph/9703016>

- 2452 Srinivasan, G. 1989, A&A Rv, 1, 209,  
2453 doi: [10.1007/BF00873079](https://doi.org/10.1007/BF00873079)
- 2454 Stephan, A. P., Naoz, S., Ghez, A. M., et al. 2016,  
2455 MNRAS, 460, 3494, doi: [10.1093/mnras/stw1220](https://doi.org/10.1093/mnras/stw1220)
- 2456 Stevenson, S., Sampson, M., Powell, J., et al. 2019, ApJ,  
2457 882, 121, doi: [10.3847/1538-4357/ab3981](https://doi.org/10.3847/1538-4357/ab3981)
- 2458 Stevenson, S., Vigna-Gómez, A., Mandel, I., et al. 2017,  
2459 Nature Communications, 8, 14906,  
2460 doi: [10.1038/ncomms14906](https://doi.org/10.1038/ncomms14906)
- 2461 Storck, A., & Church, R. 2022, arXiv e-prints,  
2462 arXiv:2205.01507. <https://arxiv.org/abs/2205.01507>
- 2463 Taam, R. E., & Sandquist, E. L. 2000, ARA&A, 38, 113,  
2464 doi: [10.1146/annurev.astro.38.1.113](https://doi.org/10.1146/annurev.astro.38.1.113)
- 2465 Takahashi, R., & Seto, N. 2002, ApJ, 575, 1030,  
2466 doi: [10.1086/341483](https://doi.org/10.1086/341483)
- 2467 Tamanini, N., & Danielski, C. 2019, Nature Astronomy, 3,  
2468 858, doi: [10.1038/s41550-019-0807-y](https://doi.org/10.1038/s41550-019-0807-y)
- 2469 Tauris, T. M., Kramer, M., Freire, P. C. C., et al. 2017,  
2470 ApJ, 846, 170, doi: [10.3847/1538-4357/aa7e89](https://doi.org/10.3847/1538-4357/aa7e89)
- 2471 Tauris, T. M., Langer, N., Moriya, T. J., et al. 2013, ApJL,  
2472 778, L23, doi: [10.1088/2041-8205/778/2/L23](https://doi.org/10.1088/2041-8205/778/2/L23)
- 2473 Tauris, T. M., Langer, N., & Podsiadlowski, P. 2015,  
2474 MNRAS, 451, 2123, doi: [10.1093/mnras/stv990](https://doi.org/10.1093/mnras/stv990)
- 2475 Team COMPAS: J. Riley, Riley, J., Agrawal, P., et al.  
2476 2021, arXiv e-prints, arXiv:2109.10352.  
<https://arxiv.org/abs/2109.10352>
- 2477 The LIGO Scientific Collaboration, the Virgo  
2478 Collaboration, Abbott, R., et al. 2021a, arXiv e-prints,  
2479 arXiv:2108.01045. <https://arxiv.org/abs/2108.01045>
- 2481 The LIGO Scientific Collaboration, the Virgo  
2482 Collaboration, the KAGRA Collaboration, et al. 2021b,  
2483 arXiv e-prints, arXiv:2106.15163.  
<https://arxiv.org/abs/2106.15163>
- 2485 The LIGO Scientific Collaboration, The Virgo  
2486 Collaboration, & The KAGRA Scientific Collaboration.  
2487 2021c, arXiv e-prints, arXiv:2111.03634.  
<https://arxiv.org/abs/2111.03634>
- 2489 Thrane, E., Osłowski, S., & Lasky, P. D. 2020, MNRAS,  
2490 493, 5408, doi: [10.1093/mnras/staa593](https://doi.org/10.1093/mnras/staa593)
- 2491 Timmes, F. X., Woosley, S. E., & Weaver, T. A. 1996, ApJ,  
2492 457, 834, doi: [10.1086/176778](https://doi.org/10.1086/176778)
- 2493 Tiwari, V. 2022, ApJ, 928, 155,  
2494 doi: [10.3847/1538-4357/ac589a](https://doi.org/10.3847/1538-4357/ac589a)
- 2495 Toonen, S., Claeys, J. S. W., Mennekens, N., & Ruiter,  
2496 A. J. 2014, A&A, 562, A14,  
2497 doi: [10.1051/0004-6361/201321576](https://doi.org/10.1051/0004-6361/201321576)
- 2498 Toonen, S., Portegies Zwart, S., Hamers, A. S., &  
2499 Bandopadhyay, D. 2020, A&A, 640, A16,  
2500 doi: [10.1051/0004-6361/201936835](https://doi.org/10.1051/0004-6361/201936835)
- 2501 Tout, C. A., Pols, O. R., Eggleton, P. P., & Han, Z. 1996,  
2502 MNRAS, 281, 257, doi: [10.1093/mnras/281.1.257](https://doi.org/10.1093/mnras/281.1.257)
- 2503 Tutukov, A., & Yungelson, L. 1973, Nauchnye Informatsii,  
2504 27, 70
- 2505 Tutukov, A. V., & Yungelson, L. R. 1993, MNRAS, 260,  
2506 675, doi: [10.1093/mnras/260.3.675](https://doi.org/10.1093/mnras/260.3.675)
- 2507 van den Heuvel, E. P. J. 2011, Compact stars and the  
2508 evolution of binary systems (World Scientific Publishing  
2509 Co. Pte. Ltd), 55–73, doi: [10.1142/9789814374774\\_0006](https://doi.org/10.1142/9789814374774_0006)
- 2510 van den Heuvel, E. P. J., Portegies Zwart, S. F., & de  
2511 Mink, S. E. 2017, MNRAS, 471, 4256,  
2512 doi: [10.1093/mnras/stx1430](https://doi.org/10.1093/mnras/stx1430)
- 2513 van Son, L. A. C., de Mink, S. E., Callister, T., et al. 2021,  
2514 arXiv e-prints, arXiv:2110.01634.  
<https://arxiv.org/abs/2110.01634>
- 2515 van Son, L. A. C., De Mink, S. E., Broekgaarden, F. S.,  
2516 et al. 2020, ApJ, 897, 100
- 2518 Veske, D., Bartos, I., M'arka, Z., & M'arka, S. 2021, ApJ,  
2519 922, 258, doi: [10.3847/1538-4357/ac27ac](https://doi.org/10.3847/1538-4357/ac27ac)
- 2520 Vigna-Gómez, A., Neijssel, C. J., Stevenson, S., et al. 2018,  
2521 MNRAS, 481, 4009, doi: [10.1093/mnras/sty2463](https://doi.org/10.1093/mnras/sty2463)
- 2522 Vink, J. S. 2017, A&A, 607, L8,  
2523 doi: [10.1051/0004-6361/201731902](https://doi.org/10.1051/0004-6361/201731902)
- 2524 Vink, J. S., & de Koter, A. 2005, A&A, 442, 587,  
2525 doi: [10.1051/0004-6361:20052862](https://doi.org/10.1051/0004-6361:20052862)
- 2526 Vink, J. S., de Koter, A., & Lamers, H. J. G. L. M. 2000,  
2527 A&A, 362, 295. <https://arxiv.org/abs/astro-ph/0008183>
- 2528 —. 2001, A&A, 369, 574, doi: [10.1051/0004-6361:20010127](https://doi.org/10.1051/0004-6361:20010127)
- 2529 Virtanen, P., Gommers, R., Oliphant, T. E., et al. 2020,  
2530 Nature Methods, 17, 261, doi: [10.1038/s41592-019-0686-2](https://doi.org/10.1038/s41592-019-0686-2)
- 2531 Vynatheya, P., & Hamers, A. S. 2021, arXiv e-prints,  
2532 arXiv:2110.14680
- 2533 Wagg, T., Breivik, K., & de Mink, S. E. 2021, arXiv  
2534 e-prints, arXiv:2111.08717.  
<https://arxiv.org/abs/2111.08717>
- 2536 Wagg, T., Broekgaarden, F., de Mink, S., et al. 2021,  
2537 Dataset from: Gravitational wave sources in our Galactic  
2538 backyard - Predictions for BHBH, BHNS and NSNS  
2539 binaries in LISA, 0.0.1, Zenodo,  
2540 doi: [10.5281/zenodo.5725607](https://doi.org/10.5281/zenodo.5725607)
- 2541 Waskom, M. 2021, The Journal of Open Source Software, 6,  
2542 3021, doi: [10.21105/joss.03021](https://doi.org/10.21105/joss.03021)
- 2543 Webbink, R. F. 1984, ApJ, 277, 355, doi: [10.1086/161701](https://doi.org/10.1086/161701)
- 2544 Webster, B. L., & Murdin, P. 1972, Nature, 235, 37,  
2545 doi: [10.1038/235037a0](https://doi.org/10.1038/235037a0)
- 2546 Wegg, C., Gerhard, O., & Portail, M. 2015, MNRAS, 450,  
2547 4050, doi: [10.1093/mnras/stv745](https://doi.org/10.1093/mnras/stv745)
- 2548 Willems, B., Kalogera, V., Vecchio, A., et al. 2007, ApJL,  
2549 665, L59, doi: [10.1086/521049](https://doi.org/10.1086/521049)

- 2550 Woosley, S. E., Blinnikov, S., & Heger, A. 2007, Nature,  
2551 450, 390, doi: [10.1038/nature06333](https://doi.org/10.1038/nature06333)
- 2552 Xu, X.-J., & Li, X.-D. 2010a, ApJ, 716, 114,  
2553 doi: [10.1088/0004-637X/716/1/114](https://doi.org/10.1088/0004-637X/716/1/114)
- 2554 —. 2010b, ApJ, 722, 1985,  
2555 doi: [10.1088/0004-637X/722/2/1985](https://doi.org/10.1088/0004-637X/722/2/1985)
- 2556 Ye, C., & Fishbach, M. 2022, arXiv e-prints,  
2557 arXiv:2202.05164. <https://arxiv.org/abs/2202.05164>
- 2558 Yu, S., & Jeffery, C. S. 2010, A&A, 521, A85,  
2559 doi: [10.1051/0004-6361/201014827](https://doi.org/10.1051/0004-6361/201014827)
- 2560 Zapartas, E., de Mink, S. E., Izzard, R. G., et al. 2017,  
2561 A&A, 601, A29, doi: [10.1051/0004-6361/201629685](https://doi.org/10.1051/0004-6361/201629685)
- 2562 Ziosi, B. M., Mapelli, M., Branchesi, M., & Tormen, G.  
2563 2014, MNRAS, 441, 3703, doi: [10.1093/mnras/stu824](https://doi.org/10.1093/mnras/stu824)

2564

## APPENDIX

2565

## A. POPULATION SYNTHESIS

2566 In this section we summarise the main assumptions  
 2567 and settings from the population synthesis simulation  
 2568 from Broekgaarden et al. (2021a,b).

2569

## A.1. Initial conditions

2570 Broekgaarden et al. (2021a,b) simulate between 1 and  
 2571 100 million massive binaries for each of 50 metallicities  
 2572 equally spaced in log space between  $Z \in [0.0001, 0.022]$ ,  
 2573 where  $Z$  is the mass fraction of heavy elements. They  
 2574 simulate more binaries for higher metallicities so that  
 2575 large enough sample of DCOs at each metallicity (since  
 2576 DCOs are formed at a lower rate at higher metallicities).  
 2577 These metallicities span the allowed metallicity range for  
 2578 the original fitting formulae on which COMPAS is based  
 2579 (Hurley et al. 2000). This is repeated for 19 physics  
 2580 variations (see Section A.3) and so in total over two  
 2581 billion binaries were simulated.

2582 Each binary is sampled from initial distributions for  
 2583 the primary and secondary masses as well as the separation.  
 2584 The primary mass, that is the mass of the initially  
 2585 more massive star, is restricted to  $m_1 \in [5, 150] M_\odot$ ,  
 2586 which spans the range of interest for NS and BH for-  
 2587 mation in binary systems, and drawn from the Kroupa  
 2588 (2001) initial mass function (IMF),  $p(m_1) \propto m_1^{-2.3}$ . The  
 2589 secondary mass,  $m_2$ , is drawn using the initial mass  
 2590 ratio of the binary,  $q \equiv m_2/m_1$ , which Broekgaarden  
 2591 et al. (2021a,b) assume to be uniform on  $[0, 1]$ , therefore  
 2592  $p(q) = 1$  (e.g. consistent with Sana et al. 2012). They  
 2593 additionally restrict the secondary masses  $m_2 \geq 0.1 M_\odot$ ,  
 2594 which is approximately the minimum mass for a main  
 2595 sequence star. They assume that the initial separation  
 2596 follows a flat in the log distribution with  $p(a_i) \propto 1/a_i$   
 2597 and  $a_i \in [0.01, 1000] \text{ AU}$  (Öpik 1924; Abt 1983). They  
 2598 assume that all binary orbits are circular at birth to re-  
 2599 duce the dimensions of initial parameters. Since they  
 2600 focus on post-interaction binaries which will have cir-  
 2601 cularised after mass transfer they argue this is a rea-  
 2602 sonable assumption (as many studies have in the past)  
 2603 and is likely not critical for predicting detection rates  
 2604 (Hurley et al. 2002; de Mink & Belczynski 2015).

2605 Broekgaarden et al. (2021a,b) apply the adaptive im-  
 2606 portance sampling algorithm STROOPWAFEL (Broek-  
 2607 gaarden et al. 2019) to improve the yield of their sample.  
 2608 This algorithm increases the prevalence of target DCOs  
 2609 (BHBHs, BHNSs and NSNSs in this case) in the sample  
 2610 and assigns each a weight,  $w$ , which represents the prob-  
 2611 ability of drawing the DCO without STROOPWAFEL  
 2612 in effect.

## 2613 A.2. Physical assumptions in the fiducial model

2614 *Stellar Evolution:* To follow the evolution of mas-  
 2615 sive stars, COMPAS relies on fitting formulae by Hurley  
 2616 et al. (2000) to detailed single star models by Pols et al.  
 2617 (1998). COMPAS models the evolution of stars that lose  
 2618 or gain mass closely following the algorithms originally  
 2619 described in Tout et al. (1996) and Hurley et al. (2002).  
 2620 *Wind mass loss:* Broekgaarden et al. (2021a,b) fol-  
 2621 low the wind prescription from Belczynski et al. (2008),  
 2622 which was based on results from Monte Carlo radiative  
 2623 transfer simulation of Vink et al. (2000, 2001). They use  
 2624 the wind mass loss rates from Vink et al. (2001) for stars  
 2625 above 12500 K and the rates from Hurley et al. (2000) for  
 2626 cooler stars. Additionally, they use a separate, higher  
 2627 wind mass loss rate for luminous blue variable (LBV)  
 2628 stars, following Belczynski et al. (2008), to mimic ob-  
 2629 served LBV eruptions for stars with luminosities and  
 2630 effective temperatures above the Humphreys-Davidson  
 2631 limit. They use the Wolf-Rayet-like mass loss rate from  
 2632 Hamann & Koesterke (1998) with an additional metal-  
 2633 licity scaling from Vink & de Koter (2005) for helium  
 2634 stars, and set  $f_{\text{WR}} = 1$ . See Team COMPAS: J. Riley  
 2635 et al. (2021), Section 3 for the explicit equations.

2636 *Mass Transfer:* In determining the stability of mass  
 2637 transfer Broekgaarden et al. (2021a,b) use the  $\zeta$ -  
 2638 prescription, which compares the radial response of the  
 2639 star with the response of the Roche lobe radius to the  
 2640 mass transfer (e.g. Hjellming & Webbink 1987). The  
 2641 mass transfer efficiency,  $\beta \equiv \Delta M_{\text{acc}}/\Delta M_{\text{don}}$ , is the frac-  
 2642 tion of the mass transferred by the donor that is actu-  
 2643 ally accreted by the accretor. They limit the maximum  
 2644 accretion rate for stars to  $\Delta M_{\text{acc}}/\Delta t \leq 10M_{\text{acc}}/\tau_{\text{KH}}$ ,  
 2645 where  $\tau_{\text{KH}}$  is the Kelvin-Helmholtz timescale of the star  
 2646 (Paczyński & Sienkiewicz 1972; Hurley et al. 2002). The  
 2647 maximum accretion rate for compact objects is limited  
 2648 to the Eddington accretion rate. If more mass than  
 2649 these rates is accreted then they assume that the ex-  
 2650 cess is lost through isotropic re-emission in the vicinity  
 2651 of the accreting star (e.g. Massevitch & Yungelson 1975;  
 2652 Soberman et al. 1997). They assume that all mass trans-  
 2653 fer from a stripped post-helium-burning-star (case BB)  
 2654 onto a neutron star or black hole is unstable (Tauris  
 2655 et al. 2015).

2656 *Common-Envelope:* A common-envelope phase fol-  
 2657 lows dynamically unstable mass transfer and Broekgaar-  
 2658 den et al. (2021a,b) parameterise this using the  $\alpha$ - $\lambda$   
 2659 prescription from Webbink (1984) and de Kool (1990).  
 2660 They assume  $\alpha = 1$ , such that all of the gravitational

binding energy is available for the ejection of the envelope. For  $\lambda$  they use the fitting formulae from Xu & Li (2010a,b). They assume that any Hertzsprung gap donor stars that initiate a common-envelope phase will not survive this phase due to a lack of a steep density gradient between the core and envelope (Taam & Sandquist 2000; Ivanova & Taam 2004; Klencki et al. 2021). This follows the ‘pessimistic’ common-envelope scenario (c.f. Belczynski et al. 2007). They remove any binaries where the secondary immediately fills its Roche lobe upon the conclusion of the common-envelope phase as they treat these as failed common-envelope ejections, likely leading to a stellar merger.

*Supernovae:* Broekgaarden et al. (2021a,b) draw the remnant masses and natal kick magnitudes from different distributions depending on the type of supernova that occurs. For stars undergoing a general core-collapse supernova, they use the *delayed* supernova remnant mass prescription from Fryer et al. (2012). The *delayed* prescription does not reproduce a neutron star black hole mass gap and they use this as their default as it has been shown to provide a better fit for observed populations of DCOs (e.g. Vigna-Gómez et al. 2018). They draw the natal kick magnitudes from a Maxwellian velocity distribution with a one-dimensional root-mean-square velocity dispersion of  $\sigma_{\text{rms}}^{\text{1D}} = 265 \text{ km s}^{-1}$  (Lyne & Lorimer 1994; Hobbs et al. 2005). They assume that stars with helium core masses between  $1.6\text{--}2.25 M_{\odot}$  (Hurley et al. 2002) experience electron-capture supernovae (ECSN) (Nomoto 1984, 1987; Ivanova et al. 2008). They set all remnant masses to  $1.26 M_{\odot}$  in this case as an approximation of the solution to Equation 8 of Timmes et al. (1996). For these supernovae, they set  $\sigma_{\text{rms}}^{\text{1D}} = 30 \text{ km s}^{-1}$  (e.g. Pfahl et al. 2002; Podsiadlowski et al. 2004). They assume that stars that undergo case BB mass transfer (Dewi et al. 2002) experience extreme stripping which leads to an ultra-stripped supernova (Tauris et al. 2013, 2015). For these supernovae they calculate the remnant mass using the Fryer et al. (2012) prescription and use  $\sigma_{\text{rms}}^{\text{1D}} = 30 \text{ km s}^{-1}$  (as with ECSN). Stars with final helium core masses between  $35\text{--}135 M_{\odot}$  are presumed to undergo a pair-instability, or pulsational pair-instability supernova (e.g. Woosley et al. 2007; Farmer et al. 2019). They follow the prescription from Marchant et al. (2019) as implemented in (Stevenson et al. 2019) for these supernovae. They assume that kicks are isotropic in the frame of the collapsing star. They adopt a maximum neutron star mass of  $2.5 M_{\odot}$  (e.g. Kalogera & Baym 1996; Fryer et al. 2015; Margalit & Metzger 2017) for the fiducial model and change the Fryer et al. (2012) prescription accordingly.

### A.3. Model variations

In addition to their fiducial model for the formation of DCOs, Broekgaarden et al. (2021a,b) explore 19 other models in which they change various aspects of the mass transfer, common-envelope, supernova and wind mass loss physics assumptions in order to assess the effect of their uncertainties on the overall double compact object detection rates and distributions. Each of the models varies a single physics assumption (fiducial assumptions are outlined in Section A.2) and these models are outlined in Table A1.

Their fiducial model is labelled model A. Models B-D focus on changes to the mass transfer physics assumptions. They explore the effect of fixing the mass transfer efficiency  $\beta$  to a constant value, rather than allowing it to vary based on the maximum accretion rate. In models B, C, D, in which they set the value of  $\beta$  to 0.25, 0.5 and 0.75 respectively.

Models E'-K focus on altering the common-envelope physics. In model E' we modify model E from Broekgaarden et al. (2021a,b) to investigate the consequence of assuming that case BB mass transfer is always unstable, whilst allowing Helium HG donors to survive CE events. They change the common-envelope efficiency parameter to  $\alpha_{\text{CE}} = 0.1, 0.5, 2.0, 10.0$  in models G, H, I and J respectively. In model K, they relax their restriction that Hertzsprung gap donor stars cannot survive common-envelope events, thereby following the ‘optimistic’ common-envelope scenario. They combine this with model E' in model F.

In models L-R they consider changes related to their assumptions about supernova physics. Model L uses the alternate *rapid* remnant mass prescription from Fryer et al. (2012) instead of the *delayed* prescription. They change the maximum neutron star mass in models M and N to 2 and  $3 M_{\odot}$  respectively to account for the range of predicted maximum neutron star masses. Model O removes the implementation of pair-instability and pulsational pair-instability supernovae. In models P and Q they decrease the root-mean-square velocity dispersion for core-collapse supernovae to explore the effect of lower kicks. Model R removes the natal kick for all black holes.

Finally, in models S-T Broekgaarden et al. (2021a,b) investigate the effect of changing their assumption about wind mass loss rates, specifically for Wolf-Rayet winds. They vary  $f_{\text{WR}}$  to 0.1 and 5.0 in models S and T respectively. These values approximately span the current range of possible Wolf-Rayet wind efficiencies suggested from observations (e.g. Vink 2017; Hamann et al. 2019; Shenar et al. 2019; Miller-Jones et al. 2021; van Son et al. 2021).

Model	Physics Variation
A	Fiducial (see Section A.2)
B	Fixed mass transfer efficiency of $\beta = 0.25$
C	Fixed mass transfer efficiency of $\beta = 0.5$
D	Fixed mass transfer efficiency of $\beta = 0.75$
E'	Case BB mass transfer always unstable
F	Case BB always unstable + Optimistic CE
G	CE efficiency parameter $\alpha = 0.1$
H	CE efficiency parameter $\alpha = 0.5$
I	CE efficiency parameter $\alpha = 2$
J	CE efficiency parameter $\alpha = 10$
K	HG donor stars initiating a CE survive CE
L	Fryer rapid SN remnant mass prescription
M	Maximum NS mass is fixed to $2 M_{\odot}$
N	Maximum NS mass is fixed to $3 M_{\odot}$
O	PISN and pulsational-PISN not implemented
P	$\sigma_{\text{rms}}^{\text{1D}} = 100 \text{ km s}^{-1}$ for core-collapse supernova
Q	$\sigma_{\text{rms}}^{\text{1D}} = 30 \text{ km s}^{-1}$ for core-collapse supernova
R	Black holes receive no natal kick
S	Wolf-Rayet wind factor $f_{\text{WR}} = 0.1$
T	Wolf-Rayet wind factor $f_{\text{WR}} = 5.0$

**Table A1.** A description of the 20 binary population synthesis models used in this study. A is the fiducial model, B-D change mass transfer physics, E'-K change common-envelope physics, L-R change supernova physics and S-T change wind mass loss (c.f. Broekgaarden et al. 2021a, Table 2).

2764

## B. DETECTION RATE NORMALISATION

In this section we explain the normalisation process that we refer to in Section 2.3. From each simulated instance of the Milky Way we extract the fraction of targets that are detectable, where we define a target as one of BHBH, BHNS or NSNS that merges in a Hubble time. To convert the detectable fraction to a detection rate for the Milky Way, we write that the *number* of detectable targets in the Milky Way is

$$N_{\text{detect}} = f_{\text{detect}} \cdot N_{\text{target,MW}}, \quad (\text{B1})$$

where  $f_{\text{detect}}$  is the fraction of targets in the instance that were detectable and  $N_{\text{target,MW}}$  is the total number of targets that have been formed in the Milky Way's history. We can further break this total down into

$$N_{\text{target,MW}} = \langle \mathcal{R}_{\text{target}} \rangle \cdot M_{\text{SF,MW}}, \quad (\text{B2})$$

2765 where  $\langle \mathcal{R}_{\text{target}} \rangle$  is the average number of targets formed  
2766 per star forming mass and  $M_{\text{SF,MW}}$  is the star forming  
2767 mass of the Milky Way, meaning the total mass of every  
2768 star ever formed in the Milky Way.

### B.1. Average target formation rate

Double compact object formation is metallicity dependent, so we find the average rate as the integral over metallicity, which is given by

$$\langle \mathcal{R}_{\text{target}} \rangle = \int_{Z_{\min}}^{Z_{\max}} p_Z \mathcal{R}_{\text{target,Z}} dZ, \quad (\text{B3})$$

where  $Z_{\min}, Z_{\max}$  are the minimum and maximum sampled metallicities,  $p_Z$  is the probability of forming a star at the metallicity  $Z$  (which can be found using the distribution in Frankel et al. 2018) and  $\mathcal{R}_{\text{target,Z}}$  is the number of targets formed per star forming mass,

$$\mathcal{R}_{\text{target,Z}} = \frac{N_{\text{target,Z}}}{M_{\text{SF,Z}}}. \quad (\text{B4})$$

In practice, this integral is instead approximated as a sum over the metallicity bins that we use in our simulation. The number of targets in our sample at a metallicity  $Z$ ,  $N_{\text{target,Z}}$ , can be written simply as the sum of the targets' weights:

$$N_{\text{target,Z}} = \sum_{i=1}^{N_{\text{binaries,Z}}} w_i \theta_{\text{target,i}}, \quad (\text{B5})$$

2770 where  $w_i$  is the binary's adaptive importance sampling  
2771 weight assigned,  $N_{\text{binaries,Z}}$  is the number of binaries at  
2772 metallicity  $Z$  in our sample and  $\theta_{\text{target,i}}$  is only 1 when  
2773 the binary is a target and otherwise 0.

The total star forming mass at a metallicity  $Z$ ,  $M_{\text{SF,Z}}$ , can be written as

$$M_{\text{SF,Z}} = \frac{\langle m \rangle_{\text{COMPAS,Z}}}{f_{\text{trunc}}} N_{\text{binaries,Z}}, \quad (\text{B6})$$

2774 where  $\langle m \rangle_{\text{COMPAS}}$  is the average star forming mass of  
2775 a binary in a simulation using our cutoffs (discussed  
2776 in Section 2.1) and  $f_{\text{trunc}}$  is the fraction of the total  
2777 stellar mass from which our COMPAS simulations sam-  
2778 ple, given our truncated mass and separation ranges  
2779 (see Section 2.1). These truncations mean that only  
2780  $f_{\text{trunc}} \approx 0.17$  of the stellar mass in the galaxy is sam-  
2781 pled from.

### B.2. Total star forming mass in the Milky Way

2783 It is important to distinguish between the *total* mass  
2784 of every star formed over the entire history of the Milky  
2785 Way and the *current* stellar mass in the Milky Way.  
2786 Many stars born in the Milky Way are no longer living  
2787 and have lost much of their mass to stellar winds and  
2788 supernovae, thus the current stellar mass in the Milky  
2789 Way is an underestimate of the total star forming mass.

Licquia & Newman (2015) find that the total stellar mass today in the Milky Way is  $6.08 \pm 1.14 \times 10^{10} M_{\odot}$ .

This total includes all stars and stellar remnants (white dwarfs, neutrons stars and black holes) but *excludes* brown dwarfs. We can write that the total mass of every star every formed in the Milky Way is

$$M_{\text{SF,MW}} = (6.08 \pm 1.14) \times 10^{10} M_{\odot} \cdot \frac{\langle m \rangle_{\text{SF,total}}}{\langle m \rangle_{\text{SF,today}}}, \quad (\text{B7})$$

where  $\langle m \rangle_{\text{SF,total}}$  is the average mass of a star over the history of the Milky Way and is defined as

$$\langle m \rangle_{\text{SF,total}} = \int_0^{t_{\text{MW}}} p_{\text{birth}}(\tau) \int_{0.01}^{200} \zeta(m) m dm d\tau, \quad (\text{B8})$$

where  $t_{\text{MW}}$  is the age of the Milky Way,  $\zeta(m)$  is the Kroupa (2001) IMF function and  $p_{\text{birth}}(\tau)$  is the probability of a star being formed at a lookback time  $\tau$  (Eq. 2).  $\langle m \rangle_{\text{SF,today}}$  is the average mass of all stars and stellar remnants (excluding brown dwarfs) present in the Milky Way today is defined as follows (note that we integrate from 0.08 not 0.01 since observations of today's Milky Way mass exclude brown dwarfs)

$$\langle m \rangle_{\text{SF,today}} = \int_0^{t_{\text{MW}}} p_{\text{birth}}(\tau) \int_{0.08}^{200} \zeta(m) m_{\text{today}} dm d\tau, \quad (\text{B9})$$

where  $m_{\text{today}}(m, Z, \tau)$  is the current mass of a star that was formed  $\tau$  years ago at a metallicity  $Z$ . We calculate  $m_{\text{today}}(m, Z, \tau)$  by interpolating the final masses given by COMPAS for a grid of single stars over different masses and metallicities using the Fryer et al. (2012) delayed prescription and default wind mass loss settings. For  $Z$ , we use the average star forming metallicity in the Milky Way at a lookback time  $\tau$  using our galaxy model. Evaluating Equation B7, we find that the total mass of every star that has ever formed in the Milky Way is

$$\begin{aligned} M_{\text{SF,MW}} &= (6.1 \pm 1.1) \times 10^{10} M_{\odot} \cdot \frac{0.378 M_{\odot}}{0.221 M_{\odot}}, \\ &= (10.4 \pm 1.1) \times 10^{10} M_{\odot}, \end{aligned} \quad (\text{B10})$$

an increase of approximately 70% from the value still in stars today!

### B.3. Normalisation summary

Finally, we can substitute Equations B3 and B7 into B1 and write that the overall normalisation of the detection rate is calculated as

$$\begin{aligned} N_{\text{detect}} &= f_{\text{detect}} \cdot 10.4 \times 10^{10} M_{\odot} \\ &\times \sum_{Z=Z_{\min}}^{Z_{\max}} p_Z \left( \sum_{i=1}^{N_{\text{binaries},Z}} w_i \theta_{\text{target},i} \right) \\ &\times \left( \frac{\langle m \rangle_{\text{COMPAS},Z}}{f_{\text{trunc}}} \sum_{i=1}^{N_{\text{binaries},Z}} w_i \right)^{-1}. \end{aligned} \quad (\text{B11})$$

## C. CALCULATION OF THE UNCERTAINTIES IN THE CHIRP MASS FOR DETECTABLE SOURCES

How accurately the chirp mass of a detected binary can be determined depends on the signal to noise ratio, duration of the mission, its orbital frequency and the time derivative of the orbital frequency.

Here we describe how we estimate the uncertainty of the chirp mass. First, consider the chirp mass, which can be expressed as

$$\mathcal{M}_c = \frac{c^3}{G} \left( \frac{5\pi}{48n} \frac{\dot{f}_n}{F(e)} \right)^{3/5} \frac{1}{(2\pi f_{\text{orb}})^{11/5}}, \quad (\text{C1})$$

where  $f_n$  is the frequency of the n-th harmonic,  $f_{\text{orb}}$  is the orbital frequency,  $\mathcal{M}_c$  is the chirp mass (defined in Eq. 12),  $e$  is the eccentricity and

$$F(e) = \frac{1 + \frac{73}{24}e^2 + \frac{37}{96}e^4}{(1 - e^2)^{7/2}}, \quad (\text{C2})$$

is the enhancement factor of gravitational wave emission for an eccentric binary over an otherwise identical circular binary (Peters & Mathews 1963, Eq. 17). In practice, we will use the dominating harmonic, with  $n = n_{\text{dom}}$  and  $f_n = n_{\text{dom}} f_{\text{orb}} = f_{\text{dom}}$ . The dominating harmonic for circular binaries is  $n_{\text{dom}} = 2$  and so the dominating frequency is twice the orbital frequency.

Therefore the chirp mass uncertainty can be estimated as

$$\frac{\Delta \mathcal{M}_c}{\mathcal{M}_c} = \frac{11}{5} \frac{\Delta f_{\text{orb}}}{f_{\text{orb}}} + \frac{3}{5} \frac{\Delta \dot{f}_{\text{dom}}}{\dot{f}_{\text{dom}}} + \frac{3}{5} \frac{\Delta F(e)}{F(e)}, \quad (\text{C3})$$

We estimate the frequency uncertainties using Takahashi & Seto (2002), such that

$$\frac{\Delta f_{\text{orb}}}{f_{\text{orb}}} = 4\sqrt{3} \cdot \frac{1}{\rho} \frac{1}{T_{\text{obs}}} \frac{1}{f_{\text{orb}}}, \quad (\text{C4})$$

$$\frac{\Delta \dot{f}_{\text{dom}}}{\dot{f}_{\text{dom}}} = 6\sqrt{5} \cdot \frac{1}{\rho} \left( \frac{1}{T_{\text{obs}}} \right)^2 \frac{1}{\dot{f}_{\text{dom}}}, \quad (\text{C5})$$

where  $\rho$  is the signal-to-noise ratio and  $T_{\text{obs}}$  is the LISA mission length. We estimate the eccentricity uncertainty,  $\Delta e$ , following the methods of Lau et al. (2020) and Korol & Safarzadeh (2021), which use the relative SNRs of different harmonics to work out the eccentricity. We propagate this uncertainty such that

$$\frac{\Delta F(e)}{F(e)} = \Delta e \cdot \frac{(1256 + 1608e^2 + 111e^4)e}{96 + 196e^2 - 255e^4 - 37e^6}. \quad (\text{C6})$$

We use Eq. C3 to calculate the chirp mass uncertainty for each DCO type in our sample and plot it in Fig. 6.

2809    D. ASSESSING THE IMPACT OF MILKY WAY  
 2810    MODEL CHOICES

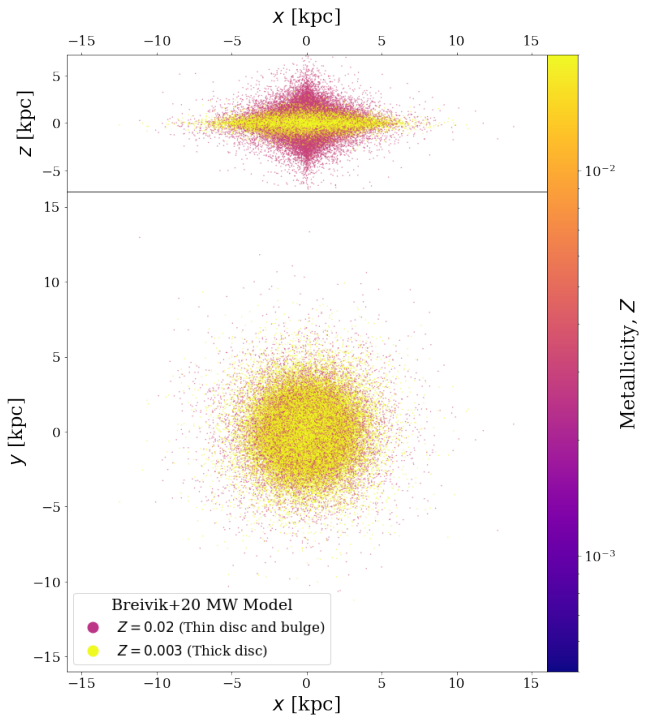
2811    The model that we use for the Milky Way adds several layers of complexity, accounting for the inside-out  
 2812    growth of the thin disc, using empirically informed star  
 2813    formation histories that are a function of time and as-  
 2814    signing metallicities based on the position and age of  
 2815    binaries. In this section, we repeat our main analysis  
 2816    but instead apply a simpler model for the Milky Way in  
 2817    order to assess the effect of these added features. For  
 2818    this purpose, we use model for the Milky Way used in  
 2819    Breivik et al. (2020) as this is representative of the mod-  
 2820    els used in most previous works.

2821    Their model can be summarised as follows: the Milky  
 2822    Way is assumed to comprise of three components, a thin  
 2823    disc, a thick disc and a bulge. The spatial distributions  
 2824    and relative masses for these components are given in  
 2825    McMillan (2011). Breivik et al. (2020) assume constant  
 2826    star formation over 10 Gyr for the thin disc, a 1 Gyr  
 2827    burst of star formation 11 Gyr ago for the thick disc  
 2828    and a 1 Gyr burst of star formation 10 Gyr ago for the  
 2829    bulge. A major difference is that only two metallicities  
 2830    are used and they are assigned to binaries independent  
 2831    of age or position. Binaries formed in the thin disc and  
 2832    bulge are assumed to have a metallicity of  $Z = 0.02$   
 2833    and those formed in the thick disc are assumed to have  
 2834     $Z = 0.003$ .

2835    We show the spatial metallicity distribution for this  
 2836    model in Fig. D1 in the same form as Fig. 1 for ease  
 2837    of comparison between our models. The two main dif-  
 2838    ferences we can see between Fig. 1 and D1 are that the  
 2839    Breivik et al. (2020) model is more centrally concen-  
 2840    trated and only has two fixed metallicity populations.

2841    When applying this simpler Milky Way model in com-  
 2842    bination with our fiducial binary physics assumptions  
 2843    (model A), we find that the expected number of detec-  
 2844    tions for BHBHs, BHNSs and NSNSs for a 4-year LISA  
 2845    mission is 52, 25 and 17 respectively. Thus the BHBH  
 2846    detection has decreased slightly compared to our main  
 2847    findings, whilst for BHNSs and NSNSs the rate has ap-  
 2848    proximately halved and doubled respectively.

2849    Moreover, the distribution of parameters within the  
 2850    population, particularly the mass distributions, are no-  
 2851    tablely disparate. By using only two fixed metallicity pop-  
 2852    ulations, unphysical artifacts are introduced into distri-  
 2853    bution of DCO masses (e.g. Dominik et al. 2015; Neijssel  
 2854    et al. 2019; Kummer 2020). For example, in Fig. D2, we  
 2855    show the black hole mass distribution for BHNSs pro-  
 2856    duced by the simulation using the simple Milky Way  
 2857    model. Despite the fact that these KDEs use the same  
 2858    bandwidth as Fig. 3, the distributions show many more  
 2859    sharp transitions, which is a result of pileups occurring



2861    **Figure D1.** As Fig. 1 (right panel), but for the Milky Way  
 2862    model used in Breivik et al. (2020).

2863    at specific masses for specific metallicities. Moreover,  
 2864    the lack of lower metallicity systems means that higher  
 2865    mass systems are not formed and so we see the distri-  
 2866    butions do not include a high mass tail such as in our  
 2867    fiducial results.

2868    The unphysical artifacts present in the mass distribu-  
 2869    tions can have far-reaching effects since the masses of  
 2870    DCOs affect most other parameters. The inspiral time  
 2871    and SNR are directly dependent on the mass, whilst the  
 2872    uncertainty estimates depend on the SNR. This means  
 2873    that the artifacts can affect the predictions for most dis-  
 2874    tributions of LISA detectable populations.

2875    Overall, we find that previous studies that use Milky  
 2876    Way models analogous to this simpler model may signif-  
 2877    icantly underestimate the LISA BHNS rate whilst over-  
 2878    estimating the NSNS detection rate. They may also miss  
 2879    higher mass systems (particular for BHNSs) and contain  
 2880    unphysical artifacts in their parameter distributions.

2879    E. ESTIMATING THE NUMBER OF PULSARS  
 2880    FOR A GIVEN SKY AREA IN SKA

2881    In this section, we perform some back-of-the-envelope  
 2882    calculations in order to estimate the number of pulsars  
 2883    that SKA will observe within a given sky area.

2884    First, we consider how many pulsars SKA is likely  
 2885    to detect. Keane et al. (2015) uses PSRPOPPy (Bates  
 2886    et al. 2014) to simulate the Milky Way pulsar popula-

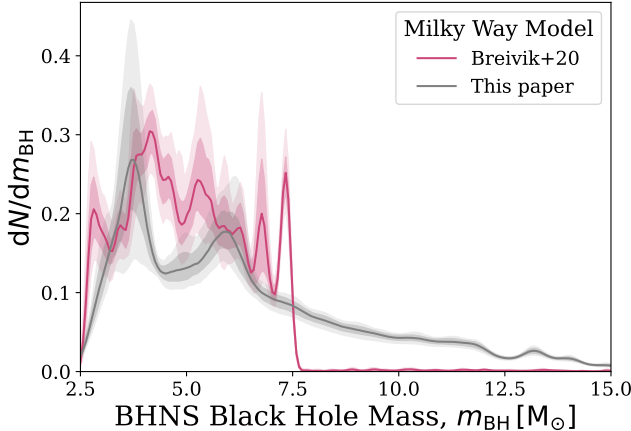


**Figure D2.** As Fig. 3b, but for the Milky Way model used in Breivik et al. (2020). Dotted lines show the distribution from Fig. 3b for comparison. 

tion. They find that for SKA-1, approximately 10000 pulsars will be discovered. The second phase of SKA, which should be in operation by the time of the LISA mission, would yield a total of 35000-41000 pulsars (Keane et al. 2015). We use the average, 38000, in further estimates below. Moreover, we are only interested in pulsars that are part of a binary system. We estimate this pulsar binary fraction as the fraction of known pulsars that are in binaries using the ATNF Pulsar Catalogue<sup>8</sup> (Manchester et al. 2005). 290 of the 2872 currently known pulsars are in binary systems and thus we estimate the binary fraction of pulsars as 10%. Therefore, we expect that SKA-1 and SKA-2 will detect approximately 1000 and 3800 binary pulsars respectively.

Next, we can find the total number of pulsars SKA will detect in a patch on the sky. The total sky area that the SKA covers is approximately  $5700 \text{ deg}^2$ , which is calculated by integrating over the sky for all Galactic longitudes and Galactic latitudes limited to  $|b| < 10^\circ$  and  $\delta < 45^\circ$ , which are the limits on SKA-mid (Keane et al. 2015). If we assume that the pulsars are found uniformly across the sky, this means that roughly 0.2 and 0.7 binary pulsars are expected per square degree for SKA-1 and SKA-2 respectively. Note that the assumption of a uniform distribution is not realistic as pulsars will tend to be far more concentrated in the Galactic centre but we use it to provide a slightly optimistic estimate.

Overall, we therefore expect a single pulsar per  $5.7 \text{ deg}^2$  and  $1.5 \text{ deg}^2$  for SKA-1 and SKA-2 respectively,

which correspond to angular resolutions of  $\sigma_\theta = 1.3^\circ$  and  $\sigma_\theta = 0.7^\circ$ .

<sup>8</sup><https://www.atnf.csiro.au/research/pulsar/psrcat>

## F. SUPPLEMENTARY MATERIAL

**Table F1.** The number of detectable binaries in a 4- and 10-year LISA mission for the 20 different model variations and each DCO type. Each model variation is discussed in App. A.3 and the trends in detection rates are discussed in Sec. 4.1. The ‘All’ column contains the total expected detections when summed over the three types. The final two rows show the minimum and maximum rates across all model variations. We embolden the corresponding rate for convenience of seeing which variation results in the minimum/maximum. Each value shows the mean and the  $1-\sigma$  Poisson uncertainty.  $\Xi$ .

Model	Description	LISA detections (4 year)				LISA detections (10 year)			
		All	BHBH	BHNS	NSNS	All	BHBH	BHNS	NSNS
A	Fiducial	$124^{+11}_{-11}$	$74^{+8}_{-9}$	$42^{+7}_{-6}$	$8^{+3}_{-3}$	$202^{+14}_{-15}$	$117^{+11}_{-10}$	$71^{+8}_{-8}$	$13^{+4}_{-4}$
B	Fixed mass transfer efficiency of $\beta = 0.25$	$94^{+10}_{-10}$	$69^{+8}_{-9}$	$22^{+5}_{-4}$	$3^{+2}_{-2}$	$149^{+12}_{-12}$	$108^{+10}_{-11}$	$37^{+6}_{-6}$	$5^{+2}_{-2}$
C	Fixed mass transfer efficiency of $\beta = 0.5$	$59^{+8}_{-8}$	$47^{+7}_{-7}$	$8^{+3}_{-3}$	$4^{+2}_{-2}$	$96^{+9}_{-10}$	$76^{+8}_{-9}$	$14^{+3}_{-4}$	$7^{+2}_{-3}$
D	Fixed mass transfer efficiency of $\beta = 0.75$	$67^{+8}_{-8}$	$47^{+7}_{-7}$	$7^{+3}_{-2}$	$13^{+3}_{-4}$	$104^{+11}_{-10}$	$71^{+8}_{-8}$	$12^{+4}_{-3}$	$21^{+5}_{-4}$
E'	Case BB mass transfer is always unstable	$90^{+9}_{-10}$	$66^{+8}_{-8}$	$21^{+5}_{-5}$	$3^{+2}_{-2}$	$133^{+12}_{-11}$	$101^{+10}_{-10}$	$29^{+5}_{-5}$	$4^{+2}_{-2}$
F	Case BB Unstable + Optimistic CE	<b><math>368^{+19}_{-19}</math></b>	<b><math>154^{+12}_{-13}</math></b>	<b><math>198^{+14}_{-14}</math></b>	<b><math>17^{+4}_{-4}</math></b>	<b><math>553^{+23}_{-24}</math></b>	<b><math>238^{+16}_{-15}</math></b>	<b><math>289^{+17}_{-17}</math></b>	<b><math>25^{+5}_{-5}</math></b>
G	CE efficiency $\alpha = 0.1$	$40^{+6}_{-6}$	$28^{+5}_{-5}$	<b><math>2^{+2}_{-1}</math></b>	$10^{+3}_{-3}$	$64^{+8}_{-8}$	$44^{+6}_{-7}$	<b><math>3^{+2}_{-1}</math></b>	$17^{+4}_{-4}$
H	CE efficiency $\alpha = 0.5$	$86^{+9}_{-10}$	$58^{+8}_{-7}$	$22^{+4}_{-5}$	$6^{+2}_{-3}$	$136^{+11}_{-12}$	$91^{+10}_{-9}$	$35^{+6}_{-6}$	$10^{+3}_{-3}$
I	CE efficiency $\alpha = 2.0$	$133^{+11}_{-12}$	$67^{+9}_{-8}$	$38^{+6}_{-6}$	$28^{+5}_{-6}$	$218^{+14}_{-15}$	$109^{+11}_{-10}$	$62^{+8}_{-7}$	$46^{+7}_{-7}$
J	CE efficiency $\alpha = 10.0$	$78^{+9}_{-9}$	$27^{+5}_{-6}$	$16^{+4}_{-4}$	<b><math>35^{+6}_{-6}</math></b>	$126^{+11}_{-11}$	$42^{+7}_{-6}$	$27^{+5}_{-6}$	<b><math>57^{+8}_{-7}</math></b>
K	HG donor stars initiating a CE survive CE	$218^{+14}_{-15}$	$151^{+12}_{-12}$	$57^{+7}_{-8}$	$10^{+3}_{-3}$	$340^{+19}_{-18}$	$229^{+15}_{-15}$	$96^{+10}_{-10}$	$16^{+4}_{-4}$
L	Fryer rapid SN remnant mass prescription	$127^{+11}_{-11}$	$50^{+7}_{-7}$	$70^{+8}_{-8}$	$7^{+2}_{-3}$	$204^{+15}_{-14}$	$76^{+9}_{-8}$	$117^{+11}_{-11}$	$11^{+3}_{-3}$
M	Maximum NS mass = $2.0 M_{\odot}$	$133^{+12}_{-11}$	$96^{+10}_{-10}$	$30^{+5}_{-5}$	$7^{+3}_{-2}$	$214^{+15}_{-14}$	$153^{+13}_{-12}$	$50^{+7}_{-7}$	$12^{+3}_{-4}$
N	Maximum NS mass = $3.0 M_{\odot}$	$118^{+11}_{-11}$	$58^{+8}_{-8}$	$52^{+7}_{-7}$	$8^{+3}_{-3}$	$189^{+14}_{-13}$	$91^{+10}_{-9}$	$85^{+9}_{-10}$	$14^{+3}_{-4}$
O	No PISN and pulsational-PISN	$126^{+12}_{-11}$	$75^{+9}_{-9}$	$43^{+7}_{-6}$	$8^{+3}_{-3}$	$205^{+14}_{-14}$	$120^{+11}_{-11}$	$72^{+9}_{-8}$	$13^{+3}_{-4}$
P	$\sigma_{\text{RMS}}^{1D} = 100 \text{ km s}^{-1}$ for CCSN	$184^{+14}_{-14}$	$82^{+9}_{-9}$	$86^{+10}_{-9}$	$15^{+4}_{-4}$	$300^{+17}_{-17}$	$130^{+11}_{-12}$	$145^{+12}_{-12}$	$26^{+5}_{-6}$
Q	$\sigma_{\text{RMS}}^{1D} = 30 \text{ km s}^{-1}$ for CCSN	$268^{+16}_{-16}$	$92^{+9}_{-10}$	$143^{+12}_{-12}$	$34^{+6}_{-6}$	$426^{+21}_{-20}$	$142^{+12}_{-11}$	$229^{+15}_{-16}$	$55^{+8}_{-7}$
R	Black holes receive not natal kick	$205^{+15}_{-14}$	$89^{+10}_{-9}$	$109^{+10}_{-11}$	$7^{+3}_{-2}$	$332^{+18}_{-18}$	$140^{+12}_{-12}$	$180^{+13}_{-13}$	$12^{+3}_{-4}$
S	Wolf-Rayet wind factor $f_{\text{WR}} = 0.1$	$118^{+11}_{-11}$	$75^{+9}_{-8}$	$34^{+6}_{-6}$	$9^{+3}_{-3}$	$182^{+13}_{-14}$	$112^{+11}_{-11}$	$56^{+7}_{-8}$	$14^{+4}_{-4}$
T	Wolf-Rayet wind factor $f_{\text{WR}} = 5.0$	<b><math>30^{+5}_{-6}</math></b>	<b><math>6^{+2}_{-3}</math></b>	$15^{+4}_{-3}$	$8^{+3}_{-2}$	<b><math>49^{+7}_{-7}</math></b>	<b><math>9^{+3}_{-3}</math></b>	$26^{+5}_{-5}$	$13^{+4}_{-3}$
-	Minimum rate	$30^{+5}_{-6}$	$6^{+2}_{-3}$	$2^{+2}_{-1}$	$3^{+1}_{-2}$	$49^{+7}_{-7}$	$9^{+3}_{-3}$	$3^{+2}_{-1}$	$4^{+2}_{-2}$
-	Maximum rate	$368^{+19}_{-19}$	$154^{+12}_{-13}$	$198^{+14}_{-14}$	$35^{+6}_{-6}$	$553^{+23}_{-24}$	$238^{+16}_{-15}$	$289^{+17}_{-17}$	$57^{+8}_{-7}$

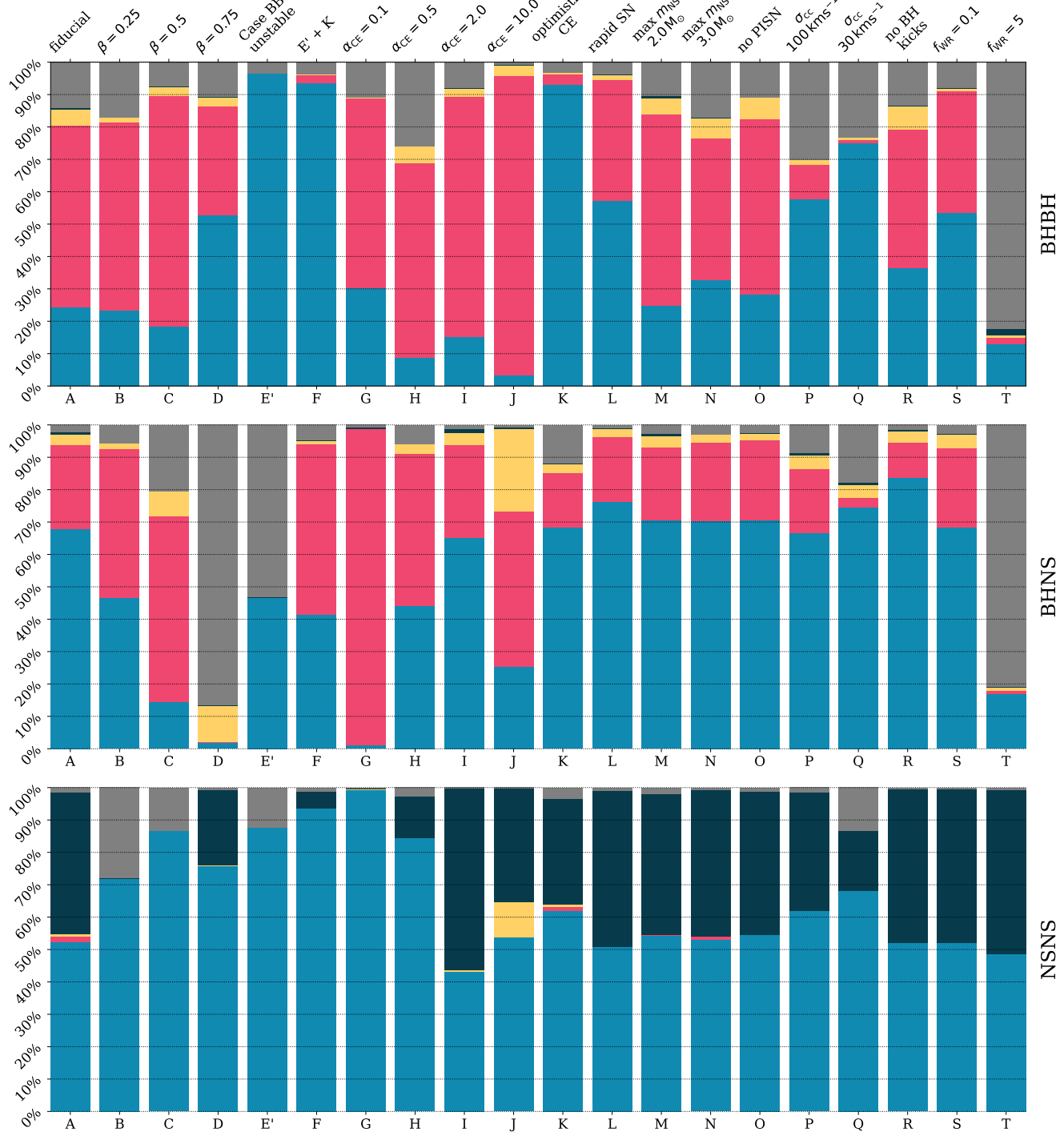


**Figure F1.** Fraction of each DCO type that is formed through different formation channels for all physics variations. Channels are described in detail in Broekgaarden et al. (2021a). The classic, single core CEE and double core CEE channels all require at least one common-envelope event whilst only “only stable” consists of only stable mass transfer and “other” contains the remaining binaries which are mainly formed from case A “classic” binaries as well as “lucky” supernova kicks that shrink the binary. .

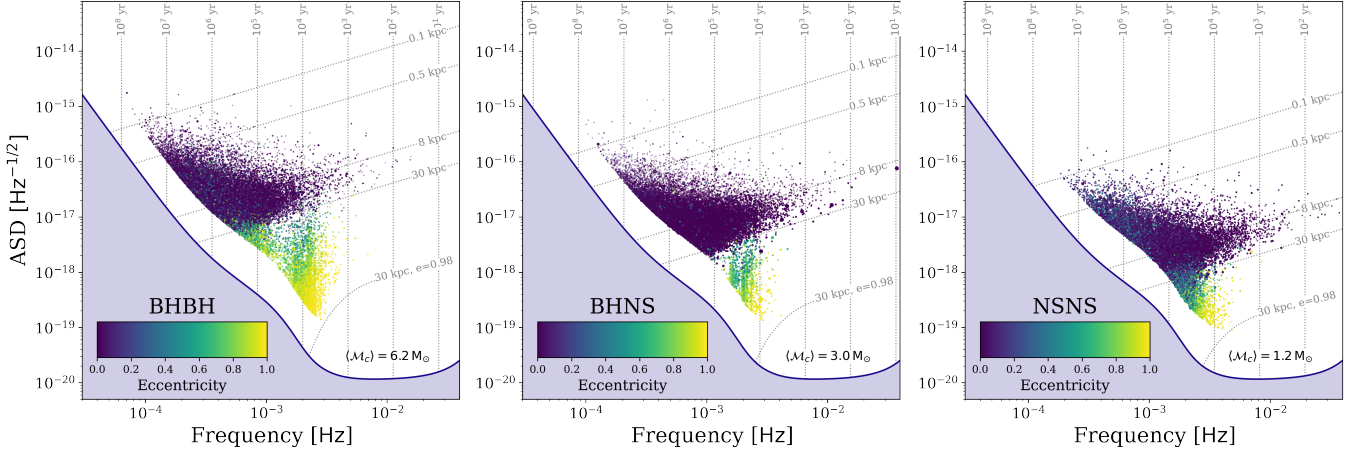


**Figure F2.** As the bottom panels of Fig. 2, but without the density distributions and scatter points are coloured by their eccentricity. We show eccentric sources are located in an offshoot below the 30 kpc around 2 mHz. .

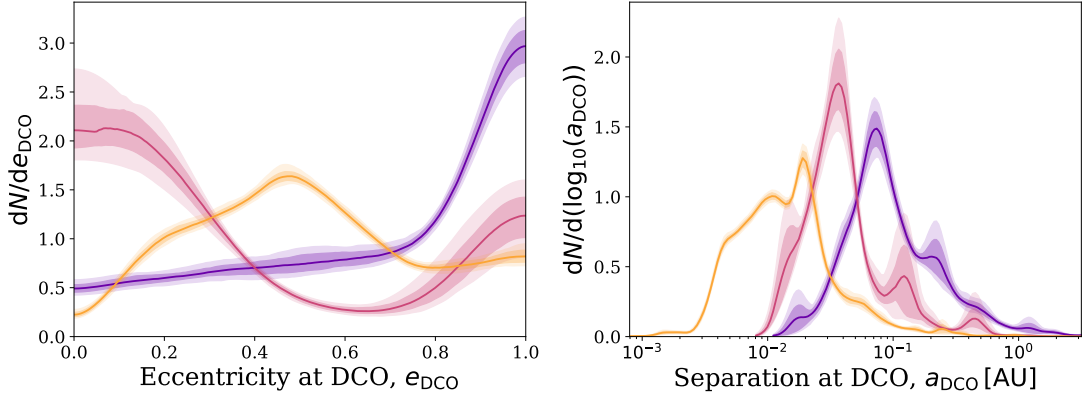


**Figure F3.** As Fig. 3, but for the properties of the detectable systems at DCO formation. .